Geochemistry and Geochronology of the Whabouchi Pegmatite Dykes as Revealed Through Zircon

Undergraduate Thesis submitted to Dr. James Brenan

by Caitlin Beland

996336228

April 11th 2011

TABLE OF CONTENTS

ABSTRACT

The purpose of this study was to determine a U-Pb age for the Whabouchi Li-pegmatite dykes from zircon and investigate their geochemistry in an attempt to constrain aspects of their petrogenesis and place their occurrence in a regional context. This was done by *in-situ* determination of trace element abundances and U, Pb isotopes by LA-ICP-MS combined with a petrographic study. The Whabouchi pegmatites are peraluminous in composition and are albite-spodumene type. The zircon contain unprecedented levels of Li, and exhibit HREE depleted REE patterns, characteristic of prior/concurrent growth of garnet. The reported age of emplacement determined in this study is 2577 ± 13 Ma. Examination of thermal models indicates the possibility that the Whabouchi pegmatite-forming melt could have been generated by anatexis following crustal thickening in a compressional regime.

INTRODUCTION

Lithium pegmatites are an important source of economic Li used in ceramics and the pharmaceutical industry as well as a number of other industrial applications (Talison Lithium, 2010). One of the newest applications of Li metal is the lithium ion battery for electric vehicles (Talison Lithium, 2010). Understanding their genesis is essential to better delineate geologic terranes and environments permissive to their occurrence. The present work combines a petrographic study and *in situ* determination of trace element abundances and U-Pb ratios in zircon of the Whabouchi Li-pegmatite dykes in Quebec, Canada, to place their occurrence in a regional context by determining the age of emplacement, textural relationships and geochemical trends.

REGIONAL GEOLOGY

Location

The Whabouchi spodumene-bearing pegmatite swarm lies in the eastern James Bay region of Quebec, Canada, in the Superior Province. Specifically, it is located in the Opinaca (OnS) metasedimentary subprovince, bounded to the east by the Ashuanipi Complex (AC) and to the north and south by the La Grande (LG) and Opatica (OcS) volcano-plutonic subprovinces, respectively (Figure 1).

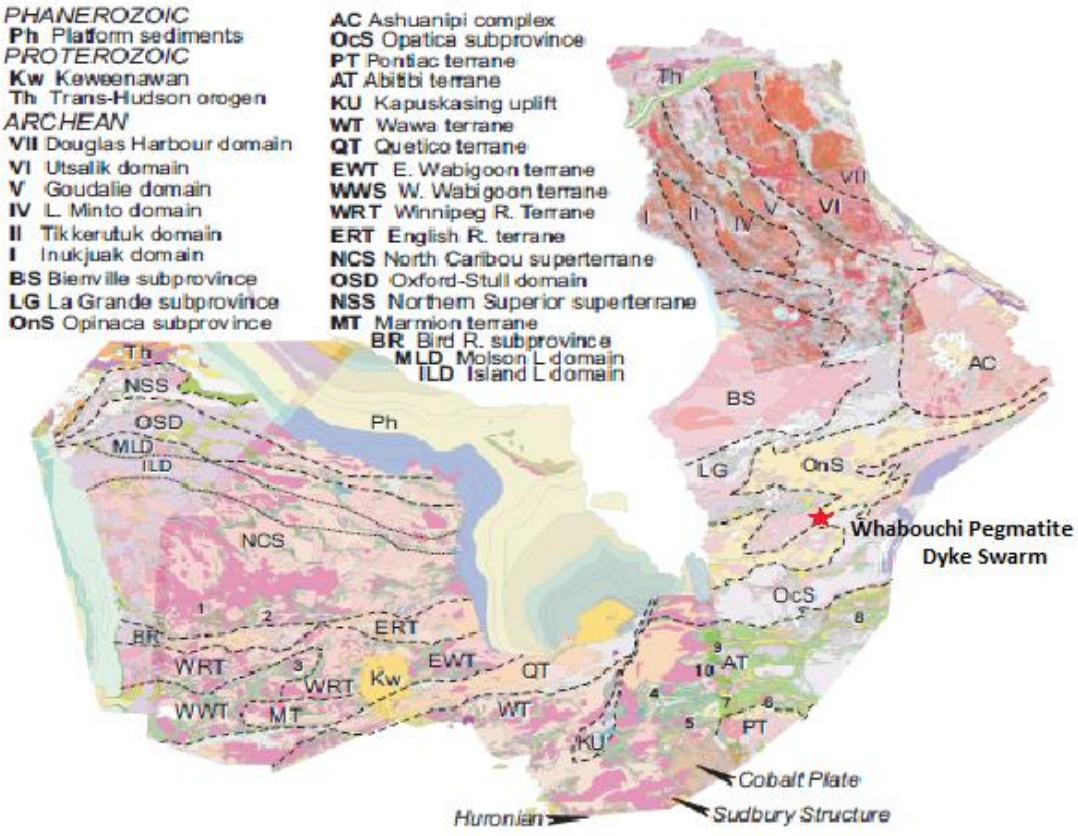

Figure 1: A map of the superior province, Canada, after Percival (2007)

The OnS-AC contact is marked by the Nichicun Fault, where AC was thrust southward over OnS (Caderon 2003). The OnS-AC-OcS contact is fault bound by the Lac Vallard thrust fault that thrust OnS over OcS (Caderon, 2003). Similarly, the OnS-LG contact is not defined by a single continuous, regional structure or lithology, but is fault bound (Dalmas thrust fault, OnS over LG) or depositional, the latter being interpreted as conformable in some places and unconformable in others (Caderon, 2003, Simard and Gosselin, 1999). The depositional contact has also been inferred at the interface of two intrusive suites, one assigned to LG and the other OnS, under the assumption that it was obliterated by their emplacement (Simard and Gosselin, 1999).

Lithologies

The OnS is interpreted to have been an Archean sedimentary basin which was subsequently intruded by felsic-intermediate intrusive rocks of varying ages. Volcanics are relatively rare in the OnS, though there are some amphibolitized basalts in the interior (stratigraphic center) (Simard and Gosselin, 1999). The subprovince is also bordered by volcanosedimentary belts to the east and west, contained in the adjacent subprovinces (Simard and Gosselin, 1999). A simplified timeline of the subprovince geology is given in Figure 2.

Metasediments

The Opinaca subprovince has a gneissic basement, dated to 2811 Ma (Caderon, 2003) overlain by a thick metasedimentary sequence, whose primary structures have been entirely destroyed by high grade metamorphism and migmatization (Simard and Gosselin, 1999). The metasediments are dominated by a biotite-paragneiss composed mainly of quartz, biotite and plagioclase (Simard and Gosselin, 1999) though there are variations in mineralogy throughout

this lithology due to differences in protolith composition, likely ranging from greywacke to pelite. Biotite-paragneisses formed from greywacke protoliths are richer in ferromagnesian minerals (>25 %) than their pelitic counterparts (<15%) (Simard and Gosselin, 1999).

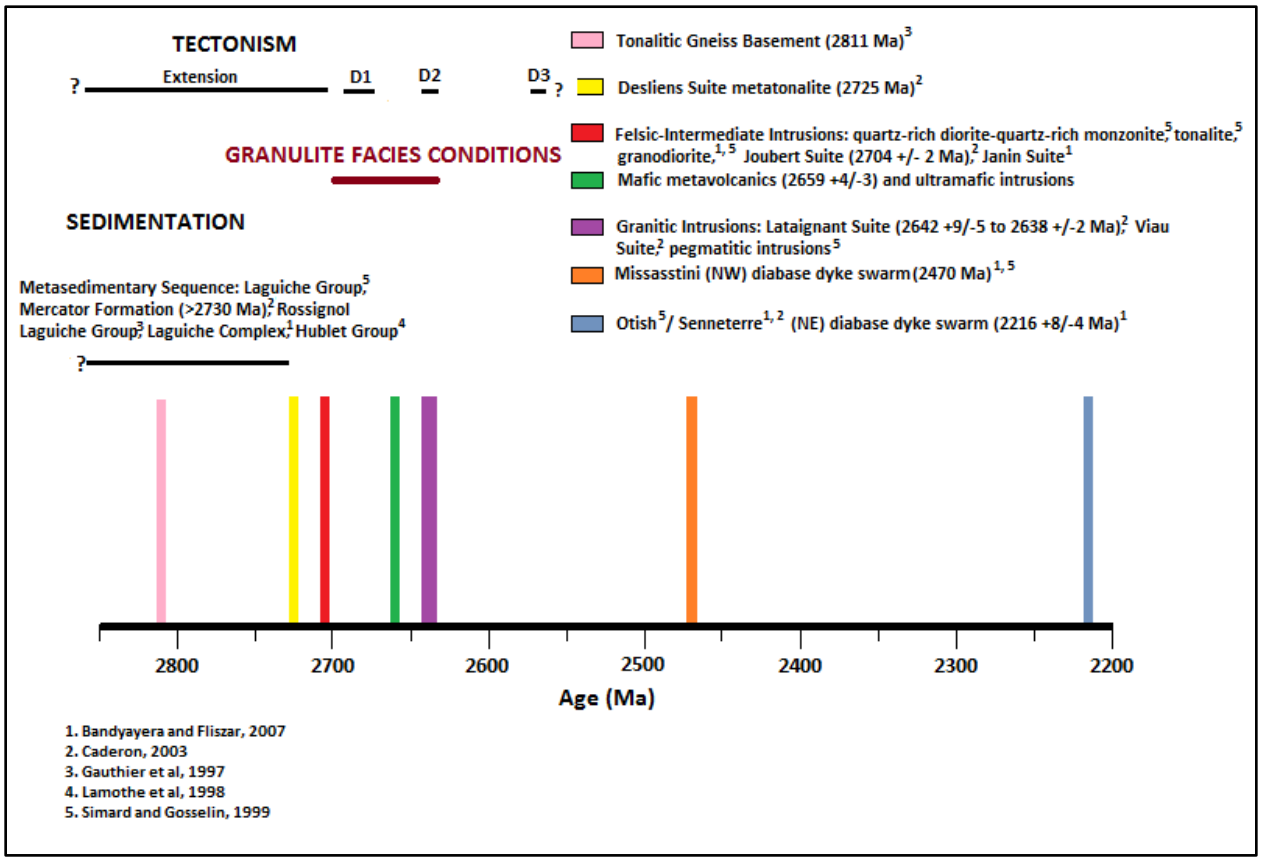

Figure 2: A simplified timeline of the regional geology of the Opinaca subprovince. The y axis is arbitrary.

In addition to the voluminous biotite-paragneiss, the metasedimentary sequence also contains horizons of magnetite-paragneiss which is very similar in composition to its biotite counterpart, with magnetite replacing biotite as the dominant ferromagnesian mineral (Figure 3) (Simard and Gosselin, 1999). There are also thin horizons of paragneiss containing andalusite and/or cordierite porphyroblasts with minor garnet and sillimanite (Figure 4) (Simard and Gosselin, 1999). More highly metamorphosed sediments include coarser grained, green

hornblende-rich, mesocratic, weakly banded gneisses (Simard and Gosselin, 1999), which represent greenschist facies metamorphism. Their occurrence has been linked to contact metamorphism by adjacent plutons (Franconi, 1983). There are abundant horizons of amphibolite and amphibolite gneisses intercalated with the metasediments, though too thin to be mappable units (Simard and Gosselin, 1999). The protolith of the amphibolites is uncertain and could either represent mafic lavas extruded into a sedimentary basin, or gabbroic sills and dykes (Simard and Gosselin, 1999).

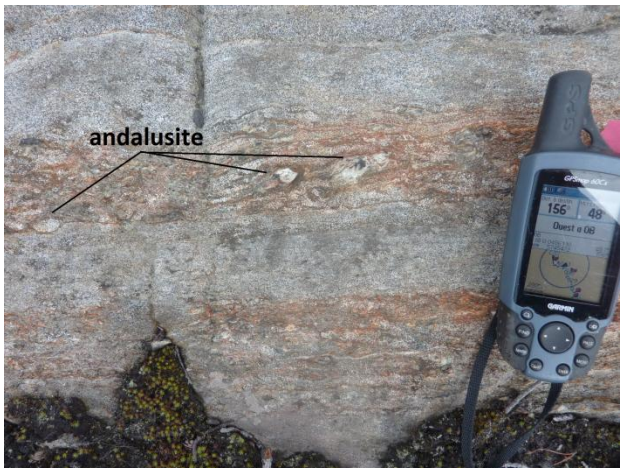

Figure 3: Magnetite-rich layers within migmatized paragneiss. Figure 4: Andalusite-porphyroblastic paragneiss.

Intrusives

Intrusive rocks are abundant in OnS, occupying approximately 30% of surface outcrop (Simard and Gosselin, 1999). The felsic-intermediate intrusions are mostly Archean in age, cross cutting the same metasediments from which they likely formed from by anatexis (Card and Ciesielski, 1986).

The oldest intrusive suite is tonalitic-granodioritic in composition and was emplaced during the same regional metamorphism that migmatized the metasediments, as is evidenced by the development of a penetrative regional foliation through all pre- to syn-tectonic units (Simard and Gosselin, 1999).

The next oldest intrusive suite ranges in composition from quartz-rich diorite to quartz-rich monzonite and is the most voluminous unit in OnS (Simard and Gosselin, 1999). This suite was also emplaced syn-deformation as is evidenced by a well developed foliation expressed by the alignment of amphiboles (Simard and Gosselin, 1999). The quartz-rich diorite- quartz-rich monzonite suite has an irregular thickness and often contains enclaves of amphibolite (Simard et Gosselin, 1999).

Next are the late granitic intrusions which are characterized by an equigranular, medium grain size and homogeneous appearance (Simard and Gosselin, 1999). OnS granites are unfoliated and commonly contain enclaves of paragneiss, suggesting they were emplaced post-deformation and formed by anatexis of the metasediment (Simard and Gosselin, 1999).

There are numerous fields of compositionally simple pegmatite dykes, pink or white in colour depending on which alkali feldspar is dominant, microcline or orthoclase, respectively (Bandyayera and Fliszar, 2007). The pegmatite dykes are largely undeformed, unfoliated and massive, sometimes containing enclaves of paragneiss (Bandyayera and Fliszar, 2007).

The youngest intrusives are post-tectonic, Proterozoic diabase dykes that are strongly magnetic and extend along strike for metres to hundreds of metres (Simard and Gosselin, 1999). There are two swarms, evidenced by their differing orientation and age. The Missasstini

Swarm trends NW and was dated to 2470 Ma, while the Senneterre Swarm trends NE and was dated to 2216 +8/-4 Ma (Bandyayera and Fliszar, 2007).

Regional Metamorphism

The metamorphic grade in the OnS is granulite facies, with local, complete retrograde metamorphism to amphibolite or greenschist facies. Granulite facies metamorphism is recorded in mineral assemblages through the occurrence of orthopyroxene (opx) in metasediments (Caderon, 2003), indicating anhydrous metamorphic conditions (Simard and Gosselin, 1999). Caderon (2003) determined the presence of two generations of orthopyroxene through their occurrence and alignment within two different regional foliations. The author links the opx generations to two granulite facies metamorphic phases, each linked to a deformation episode, that describe a continuous, clockwise, P-T-t path in a protracted polyphased granulite metamorphic episode (Caderon, 2003). Caderon (2003) cites chemical continuity in opx composition between generations and similar P-T conditions for the same mineral assemblages between metamorphic events as evidence for continuous tectonometamorphic evolution. While there is a large temperature decrease between P-T-t paths for the metamorphic events, there is only a slight drop in pressure, leading Caderon (2003) to conclude that they represent near-isobaric cooling paths.

The first metamorphic phase is related to compression and the onset of closure of the Opinaca sedimentary basin from 2705 to 2680 Ma and is manifested by the thickening of sediments through both ductile and brittle deformation as they were progressively exhumed (Caderon, 2003). Minimum peak P-T conditions were determined through

geothermobarometry of mineral assemblages, and were found to be 8.2 ± 1 kbar at 960 ± 50°C (Caderon, 2003). Minimum P-T conditions for this metamorphic episode represent a cooling phase and are 5.1 ± 1 kbar at 720 ± 50°C (Caderon, 2003). Prolonged granulite facies conditions resulted in the formation of huge volumes of melt by anatexis of LG, OcS and OnS lithologies (Caderon, 2003). Between 2680 and 2650, these anatectic melts originating in the Ashuanipi Complex were injected along the Dalmas and Lac Vallard Faults, at the LG-OnS and OnS-OcS contacts, respectively (Caderon, 2003).

The second granulite phase is linked to continued compression and the final closure of the Opinaca basin, with minimum peak P-T conditions of 8.3 ± 1 kbar and 890 ± 50°C and minimum cooling P-T conditions of 5.8 ± 1 kbar at 720 ± 50°C (Caderon, 2003). This second phase began as the first granulite event began its cooling phase, with minimum cooling conditions of 5.8 ± 1 kbar and 720 ± 50°C, and likely stabilized at amphibolite facies between 2635 and 2633 Ma (Caderon, 2003).

Another major product of metamorphism in the Opinaca subprovince is regional migmatization, affecting all lithologies except for the late Proterozoic diabase dykes (Simard and Gosselin, 1999). This is manifested as migmatites that contain 10 to >90 % (by volume) mobilizate; those containing 60 – 90 % leucosome are banded while migmatites with >90% leucosome are massive (Simard and Gosselin, 1999). Though the size and orientation, colour, grain size and texture of mobilizate injections are widely variable, their composition is always granitic (Simard and Gosselin, 1999). Injections of mobilizate are commonly metre to tens of metres thick and concordant with the regional gneissosity/foliation which indicates pre- and/or

syn-tectonic emplacement (Simard and Gosselin, 1999). Less common are thinner, discordant injections, interpreted to have been emplaced late or post-tectonic, that indicate either continued or a second phase of migmatization (Simard and Gosselin, 1999).

The origin of anatectic melt in the Opinaca subprovince is uncertain. Simard and Gosselin (1999) state that the maximum anhydrous P-T conditions reached in OnS could not have produced such a large volume of melt, and that the majority was probably formed by anatexis at depth with melts later migrating upwards to be emplaced as granitic intrusions.

Structural Geology and Deformation History

Caderon (2003) conducted a tectono-metamorphic study of the Opinaca subprovince, and found that there were three regional ductile deformation events (Figure 5) and one brittle deformation event that affected Opinaca lithologies.

Figure 5: Photograph showing polyphased deformation in amphibolitized basalt.

The principal structural feature in the OnS is a regional foliation oriented E-W and dipping 30° to 60° north or south, affecting all lithologies except for late intrusives (Simard and Gosselin, 1999) and formed during the first ductile deformation event (Caderon, 2003). The first deformation event was caused by subduction of an oceanic slab, resulting in E-W, to NW-SE compression and initiation of closure of the Opinaca basin (Caderon, 2003) (Figure 6,7). The foliation is expressed by the alignment of biotite or hornblende in syn-tectonic intrusions, or by the gneissosity and injections of mobilizate parallel to the foliation in metasediments (Simard and Gosselin, 1999). The OnS metasediments were also significantly thickened as they were exhumed (Caderon, 2003). Furthermore, the originally extensional, normal Dalmas and Lac Vallard faults were reactivated as reverse faults, resulting in simultaneous thrusting to the north and south, creating a positive flower structure (Caderon, 2003). This deformation event continued from 2705 to 2680 Ma, when there was a hiatus in compression of the Opinaca basin (Caderon, 2003).

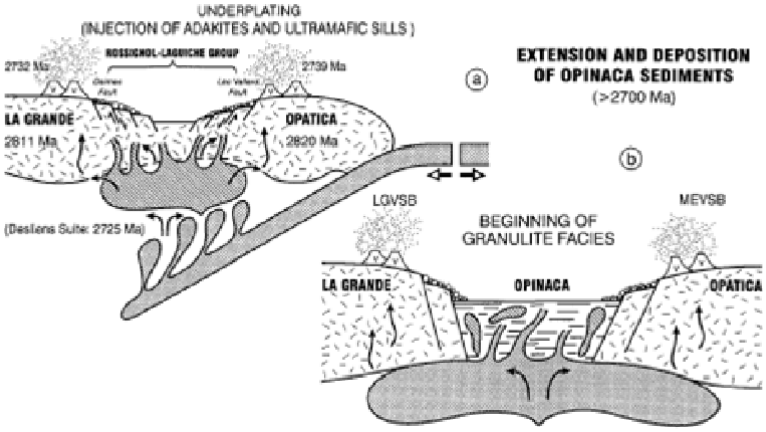

Figure 6: Schematic depiction of the events leading up to the first stage of ductile deformation, including the formation of the Opinaca basin, the emplacement of the Desliens Suite, and the activation of the Dalmas and Lac Vallard normal faults, after Caderon (2003).

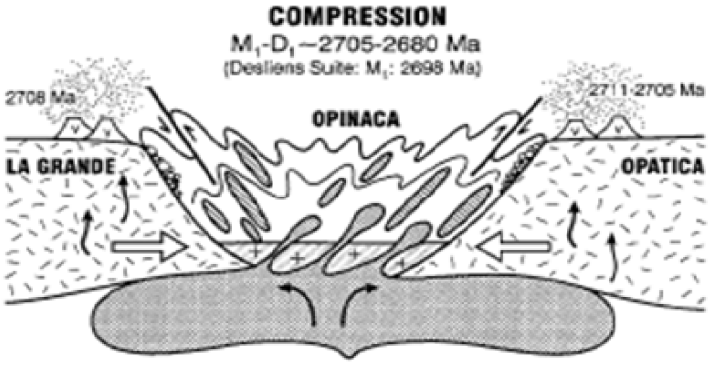

Figure 7: Schematic depiction of the N-S compression of the first ductile deformation event (D1) that Opinaca experienced, resulting in a positive flower structure and the reactivation of the originally normal Dalmas and Lac Vallard faults as reverse faults, after Caderon (2003).

The second deformation event is related to the final closure of the Opinaca basin from 2647 to 2638 Ma by N-S compression (Caderon, 2003). At this time, all structures originating from the previous deformation event, as well as the Dalmas and Lac Vallard faults, were refolded into E-W oriented folds, plunging ENE and overturned southward (Caderon, 2003), though there is no foliation associated to the folding (Simard and Gosselin, 1999). Moreover, the entire Opinaca basin was folded into a southward-overturned anticline (Caderon, 2003).

The third, and last ductile deformation event affected Opinaca and resulted in the refolding of previous structures into N-S oriented, large amplitude folds (Caderon, 2003). This event's upper age limit was determined to be 2571 Ma, while the lower limit is unconstrained (Caderon, 2003). The only brittle and Proterozoic deformation event is associated with the Grenville Orogeny at 1000 Ma, and resulted in a regional N-S fault system, with two conjugate sets of faults trending NW and NE (Caderon, 2003). The NW trending fault system has a dextral strike-slip component, and the regional foliation tends to bend parallel to the faults (Simard

and Gosselin, 1999). The Missasstini diabase dykes are commonly intruded along NW trending faults (Simard and Gosselin, 1999), therefore it is likely that the Senneterre diabase dyke emplacement was similarly controlled by the NE trending regional fault system. However, the NW and NE trending faults that the diabase dyke swarms were emplaced along cannot be the same as those related to the Grenville Orogeny described by Caderon (2003) since they were formed 1.2 to 1.7 By after the dykes intruded. This suggests that there is an Archean brittle deformation event that has not yet been accounted for and that similarly resulted in NW, and possibly NE trending fault systems.

Interpretation/Regional Context

It has been suggested that the Opinaca metasedimentary province represents the eastern lateral equivalent of the Nemiscau and Quetico basins to the west. This is consistent with the three basins having very similar lithologies, Nemiscau and Opinaca in particular, which both contain approximately 20% metapelites and 80% metagraywackes intercalated with thin mafic volcanic flows (Doyon, 2004). Doyon (2004) also found that sediments deposited in the three basins have comparable geochemical patterns and attributed this to the same or a similar source of sediment. Furthermore, all three basins' sediments have similar minimum ages of deposition. Quetico sediments were found to have a depositional age ranging from 3009 ± 4 Ma to 2698 ± 3 Ma (Davis et al, 1990), while Nemiscau sediments were dated to 2668 Ma (Doyon, 2004) and the deposition of Opinaca sediments is constrained to a maxiumum of 2730 Ma (Caderon, 2003).

The Quetico basin has been interpreted as an accretionary prism (Doyon, 2004) therefore if the three basins are actually one and the same, OnS could also represent an Archean accretionary prism. Similarly, Percival et al (1992) and Percival (1990) have suggested that together, the Opinaca subprovince and the Ashuanipi Complex represent an accretionary prism. Caderon (2003) however discounts this hypothesis due to the fact that it does not agree with the thermobarometric data obtained in their study nor their mineralogical and structural data. Additionally, Caderon (2003) states that the OnS is double vergence structure, characteristic of pull apart basins in transpressional regimes and proposes instead that the OnS is a marginal basin deposited on a thinned crust during the Kenoran orogeny.

LOCAL GEOLOGY

The Whabouchi spodumene-bearing pegmatite dyke swarm is located in the volcanosedimentary Lac des Montagnes Formation, which is a narrow sliver of the OnS wedged between the Lac des Champions granitoids and the NE section of the OcS (Laferriere, 2009) (Figure 8).The Lac des Montagnes formation is oriented northeast and is comprised of intercalated paragneiss and amphibolites crosscut by granitic intrusive rocks, including white pegmatite dykes and sills (Laferriere, 2009). A summary of lithologies is provided in Table 1. The Lac des Champions granitoids are comprised of orthogneiss and undifferentiated granites (Laferriere, 2009). The swarm is bordered to the WSW by Lac des Montagnes and to the ENE by Lac du Spodumene.

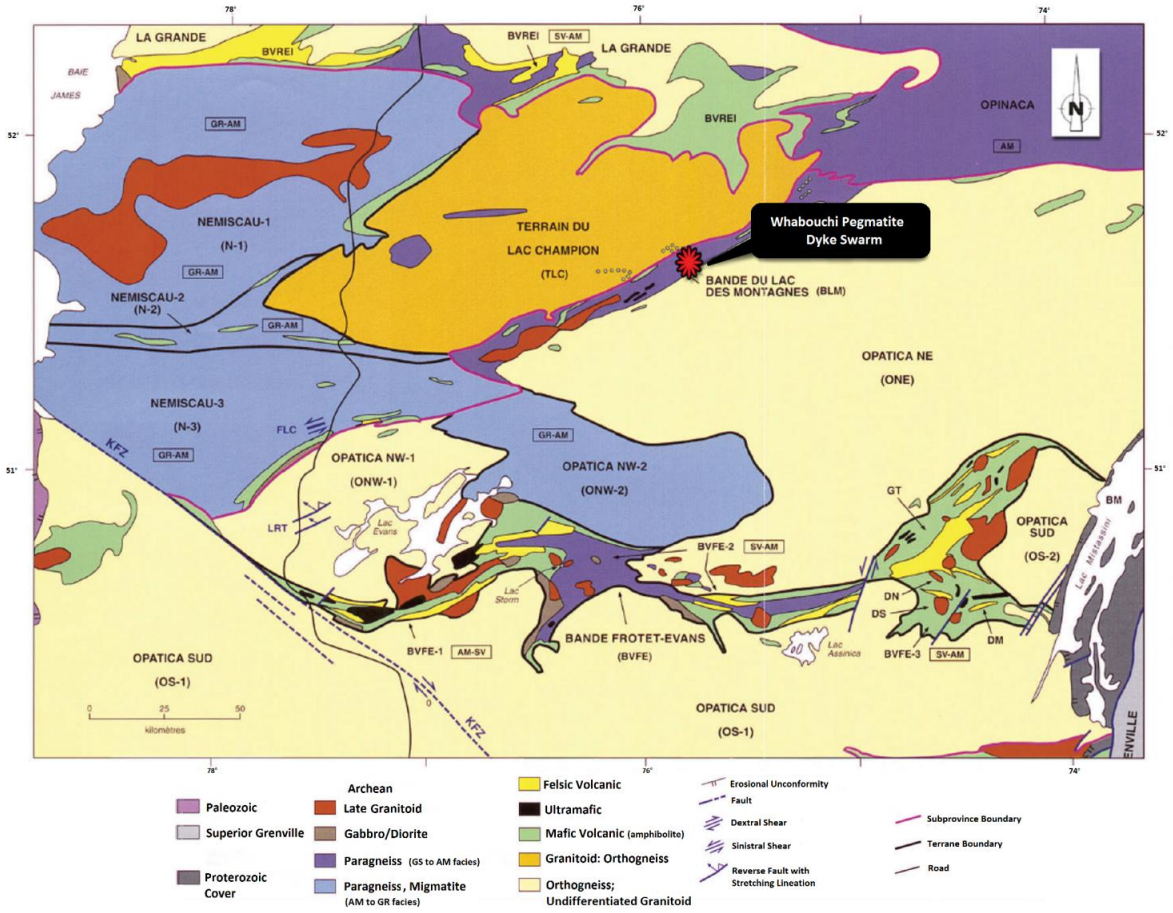

Figure 8: A map of the local geology hosting the Whabouchi pegmatite dyke swarm, after Laferriere (2009).

Table 1: Local geology, after Bussieres and Theberge (2010).

Pleistocene and Holocene	Moraines, eskers, alluvial deposits and string bogs
Precambrian	10 - Diabase
	9 – White or pink granite, alaskite, quartz monzonite, pink pegmatite and aplite
	8 – White anatexis granite containing 10% to 40% of paragneiss or amphibolite enclaves. White pegmatites
	7 – Porphyric granodiorite
	6 – Hornblende gneiss
	5 – Granodiorite, tonalite, trondhjemite, a few diorites, gneissic and migmatized facies
	4 – Migmatites, made up of 40% to 70% paragneiss and/or amphibolite with white or pink granite mobilizate
	3 – Biotite and chlorite-bearing paragneiss or schist - with biotite, muscovite, (cordierite or sillimanite or andalousite); - with biotite, garnet, (cordierite or sillimanite or andalousite); - with biotite, cordierite, sillimanite, andalousite; - with biotite, sillimanite, andalousite and staurotide; - metasomatic rock and quartz rich paragneiss.
	2 – Metavolcanic rocks, associated tuffs and paragneiss amphibolite and a few ultramafic rocks
	1 – Ultramafic rocks, peridotites, serpentinites, actinote and tremolite bearing rocks.

All of these lithologies are Archean in age except for the Proterozoic diabase dykes (Valiquette, 1975). Exposure is generally quite good in the area due to high ridges of ultramafic and felsic intrusive rocks, though the valleys in between are sometimes covered by overburden consisting of Pleistocene and Holocene glacial and alluvial deposits (Valiquette, 1975). The entire area was glaciated, with general ice flow towards the SW as is evidenced by glacial striae and polish, roches moutonnes, and the deposition of erratic blocks up to 20 m in diameter (Valiquette, 1975).

The regional foliation is well developed locally with orientation ranging from 060/60 to 070/90, though the latter is most common in the vicinity of the pegmatite swarm (Valiquette, 1975). In the literature, no faulting has been directly observed in part due to glacial overburden, but there are some linear valleys that have been interpreted as zones of tectonic weakness (Valiquette, 1975). The author though has noted fault breccias in the vicinity of the pegmatite swarm (Figure 9, 10).

Figure 9: Fault breccia in granite, with angular fragments of granite cemented by hematite, 2km NE of the Whabouchi swarm and trending ~045°.

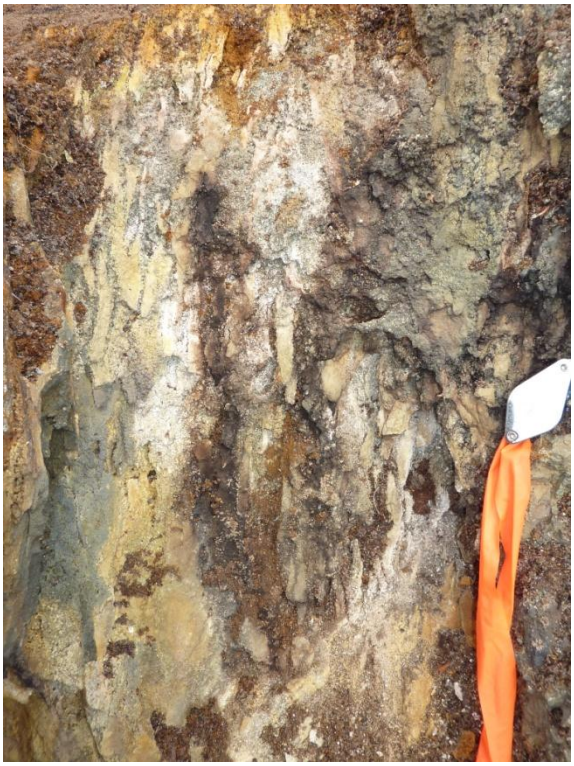

Figure 10: Strongly weathered fault breccia composed of fragments of a siliceous rock cemented with pyrite, located 2.5km SW of the Whabouchi swarm.

Whabouchi Pegmatite Description and Economic Geology

The swarm, hosted by oligoclase-bearing orthogneiss, is comprised of an approximately NE oriented series of sub-parallel and sub-vertical pegmatite dykes. The swarm is 1.3 km in length, with a maximum width of 130 m, and a depth greater than 300 m (Laferriere, 2009) (Figure 11,12). Based on drilling exploration conducted thus far, the pegmatites are macroscopically, texturally homogeneous and no zoning has been delineated (Laferriere, 2009). The Whabouchi pegmatites are composed of quartz, albite, spodumene, microcline and muscovite with accessory beryl, apatite and garnet (Laferriere, 2009).

Figure 11: Aerial photo of Whabouchi pegmatite dyke exposed at the surface, looking approximately South. The dyke is approximately 130 m wide and 1.3 km long.

Figure 12: Stripped trench at Whabouchi, showing the pegmatite (white) cutting its oligoclase gneiss host (dark grey). Field of view is approximately 15 m. Photo from Nemaska Exploration Ltd.

Mineralization in the Whabouchi pegmatites is primarily Li contained in spodumene and minor petalite (Figure 13,14) (Laferriere, 2009). Though much less, there is also minor Be mineralization in beryl, trace Rb in feldspar and trace Nb, Ta in Nb-Ta oxides (Laferriere, 2009).

A resource estimate conducted in 2009 for Nemaska Exploration Ltd. reported in the measured + indicated categories, a total of 9.8 Mt grading 1.63 % Li_2O, and approximately 450 ppm Be, which translates to 74, 000 t Li metal and 1600 t Be metal (Laferriere, 2009). In the inferred category 15.4 Mt were reported, grading at 1.57 Li_2O and 420 ppm Be, which translates to 112,11 t Li metal and 2300 t Li metal (Laferriere, 2009). Though there is much drilling exploration to be done to better delineate the economic potential of the Whabouchi pegmatite dykes, even with the limited data collected thus far it is clear that these pegmatites are a significant deposit of Li.

Figure 13: Core sample from Whabouchi, showing a large spodumene crystal in a matrix of smoky quartz, feldspar and fine grained mica. The core is approximately 3 cm in diameter and 25 cm long. Photo from Nemaska Exploration Ltd.

Figure 14: Core from Whabouchi pegmatites. Abundant mineralization is obvious by the notable green colour. Cores are approximately 3 cm in diameter and 1 m in length. Photo from Nemaska Exploration Ltd.

PEGMATITES: CLASSIFICATION AND PETROGENESIS

Pegmatites are igneous rocks, usually granitic in composition, with a highly variable grain size, often featuring directional growth habits (London, 2008). They may exhibit internal compositional zonation and/or be part of a continuum of a compositionally zoned field of pegmatites (London, 2008).

Classification

The classification of pegmatites is genetic, and based on specific chemical and mineralogical characteristics which are ultimately controlled by the source rock and depth of emplacement (London, 2008). Pegmatites are classified into families, classes, subclasses, types and subtypes (Table 2) .

Families describe the characteristic elemental enrichment. There are three pegmatite families: the Li-Cs-Ta>Nb (LCT), Nb>Ta-Y-F (NYF) and mixed LCT and NYF. However, it must be noted that it is not a requisite that all elements are equally enriched. In other words, relative enrichment in just one of the characteristic elements for a family is enough for the pegmatite to belong to that family. Alternatively, if a pegmatite's dominant chemical signature is of a certain family, that pegmatite may still contain, or be enriched in elements of another family.

The most abundant LCT family stands for Li, Cs and Ta>Nb, and pegmatites belonging to this family are relatively enriched in those elements, as well as Rb, Sn, Be, B, P and F (Cerny and Ercit, 2005). LCT pegmatites are typically peraluminous in composition, reflecting the composition of their parental magma (Cerny and Ercit, 2005). Magmas with LCT enrichment are believed to form either by anatexis of crustal sedimentary or igneous rocks at moderate or shallow depths (Cerny and Ercit, 2005).

The other pegmatite family is NYF, for Nb>Ta, Y and F relative enrichment (London, 2008). NYF pegmatites are peralkaline in composition, reflecting their subaluminous, moderately fractionated anorogenic (A)- or igneous (I)-type parent granites (Cerny and Ercit, 2005). This family is often also enriched in HREE, Be, Ti, Sc and Zr (London, 2008). NYF magmas may form by a number of processes, including differentiation from basaltic magmas, melting of juvenile igneous rocks, or mid-deep crustal rocks that were previously partially melted to remove LCT components, or melting of crustal lithologies enriched in NYF components by the circulation of mantle derived fluids (Cerny and Ercit, 2005).

Table 2: A summary of the genetic classification scheme for pegmatites, after Cerny and Ercit (2005).

TABLE 1. THE CLASS SYSTEM OF GEOLOGICAL, PARAGENETIC AND GEOCHEMICAL CLASSIFICATION OF GRANITIC PEGMATITES

Class	Subclass	Type	Subtype
Abyssal (AB)	AB-HREE		
	AB-LREE		
	AB-U		
	AB-BBe		
Muscovite (MS)			
Muscovite – Rare-element (MSREL)	MSREL-REE		
	MSREL-Li		
Rare-element (REL)	REL-REE	allanite-monazite	
		euxenite	
		gadolinite	
	REL-Li	beryl	beryl-columbite
			beryl-columbite-phosphate
		complex	spodumene
			petalite
			lepidolite
			elbaite
			amblygonite
		albite-spodumene	
		albite	
Miarolitic (MI)	MI-REE	topaz-beryl	
		gadolinite-fergusonite	
	MI-Li	beryl-topaz	
		MI-spodumene	
		MI-petalite	
		MI-lepidolite	

The mixed LCT+NYF family is rare, with only a few cases having been recorded. Fittingly, these pegmatites have intermediate enrichment patterns and mineralogy, and originate from LCT contamination of originally NYF melts (Cerny and Ercit, 2005). The NYF component is

consistently dominant over the LCT, which is only manifested as accessory phases (Cerny and Ercit, 2005).

Classes reflect the depth of emplacement of the pegmatite, as reflected by the metamorphic grade of host rocks (London, 2008). There are 5 classes: Abyssal, Muscovite, Muscovite-Rare-Element, Rare-Element and Miarolitic (London, 2008). Abyssal class pegmatites are emplaced at depth in high temperature-moderate pressure granulite facies hosts, commonly in polyphased metamorphic terranes (Cerny and Ercit, 2005). Usually formed by anatectic melts, abyssal class pegmatites generally take the form of relatively small injections of migmatitic leucosome, sometimes at the margins of larger accumulations of anatectic granite, and rarely derived magmatically from granites (Cerny and Ercit, 2005). There are 4 subclasses based on elemental enrichment: HREE, LREE, U, and B-Be, though abyssal pegmatites are rarely sufficiently mineralized for economic extraction (Cerny and Ercit, 2005).

Muscovite-class pegmatites are emplaced within high pressure amphibolite facies host rocks, and include pegmatites of a simple, granitic composition with no relative enrichment in rare elements or REEs (London, 2008). They are anatectic melts emplaced at higher pressures, but lower temperatures than the abyssal class, and are usually conformable with their hosts, indicating syn-deformational emplacement (Cerny and Ercit, 2005). Muscovite-class pegmatites can potentially be economic sources of industrial grade mica and feldspar, but no other mineralization is common (Cerny and Ercit, 2005).

The Muscovite-Rare-Element class is quite similar to the muscovite class, except these compositionally simple pegmatites are part of a continuum from granite to rare-element

pegmatite, while Muscovite-class pegmatites are formed by local anatexis of hosts (London, 2008). They are emplaced in hosts of moderate metamorphic grade, and are discordant with the regional foliation suggesting post-deformational emplacement (Cerny and Ercit, 2005). There are two subclasses, REE and Li, based on the relative enrichment of these elements (London, 2008).

Rare-Element class pegmatites are hosted by lower greenschist to amphibolite facies rocks, emplaced at shallow to moderate depth, and have widely variable compositions as they have been subject to different extents of fractionation (London, 2008). There are two distinct geochemical signatures for the two subclasses; REE, enriched in high field strength elements and Li, enriched in rare alkalis Li, Rb, Cs (Cerny and Ercit, 2005). The REE subclass melts are generally derived from post-orogenic to anorogenic peralkaline to peraluminous melts generated in extensional regimes, whereas the Li subclass melts form from syn- to post-orogenic peraluminous melts generated in compressional regimes (Cerny and Ercit, 2005). The REE subclass is further divided into 3 types to reflect their distinct mineralogy and geochemical signatures. REE subclass types are the allanite-monazite type, enriched in LREEs, the euxenite type, highly enriched in Y, with variable LREE:HREE, and lastly the gadolinite type, enriched in HREE with Y and Be (Cerny and Ercit, 2005). The Li subclass is highly variable in terms of enrichment and internal structure and is divided into 4 types: beryl type, complex type, albite-spodumene type and albite-type. The beryl type, Li subclass, rare-element class pegmatites are further subdivided into two subtypes: the beryl columbite and beryl columbite phosphate subtypes. Both subtypes are enriched in Be, Nb and Ta, with the only difference being a marked enrichment in P in the beryl columbite phosphate subtype (Cerny and Ercit, 2005). The complex

type, Li subclass pegmatites of the rare-element class have a characteristic enrichment in Li, often complex internal structures and the highest degree of fractionation (Cerny and Ercit, 2005). There is a further subdivision to 5 subtypes based on the bulk composition of parental melts and the pressure and temperature of crystallization, however they mostly reflect the dominant aluminosilicate (Cerny and Ercit, 2005). The subtypes are spodumene, petalite, lepidolite, elbaite and amblygonite, in order of increasing rarity (Cerny and Ercit, 2005). The albite-spodumene type of the Li subclass is very similar to the spodumene subtype, but with albite as the dominant feldspar over potassic varieties (Cerny and Ercit, 2005). Lastly, the rarest of the types of Li subclass of rare-element class pegmatites is the albite type, characterized by the occurrence of very fine grained albite in a greater proportion than quartz, with only minor to accessory lithium aluminosilicate minerals (Cerny and Ercit, 2005).

Finally, Miarolitic-class pegmatites are emplaced at shallow depths, as evidenced by the open or crystal lined cavities that characterize them and generally occur as segregations within granitic plutons rather than discrete, separate injections in their own (London, 2008). The miarolitic-class pegmatites are additionally divided into two subclasses which reflect the origin of the cavities. The REE subclass' miaroles arise from exsolution of vapour due to a sharp decrease in pressure during emplacement of anorogenic granites in the shallow crust, whereas the Li subclass' cavities originate from vapour exsolution caused by chemical and pressure quench during emplacement of a fertile, peraluminous granite (Cerny and Ercit, 2005). Based on miarole mineral assemblages, the two subclasses are even further subdivided; the former into 2 types and the latter into four, though these classifications are somewhat tenuous due to

the extremely variable mineralogy between miaroles within the same pegmatite (Cerny and Ercit, 2005).

Current Understanding of Pegmatite Petrogenesis

The current understanding of pegmatite petrogenesis is that they form by the rapid emplacement and subsequent crystallization of a low viscosity, hydrous and relatively flux (B, P, F) rich granitic melt that becomes significantly undercooled with a strong thermal gradient through the body, accounting for skeletal textures at the margins and coarse grained textures at the center (London, 2009).

Unidirectional growth textures, skeletal and fine grained textures found at the margins and in the wall zones of pegmatites are evidence for liquidus undercooling of the melts (London et al, 1989). Undercooling refers to crystallization of a melt far at a temperature far below the liquidus. Very high degrees of undercooling result in a high nucleation rate and a low growth rate which produces fine grained grained textures. Aplite units in pegmatites are a product of very high degrees of undercooling (Nabelek et al, 2010). However, smaller degrees of undercooling result in an increased growth rate and a reduced nucleation rate (Nabelek et al, 2010). Furthermore, significant liquidus undercooling suppresses the nucleation of crystals, requiring longer times for nucleation to begin (Nabelek et al, 2010). This phenomenon is called the nucleation delay. In their cooling-history model of a rare element pegmatite, Sirbescu et al (2008) determined that nucleation was suppressed until ≥240°C below the liquidus. Moreover, a granitic melt with 2, 4.6 and 6.5 wt % Li_2O, B_2O_3 and H_2O, respectively, experiences a nucleation delay of 9 to 14 days at 400°C (Nabelek et al, 2010). London (2009) also found that

the shortest nucleation delay that an H_2O saturated granitic melt at 200MPa undercooled by 175°C experiences is 200 hours, and saw no crystallization within the first 50°C below the liquidus temperature over 800 hours. Once nucleation can occur, it is concentrated at the contact between melt and host rock where undercooling is most significant (London, 2009). London (2009) attributes the aforementioned rapid crystallization of pegmatite melts to a strong chemical potential, driving crystallization in response to the suppression of nucleation by severe undercooling.

A large degree of undercooling at the contacts between pegmatite melt and host rock establishes a steep thermal gradient through the pegmatite body. In Sirbescu et al's (2008) cooling history model of a pegmatite dyke, they found that through conductive cooling, a thermal gradient of 170°C from core to margin persisted for 14 days. Their HEAT3D model is further supported by fluid inclusion studies on that same pegmatite that showed primary inclusions were trapped at a lower temperature than secondary inclusions (Sirbescu et al, 2008). This means that the fluid exsolved near the end of crystallization was hotter than the primary melt, and indicates the presence and maintenance of strong thermal gradients through pegmatite bodies from the onset of crystallization to the final stages of consolidation.

Coarse grain size has long been attributed to slow cooling rates, so giant pegmatite crystals were considered to have formed on the timescale of millions of years (London, 2008). Yet cooling rate models of pegmatites have shown that, depending on the size and geometry of the pegmatite body, and the temperature of the host rocks, crystallization is complete within hours to days after its onset (Nabelek et al, 2010). Sirbescu et al (2008) modelled the cooling

history of a lepidolite-spodumene hybrid subtype of the complex type, rare element lithium subclass using crystallization temperatures obtained from melt inclusions. They found that the dyke had fully crystallized within 14 days, from the margins to the core, though with considerable overlap in the timing of crystallization between zones (Sirbescu et al, 2008). Furthermore, they cite rhythmic, oscillatory textures as evidence for rapid crystallization where diffusion is the rate limiting step (Sirbescu et al, 2008).

Depending on their concentration of water and fluxes, pegmatite melts initially have a low to very low viscosity. The viscosity of a regular granitic liquid at 700°C was determined to be 10^5-10^6 Pa•s when the water content is ~ 6 wt % (London, 2005), and more recently as low as 10^3 Pa•s for 6-12 wt % H_2O (Nabelek et al, 2010). Therefore, pegmatite melts that are significantly enriched in fluxes are expected to have an even lower viscosity. For example, at 600°C, a granitic melt containing 17.3 wt % H_2O+F has a viscosity of 4.7 Pa•s (London, 2005). However, if a hydrous granitic melt is undercooled by approximately 250°C without losing any H_2O, it's viscosity will increase by several orders of magnitude, to 10^8 Pa•s (London, 2009). Consequently, pegmatite forming melts must be rapidly emplaced before significant undercooling takes place, since the undercooled, highly viscous melts are relatively immobile (Nabelek et al, 2010). In fact, London (2005) asserts that after emplacement, the pegmatite forming melt would be so exceedingly viscous that it would become semi solid or solid.

Most commonly, pegmatites have a simple, hydrous granitic bulk composition and are relatively poor in fluxing components (London, 2005). Such pegmatites are comprised mainly of quartz and feldspars with minor mica, are devoid of rare elements and complex internal

zonation, and what little fluxes are present are contained only in the accessory mineral assemblage (London, 2009). However, even the most highly fractionated, complexly zoned pegmatites do not exhibit enormously flux rich bulk compositions. The Tanco pegmatite, for example, has 9 different zones with a diverse and exotic mineral assemblage and is highly enriched in Li, Rb, Cs, and Ta, among others (London, 2008). Still, the the bulk composition of Tanco contains only 1 wt % total B, P and F, or up to 2 wt % total fluxes if those lost to the metasomatic halo in the host rocks are taken into consideration (London, 2009). Fluxes are still considered essential to pegmatite formation though, because they act to lower the melting and crystallization temperatures of the melt (London, 2005). Additionally, fluxes suppress the nucleation of quartz and feldspars, increasing the duration of the nucleation delay and allowing the melt to persist as a liquid at high undercooling (London, 2005). Fluxes also increase the solubility of H_2O in the silicate melt, sometimes to complete miscibility and thus the transition from silicate melt to aqueous fluid (London, 2005). Sirbescu et al's (2008) cooling model indicated that flux rich melts accumulated in the core of the pegmatite and exsolved an aqueous fluid at 700°C.

The above discussion leads into the two main paradoxes of pegmatite petrogenesis; how can mineral assemblages that are highly enriched in rare elements possibly form from melts whose bulk compositions are relatively low in such elements, and how are such coarse grain sizes possible in such a highly undercooled melt?

To address this first question, the London (2005, 2008, 2009) model operates on the basis of the formation of a flux rich boundary layer as a consequence of slow diffusion through

a highly viscous, highly undercooled melt (Figure 15). In other words, a high temperature, hydrous granitic melt slightly enriched in fluxes and rare elements is emplaced into much cooler host rocks and through severe undercooling, viscosity increases exponentially, nucleation rates are very low and a strong thermal gradient is established through the body. As the margins begin to crystallize common rock forming minerals such as quartz and feldspars, incompatible elements are rejected (London, 2005).

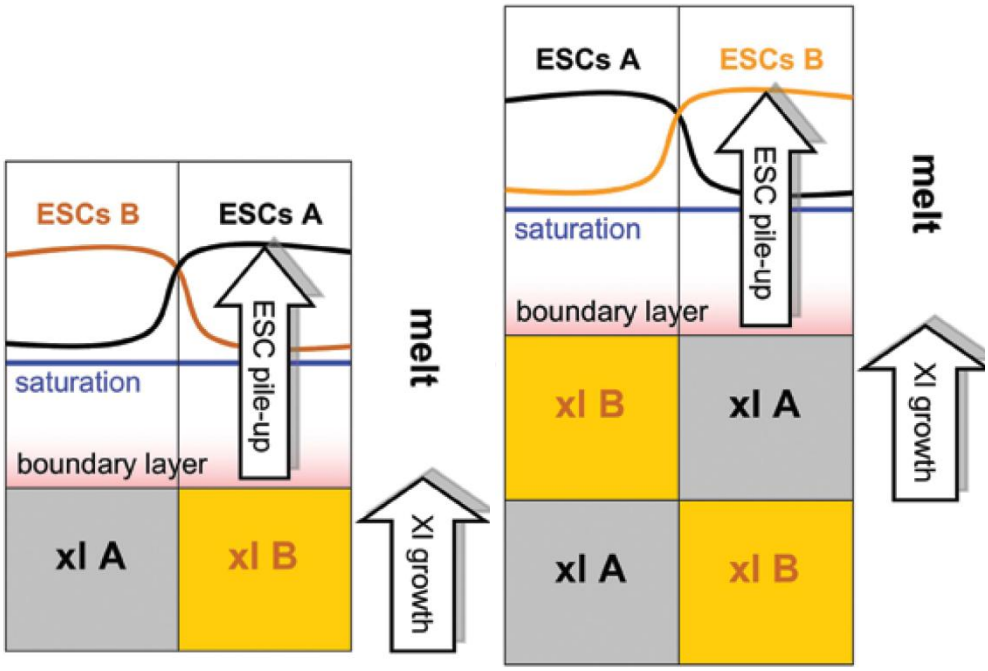

Figure 15: Schematic diagram illustrating the boundary layer model (Figure 9a,b, from London (2009). On the left, diffusion is slow in a viscous melt, and essential structural components (ESCs) build up at the crystal-melt interface. On the right, the ESCs have become saturated in the boundary layer due to slow vertical diffusion and crystallize minerals A and B.

Slow diffusion of incompatible elements away from the crystals through the extremely viscous melt allows for the build up of incompatible elements (including fluxes) at the crystal growth front (London, 2005). Consequently, a boundary layer between the bulk melt and crystal growth front develops, and has a bulk composition very different from that of the bulk

melt (London, 2009). According to this model, then, melt inclusions are likely to represent trapped boundary layer liquid rather than bulk melt (London, 2008). Concentration of fluxes in a boundary layer would further lower the solidus of the melt, encouraging it's persistence at even lower temperatures and increasing its miscibility with H_2O, thus locally decreasing the viscosity and enhancing diffusion through the boundary layer (London, 2005). With continued crystallization of common minerals, the volume of the boundary layer will increase and progressively become enriched in rare elements (London, 2008). Consequently, minerals rich in these elements will begin to crystallize from the flux-rich boundary layer rather than the bulk melt, once the boundary layer is saturated in the necessary crystal forming elements . They will continue to crystallize until the boundary layer becomes undersaturated in the essential constituents, and at the same time, by fractionation, become saturated in components required for a different mineral, resulting in sudden changes in mineralogy and oscillatory textures on both the macroscopic and microscopic scale (London, 2005). Sirbescu et al (2009) attributed the oscillatory mineral assemblages and mineral zoning they observed to the presence of flux-rich boundary layers ranging in width from <1mm to 100's of mm. The London model explains the formation of exotic primary minerals from a melt whose bulk composition is not exceedingly enriched in the necessary rare elements, as well as complex zonation in pegmatite bodies.

To address the contradiction of giant crystals in an undercooled melt, an alternative, though similar model of pegmatite petrogenesis was recently advanced by Nabelek et al (2010), operating on the basis that H_2O is the essential component for rapid emplacement and undercooling, and that large differences in Gibbs' free energy from margin to core of the body are the driving forces for crystallization. According to this model, a low viscosity, high

temperature and H_2O undersaturated granitic melt is emplaced adiabatically at depths equal to or shallower than the effective supersaturation pressure, resulting in H_2O saturation and superheating (Nabelek et al, 2010). By this mechanism, the pegmatite melt does not crystallize at all nor does it lose any of its H_2O during its ascent, and crystallization begins once transport has ceased (Nabelek et al, 2010). The authors propose that the retention of significant concentrations of H_2O by the melt delays nucleation to significant degrees of undercooling (Nabelek, 2010). In turn, steep thermal gradients from the margins to the core of the pegmatite body caused by severe undercooling result in large negative differences in Gibbs' free energy between the crystal growth front and the melt (Nabelek et al, 2010). Thus, once nucleation occurs, and assuming the necessary mineral forming constituents are available throughout the melt column, the crystal will grow inward to the distance in the melt where its liquidus temperature lies, and its size is governed by the distance between the site of its nucleation temperature, and that of its liquidus temperature (Nabelek et al, 2010). Crystal growth then ceases due to the now small difference in Gibbs' free energy, and another nucleation delay event occurs (Nabelek et al, 2010). With continued cooling of the pegmatite melt, the temperature at the new crystal growth front will eventually reach the nucleation temperature for a new mineral (or possibly the same one), and crystal growth will recommence (Nabelek et al, 2010). Also with continued cooling is the gradual flattening of the temperature profile, which promotes the growth of larger and larger crystals from margin to core, as the distance between their nucleation and liquidus temperatures gradually increases (Nabelek et al, 2010). Finally, continued fractionation of the melt by crystallization results in an accumulation of fluxes in the core that act to decrease undercooling and increase diffusivity so that crystal morphology

changes from unidirectional, elongate textures to blocky, coarse, equant textures (Nabelek et al, 2010). The Nabelek et al (2010) genetic model explains the presence of giant crystals in undercooled melts, as well as the commonly observed inward growth of crystals, differences in texture between the outer and inner zones and internal zonation of pegmatite bodies.

A third and highly contrasting model of pegmatite petrogenesis has been advanced through various melt –fluid inclusion studies led by Thomas and coworkers (Thomas et al, 2000, 2006, 2009, 2009b) that discounts the London model on a number of points. Thomas et al (2009b) explain that if the London model is correct, the boundary layer's composition should reflect the composition of the mineral that it is forming alongside, in the sense that it will contain all of the opposite constituents. For example, if quartz and feldspar are growing alongside each other, the boundary layer in contact with the quartz grain will become depleted in Si and enriched in Al relative to the boundary layer in contact with the feldspar, which will become enriched in Si and depleted in Al. Thomas et al (2006) found two types of melt inclusions consistently coexisting within different minerals from the same pegmatite and cite this as evidence that the different minerals crystallized from the same medium rather than from different boundary layers whose compositions are a function of the minerals they formed in front of. Similarly, in a study of melt and fluid inclusions in beryl from pegmatitic segregations in granite, Thomas et al (2009) found three coexisting, immiscible melt and fluid inclusions within the same growth zone, indicating that the three liquids were present simultaneously during the crystal's growth, again providing evidence which is inconsistent with the presence of a boundary layer. The three types of inclusions found are: a relatively volatile-poor aluminosilicate melt (12 wt % total H_2O, CO_2, F, Cl), a very hydrous aluminosilicate melt

(30 wt % H_2O) and a CO_2-H_2O rich supercritical fluid with ≤ 5 vol % aluminosilicates (Thomas et al, 2009). The compositions of the inclusions are mainly endmember compositions, though a few intermediate compositions from two or all phases do occur (Thomas et al, 2009). Most importantly, the proportions of the three immiscible liquids is fairly constant, indicating that they likely coexisted and that their simultaneous occurrence within the same growth layer of the beryl crystal is not coincidental (Thomas et al, 2009), nor do they represent a constantly fractionating boundary layer of variable composition. Moreover, Thomas et al (2009b) also state that if a boundary layer existed, it would be less dense than the surrounding melt and would therefore rise quickly to the roof of the body and away from crystal growth fronts. Though some pegmatites show concentric zoning, many actually *do* exhibit this texture of the coarsest textures and most fractionated compositions lying at the uppermost portions of the body (London, 2005).

Thomas et al (2009) postulate that the pegmatite forming medium is an H_2O-, Be-, B-, Li-, F-, Cl and CO_2-rich aluminosilicate melt that upon cooling splits into three immiscible liquids. On this basis, Thomas et al (2009) also downplay the importance of undercooling in pegmatite petrogenesis. In their melt inclusion study of miarolitic pegmatites, Thomas et al (2009b) describe the coexistence of two types of melt inclusion (and inclusions of intermediate composition) with vapour rich fluid inclusions of variable volume, which they interpret as evidence for a boiling fluid-melt system, implying the presence of a low viscosity melt. Accordingly, the liquidus temperature of such a volatile and flux rich melt would be much lower than that of a hydrous granite and so rather than being caused by severe undercooling, the low

crystallization temperatures of pegmatites could simply represent near- liquidus growth of crystals from a low viscosity, volatile rich melt (Thomas et al, 2009).

Through their extensive melt-fluid inclusion studies of pegmatites, Thomas et al (2000, 2006, 2009, 2009b) provide valuable insight into the nature of the pegmatite forming medium. However, their data alone cannot explain any of the characteristic primary textures of pegmatites, especially the unidirectional and skeletal undercooling textures at the margins. They suggest that the melt was extremely volatile and flux rich, which could explain the crystallization of rare element- and flux-rich primary minerals, but this is not supported by bulk compositions of pegmatites, nor can it explain abrupt transitions in mineralogy within pegmatite bodies. Alternatively, the London (2005, 2008, 2009) boundary layer model delineates a plausible mechanism for exotic primary mineralogy in a bulk composition with an overall low flux content, though this model does not provide a sufficient explanation for the driving force of crystallization, and does not acknowledge the extensive melt-fluid inclusion data compiled by Thomas et al (2009). Similarly, the Nabelek et al (2010) model ignores this pertinent research, accepting the London model's mechanism for the disagreement between primary mineralogy and bulk composition, and provides a thermodynamic explanation for primary textures and internal zonation of pegmatites.

METHODS

X-RAY DIFFRACTION (XRD)

Four samples were identified by XRD analysis (CB2010A10, CB2010A11, CB2010A12, CB2010A13). Small cores of each sample were obtained using a diamond coring bit, and except sample CB2010A13, were then crushed to a fine powder using a mortar and pestle. CB2010A13, a sample of mica, was reduced to powder using a small ring mill to reduce the potential for skewed results due to preferential crystal orientation. The tools were cleaned with quartz sand and ethanol between samples. Powdered samples were backloaded onto a glass slide for analysis to minimize preferential orientation of the grains. Data were acquired using a PW1050 powder diffractor with a Cu anode, a Ni filter to block Cu Kβ x-rays, and 1° slits. PANalytical XPert Quantify software was used to collect the scans, and XPert Highscore software was used to do a search and match routine using the ICDD-PDF2 database. The powder diffractor was operated at 40 kV and 40 mV in 0.2° steps at a rate of 1s/step, and data were acquired from 10 to 60° 2θ.

ZIRCON AND OTHER ACCESSORY MINERAL SEPARATION

Powdered sample CB2010A was processed through the Wilfley Table to separate out zircons. Initially, the sample was separated into light and heavy fractions. Next, the light fraction was repassed on the Wilfley Table, and the heavy fraction produced here was added to the initial heavy fraction. Then the total heavy fraction was again passed on the table and

separated into heavy and very heavy fractions. Lastly, the very heavy fraction was put on filter paper with ethanol, allowed to dry, and collected into a vial.

To get a heavy mineral concentrate from the very heavy fraction, first a hand magnet was passed over the sample. Next, the sample was passed through a heavy liquid separation using methylene iodide. The separated heavy fraction was then run through a magnetic Franz separation four times. The first 3 runs were conducted at tilt angles of 10° axial, 5° side, and with currents of 0.5, 1.0 and 1.7 A, respectively. The final run was conducted at 5° axial, horizontal side and with a magnetic current of 1.7 A. The resulting heavy mineral concentrate was picked through for zircons.

A yield of 112 zircons was obtained and then divided into two groups based on morphology; one consisting of 41 idiomorphic grains and another with 71 subhedral grains. The two groups were mounted separately in epoxy and are identified as samples CB2010Z1 and CB2010Z2, respectively.

The fractions obtained from the 0.5, 1.0 and 1.7 A were picked through for accessory minerals, initially believed to be titanite, epidote and garnet based on colour and morphology. The accessory minerals were mounted in epoxy and are identified as grain mounts CB2010BL, CB2010EP and CB2010GT, respectively.

All 5 mounts were polished first with 600 grit silica carbide sandpaper, then with 1500 grit. Then they were polished with 9 µm, then 1 µm oil suspended diamond on a polishing wheel, and finished by hand with 0.3 µm alumina on a polishing pad.

MODAL ANALYSIS

To determine the volumetric ratio of spodumene to quartz in spodumene-quartz intergrowths in four thin sections, CB2010A1 through CB2010A4, a JEOL-840 scanning electron microscope (SEM) with a Li-drifted silicon x-ray detector with an area of 10 mm^2 was used . I-XRF software was used for digital image capture and x-ray spectra analysis. To perform the modal analysis, back scattered electron (BSE) images were taken of the intergrowths at 20x magnification, using an accelerating voltage of 15kV and a current of 6 nA. The number of images of each spodumene-quartz intergrowth was dictated by their size, and only enough images were taken of each to approximately cover their surface area without overlap between images. For samples CB2010A1, CB2010A2, CB2010A3 and CB2010A4, 6, 20, 12 and 5 images were collected, respectively. Once an image was obtained, the segmentation tool in the I-XRF software was used to shade areas of the image with different colours according to the average atomic number (z). Each image was segmented into 4 sections from highest to lowest z, separating the highest z minerals, then spodumene and quartz, then the lowest z minerals. From each segmentation, a modal percentage of the image area was obtained for each of the 4 segments.

Next, the modal fractions of spodumene and quartz were obtained by subtracting the vol% of the highest and lowest z segments, and normalizing to total spodumene + quartz. Using densities of 3.16 and 2.65 gcm^{-3} (Cerny and Ferguson, 1972) for spodumene and quartz, respectively, the modal fractions were converted to mass fractions. A global average mass fraction of spodumene and quartz was then calculated from all of the 43 images.

SAMPLE IMAGING

An archive of representative images and notable textures from 19 thin sections was compiled using an Olympus BX51 transmitted light microscope equipped with an Olympus Q-color 3 RTV camera. Additionally, images of notable textures or unidentified minerals were compiled.

Using a JEOL-6610LV SEM operating at 20 kV and 8.3 nA , with an Oxford Instruments x-ray detector with an area of 20 mm^2 and manufacturer-provided software, a full BSE image archive of each individual grain in polished mounts CB2010Z1, CB2010Z2, CB2010GT and CB2010BL was obtained. Additionally, energy dispersive spectroscopy (EDS) was used for at least one spot on each grain to confirm their identities. Unidentified minerals from thin sections were similarly imaged and their identities were confirmed.

IN SITU TRACE ELEMENT DETERMINATION AND U-PB AGE DATING (LA-ICP-MS)

In situ trace element abundances and U-Pb ages were obtained from zircon by laser ablation inductively coupled plasma mass spectrometry (LA-ICP-MS). The analytical system uses a Newwave UP-213 Nd-YAG laser operating at 213 nm coupled to a VG-PQExcell ICP-MS with He gas flushing the ablation cell. Time-resolved software supplied by the manufacturer was used to acquire data, which was later reduced “off line” using GLITTER version 5.3 software supplied by Macquarie Research Ltd. ^{29}Si was used for internal standardization of trace element

data, with NIST 610 standard glass as the external calibration standard. For U-Pb age dating, zircon from the Sudbury Felsic Norite was used as the external calibration standard.

Trace Element Analysis

Fifteen of the zircon grains analyzed for uranium-lead ratios were also analyzed for the following isotopes of trace elements: ^{7}Li, ^{29}Si,^{31}P,^{43}Ca, ^{44}Ca, ^{46}Ti, ^{47}Ti,^{49}Ti,^{50}Ti, ^{56}Fe, ^{88}Sr,^{89}Y, ^{93}Nb, ^{139}La, ^{140}Ce, ^{141}Pr, ^{145}Nd, ^{146}Nd, ^{147}Sm, ^{149}Sm, ^{151}Eu, ^{153}Eu,^{155}Gd, ^{157}Gd, ^{159}Tb, ^{161}Dy, ^{163}Dy, ^{165}Ho,^{166}Er, ^{167}Er, ^{169}Tm,^{171}Yb,^{172}Yb, ^{173}Yb, ^{175}Lu, ^{177}Hf, ^{178}Hf, ^{179}Hf,^{181}Ta, ^{232}Th, and ^{238}U. Fifteen 10 µm spots were analyzed at 4 Hz and 70% laser output. The analyses were done for ablation times of 60 seconds, preceded by 20 seconds of background collection. The cell was flushed for at least 60 seconds between analyses. Analyses were performed in blocks of 20, with the first and last two done on the NIST-610 standard, at 10 Hz and 55% output.

The calculated abundances were normalized both to chondrite and silicate earth (pyrolite), using values from McDonough and Sun (1995).

U-Pb Age Dating of Zircon Grains

LA-ICP-MS was used to measure the following isotopes: ^{207}Pb, ^{206}Pb, ^{238}U, ^{232}Th. A total of 27, 10 µm spot analyses of unaltered portions, and 4, 10 µm targets of altered portions on 25 zircon grains were analyzed at 10 Hz and 70% output for 43s followed by a 60s washout. Each target was preceded by a 4-line raster with 6 µm spacing, at a rate of 40 µm/s to clean the surface of the grain before uranium-lead analysis. Analyses were done in groups of 3, bracketed by an analysis of zircon from the Felsic Norite of the Sudbury Igneous Complex, with known

ages of 1850 Ma. There was no correction for common lead (^{204}Pb) because it is present in extremely low abundances in zircon (Faure, 1977). Additionally, if ^{204}Pb were measured, there could be interference from ^{204}Hg in the argon, and to correct for this ^{202}Hg would have to be measured as well. Common Pb could be present in inclusions or alteration within the zircon and would result in discordant data biased towards the right on the concordia diagram. Measurement of ^{204}Pb, ^{204}Hg and ^{202}Hg is therefore unnecessary because discordant data were not used for the U-Pb age calculation. The results were plotted on concordia diagrams with two sigma uncertainties using Isoplot 3 . The reported age was determined using the upper intercept of a line from the origin through a cluster of likely concordant data with the concordia diagram. This line is the equivalent of the weighted average of the ^{207}Pb/^{206}Pb ages, which are more precise than U-Pb ages for Archean rocks because the system is unaffected by Pb loss (Faure, 1977).

RESULTS

PETROGRAPHY

The Whabouchi pegmatites are composed primarily of quartz (25-45%), feldspar (25-55%) and spodumene (15-30%), with minor mica and accessory garnet, apatite and beryl (Figures 16 - 21). The samples are mostly coarse grained, though CB2010F and CB2010G are much finer grained (Figure 20). Quartz occurs as colourless to smoky anhedral grains ranging in size from <1 mm to 1 cm. Though variable, spodumene can be especially coarse with crystals ranging in size from 0.5 x 1.0 cm to 7 x 15 cm. Spodumene is light green in colour and occurs

both as large euhedral laths and in intergrowths with quartz. Feldspar is white, and occurs both as coarse, euhedral crystals (up to 5 cm in length) and anhedral, sugary grains. Mica is generally light brown to beige and occurs both as mm sized flakes and euhedral booklets up to 4 cm in diameter. Garnet is dark red in colour and occurs in subhedral crystals ranging in diameter from 0.5 to 3 mm. Apatite is always fine grained (1 mm) and dark turquoise in colour. Beryl was observed in only one sample (CB2010G) as pale blue-green, euhedral, hexagonal crystals measuring up to 2 x 2 cm. Sample CB2010F is much finer grained, with an average grain size of approximately 3 mm. Except for one larger crystal measuring 1 x 2 cm, spodumene in this sample is much finer grained with laths measuring only 1-2 mm in length.

Graphic intergrowths of spodumene and quartz, and feldspar and quartz were identified (Figures 22, 23). In hand sample, spodumene-quartz intergrowths (SQI) can be up to 5 x 3 cm and feature vermicular, colourless quartz grains within spodumene crystals.

Texturally, the pegmatites lack any evidence for metamorphism; the regional foliation is not developed in these rocks. Full descriptions of hand samples are given in Table 3

.

Table 3: Modal abundances and textures of hand samples

Sample	% Quartz	% Feldspar	% Spodumene	% Mica	% Garnet	% Beryl	% Apatite	Textural Notes
CB2010A	35	25	20	20				Spodumene crystals mostly very coarse grained, measuring up to 3 x 12 cm. Also appears as small, mm crystals. Mica occurs as booklets up to 4cm in diameter, as well as mm flakes. The sample, as a whole, is coarse grained.
CB2010B	34	25	30	10			1	Spodumene is coarse grained, up to 7 x 15 cm, with a few mm crystals. Mica is light coloured and occurs in small booklets. Very few, mm sized, turquoise coloured apatite grains. Spodumene and quartz intergrowths appear on surface of sample.
CB2010C	25	55	15	4	1			Large, coarse grained spodumene crystals set in a matrix of sugary, fine grained quartz and feldspar. Quartz is colourless, with a small proportion of the smoky variety. Spodumene crystals are coarse grained, 1-2cm in length, 0.5-1cm in width. Garnets are dark red in colour, approximately 3mm in diameter, and occur largely as aggregates in small voids within sample. Mica is light in colour and occurs as small, mm flakes or booklets measuring 1 cm in diameter.
CB2010D	45	29	25	1	TR			Quartz crystals are round, and coarser grained, ≤1cm width. Spodumene is coarse grained, measuring 0.5 to 10cm in length. Trace amounts of garnets dark red in colour and measuring 0.5mm in diameter. The mica is light in colour. The sample is coarse grained overall, and mica-poor compared to other samples.
CB2010E	35	29	15	20	1			Spodumene is coarse, measuring 1-5cm in length. Quartz is colourless, with minor smoky variety, and occurs as both coarse (≤1cm) and fine, sugary grains. Feldspar is white, and occurs either as coarse crystals (≤5cm in length) or sugary grains. Garnet is dark red in colour and millimetric. Some mica flakes, light in colour, are seen in large spodumene crystals. Also, a small vein (2 mm width) of fine grained, sugary feldspar cross cuts a spodumene crystal.
CB2010F	49	30	20	1			TR	Spodumene is mostly fine grained (1-2mm), but one crystal measuring 1 x 2 cm. Quartz also mostly fine grained (1-3mm), with a few crystals measuring 3-5mm. Feldspar has a sugary texture and is white. Possible presence of labradorite (?). Mica is dark in colour. Apatite occurs as mm, turquoise coloured grains. There is some quartz and spodumene intergrowth on the surface of the sample. The sample is oddly porous, about 5% pores on surface. Also, one side of the sample is extremely smooth. The sample is overall much finer grained compared to the others.
CB2010G	25	35	20	15		5	TR	Spodumene occurs as both fine grained (mm) and coarse grained (≤2x10cm) crystals. Feldspar also ranges in size from millimetric to 1x2cm. Quartz ranges in size from mm to 1cm crystals. Mica is light in colour (muscovite?) and occurs as booklets as well as small flakes. Beryl is pale blue-green in colour and occurs as idiomorphic, hexagonal, coarse grained crystals measuring up to 2x2cm. Apatite is fine grained (mm), and turquoise in colour. It appears that there is some alteration to clay minerals.

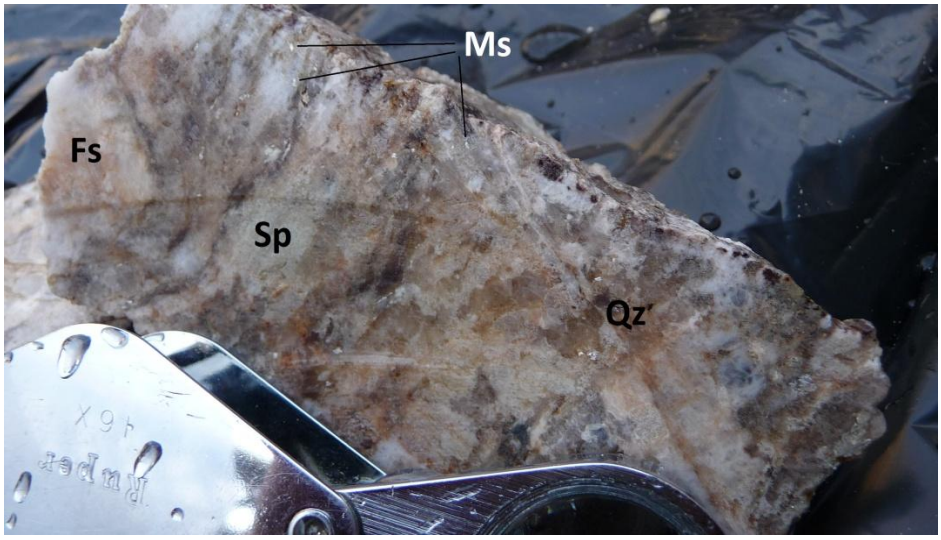

Figure 16: Photograph of sample CB2010E showing the major mineralogy, where Sp is spodumene, Fs is feldspar, Qz denotes quartz and Ms is muscovite. Hand lens is 3 x 10 cm.

Figure 17: Light green spodumene laths, outlined in black for visibility, from CB2010B. Hand lens is 3 x 10 cm.

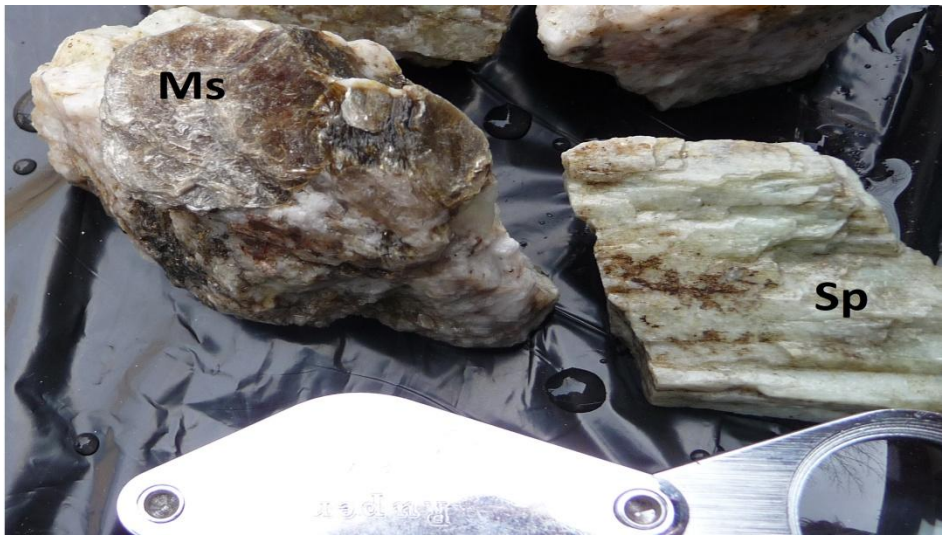

Figure 18: Pieces of coarse grained muscovite booklets and spodumene lath, from CB2010B. Hand lens is 3 x 10 cm.

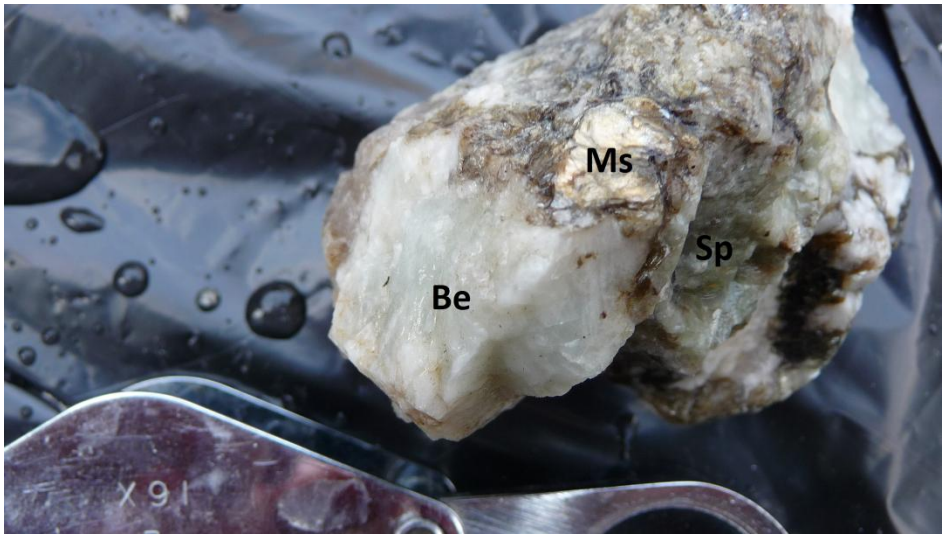

Figure 19: Beryl (Be) is very pale, milky blue green, with coarse muscovite and spodumene, from sample CB2010G. Hand lens is 3 x 10 cm.

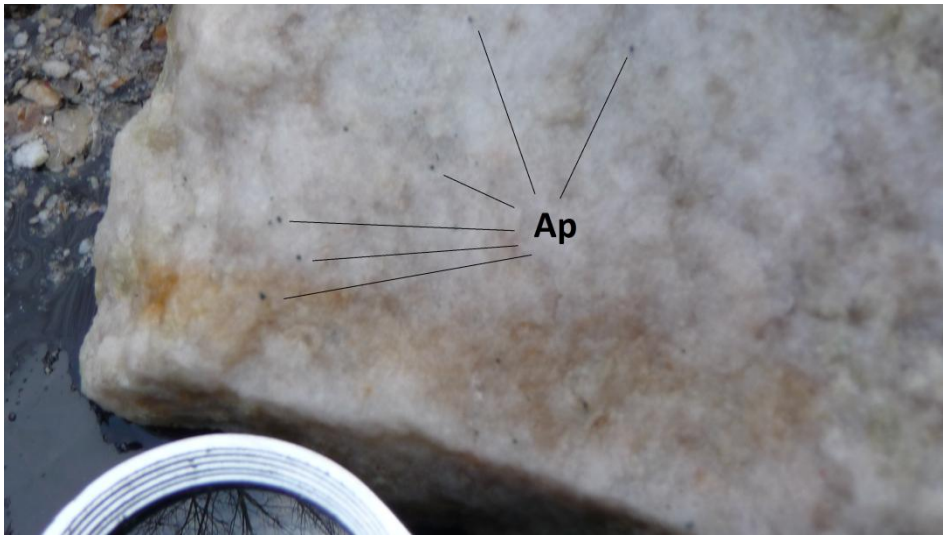

Figure 20: Mm grains of dark blue-green apatite (Ap) in sample CB2010F with aplitic texture. Hand lens is 3 x 10 cm.

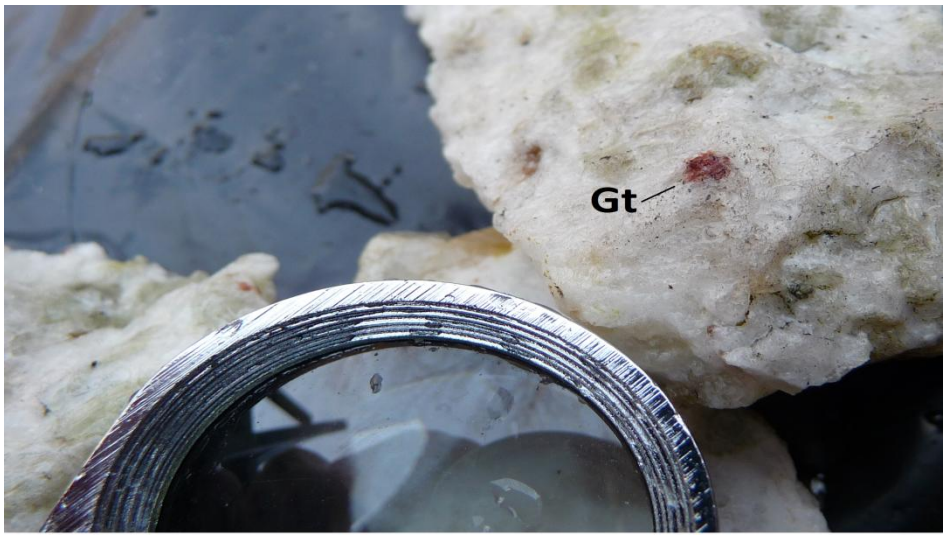

Figure 21: Large garnet crystal, 3 mm in diameter, in sample CB2010D. Hand lens is 3 x 10 cm.

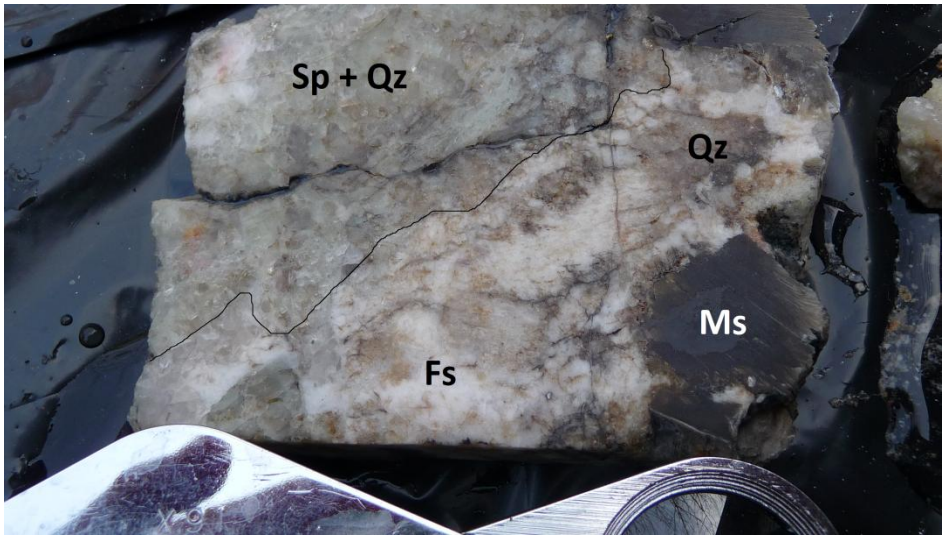

Figure 22: Spodumene-quartz intergrowth (Sp+Qz), outlined in black for visibility. Slab cut parallel to c-axis of muscovite, rendering it dark in colour with a dull luster. Quartz is smokey. Hand lens is 3 x 10 cm.

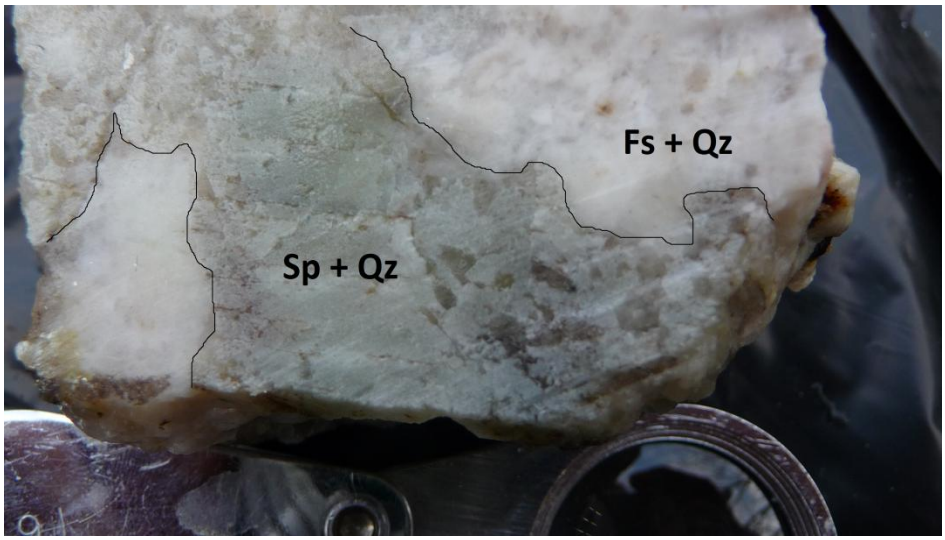

Figure 23: Green spodumene-quartz intergrowth bounded by graphic feldspar and quartz intergrowths. Hand lens is 3 x 10 cm.

Modal abundances obtained from thin section analysis agree with those from the hand samples, and the average modal abundances of quartz, plagioclase and spodumene are

approximately 40, 20 and 30 %, respectively. Modal abundances of thin sections are given in Table 4, and their textural descriptions are given in Table 5. Representative photomicrographs are given in Figures 24 a and b. While beryl was identified macroscopically, it was not observed in thin section. Thin section studies also revealed the presence of minor microcline and trace ferromanganese phosphate and orthoclase (Figures 25 - 27). Orthoclase commonly appears in aggregates at the interstices of other mineral grains such as microcline, plagioclase, quartz and spodumene (Figure 28).

Table 4: Modal Abundances of Whabouchi Pegmatite Thin Section

Sample	% Quartz	% Plagioclase Feldspar	% Microcline	% Orthoclase	% Spodumene	% Muscovite	% Garnet	% Apatite	% Ferromanganese Phosphate	% Fluid-Melt Inclusions
CB2010A1	35				65					
CB2010A1B	40	1			55	2	2			
CB2010A2	30				70					
CB2010A3	45	10			40	3		2		
CB2010A4	40	35			20	5				
CB2010A4B	25	35		4	20	13		3		
CB2010B1	40	23			30	5		2		
CB2010B1B	45	5		TR	30	15		5		
CB2010B2					100					
CB2010C1	44	15	30	4	5	1	1			
CB2010C2	40	30	15	1	7	5	2			
CB2010D1	30	7	20		40	3	TR		TR	
CB2010D2	40	9	15		30	1				5
CB2010E1	34	25	1		25	3	1	1		
CB2010E2	38	17	15	5	10	10		TR		5
CB2010F1	40	28		5	20	2		2	3	
CB2010F2	47	30			20	2		1		
CB2010G1	43	50				5	TR	2		
CB2010G2	52	30			15	3				

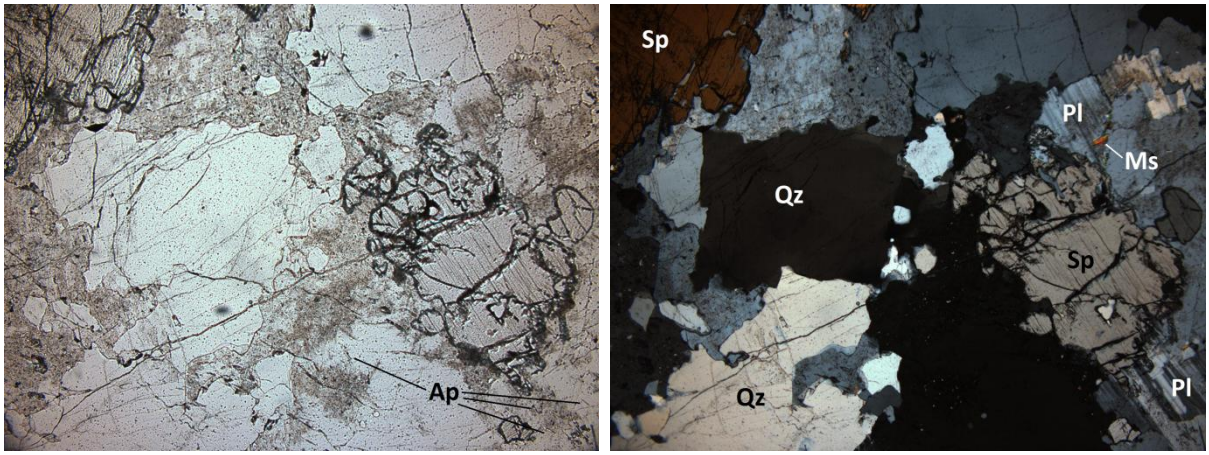

Figure 24 A) A representative, transmitted light photomicrograph in plane polarized light, of sample CB2010F1. Field of view is 4.5 mm. High relief spodumene, with quartz, plagioclase (Pl) and small grains of muscovite. B) Same image, cross polarized light.

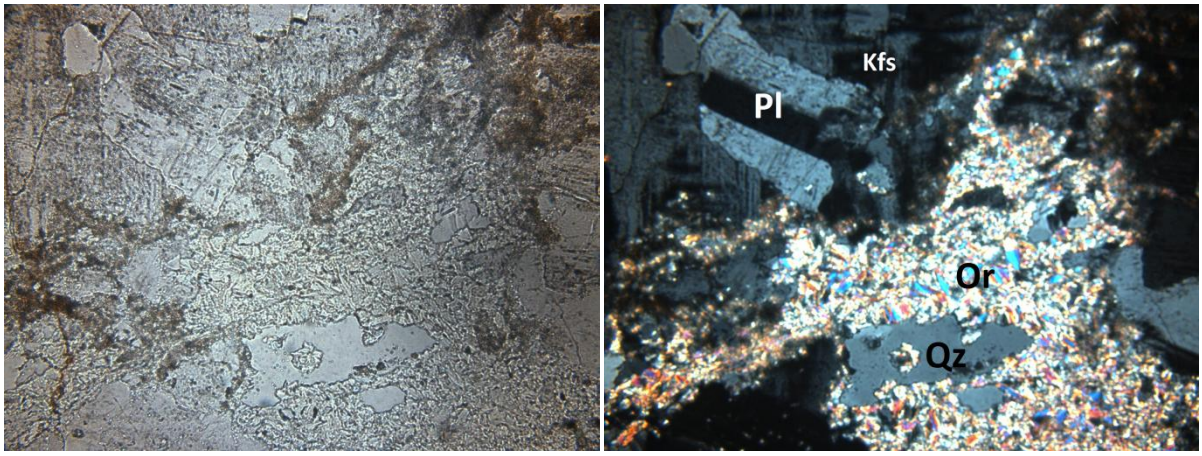

Figure 25: A) Transmitted light photomicrograph in plane polarized light of fine grained, radiating aggregates of high relief orthoclase (Or) at the interstices of quartz, microcline (Kfs) and plagioclase. Field of view is 4.5 mm across. B) Same image, cross polarized light.

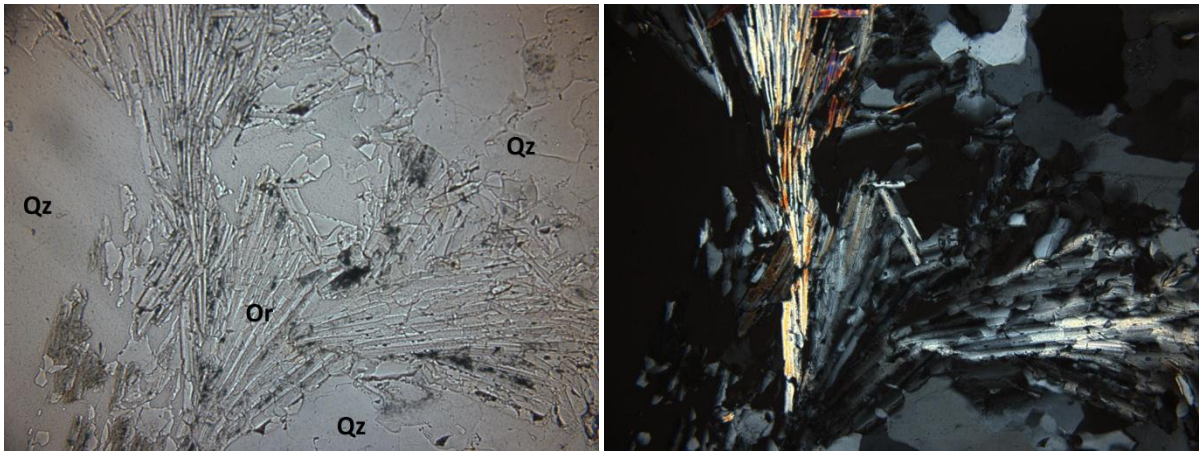

Figure 26: A) Transmitted light photomicrograph in plane polarized light of high relief orthoclase with a coarser, elongate, bladed morphology, in a quartz groundmass. Field of view is 4.5 mm. B) Same image, cross polarized light.

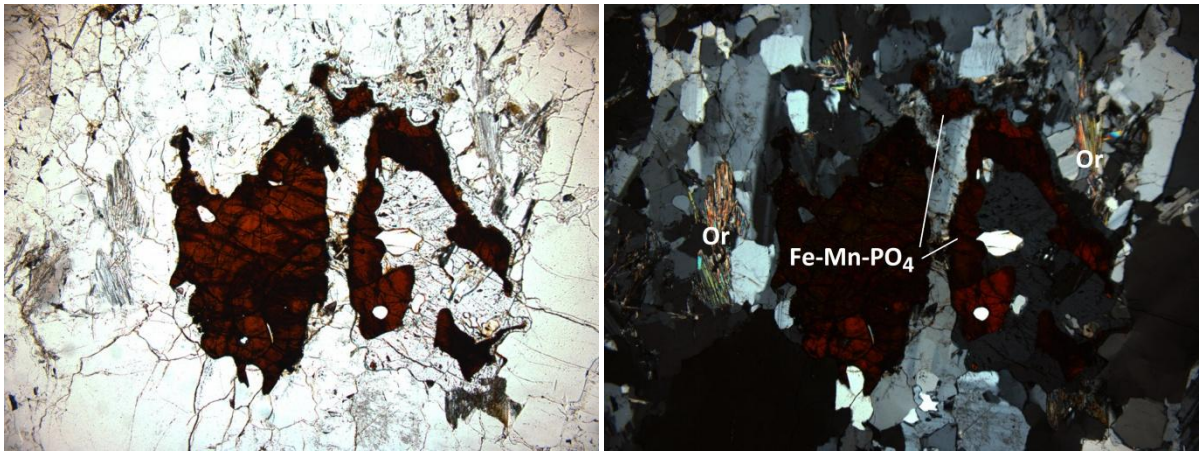

Figure 27: A) Transmitted light photomicrograph in plane polarized light of opaque, red coloured ferromanganese phosphate in a groundmass of quartz with lesser feldspar. Aggregates of bladed orthoclase. Field of view is 4.5 mm. B) Same image, cross polarized light.

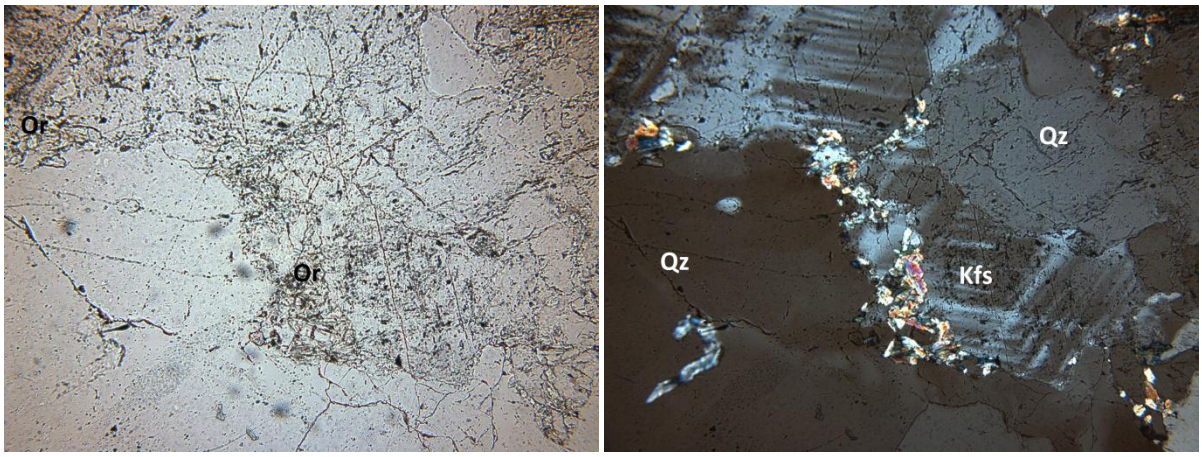

Figure 28: A) Transmitted light photomicrograph of fine grained, radiating aggregates of orthoclase at the interstices of microcline and quartz crystals. Field of view is 2.2 mm. B) Same image, cross polarized light.

Spodumene-quartz graphic intergrowths are highly abundant throughout the samples, accounting for 2 to 60 modal % (mean = 28 %)(Figures 29, 30) though both minerals also occur independently. Graphic intergrowths of quartz and feldspar (in samples CB2010C, CB2010G, less than 10 modal %) and once, quartz and muscovite, were also identified (Figures 23 and 31, respectively). Analysis of heavy mineral separates from crushed sample CB2010A also revealed the presence of accessory gahnite, a Zn-spinel, and columbite-tantalite.

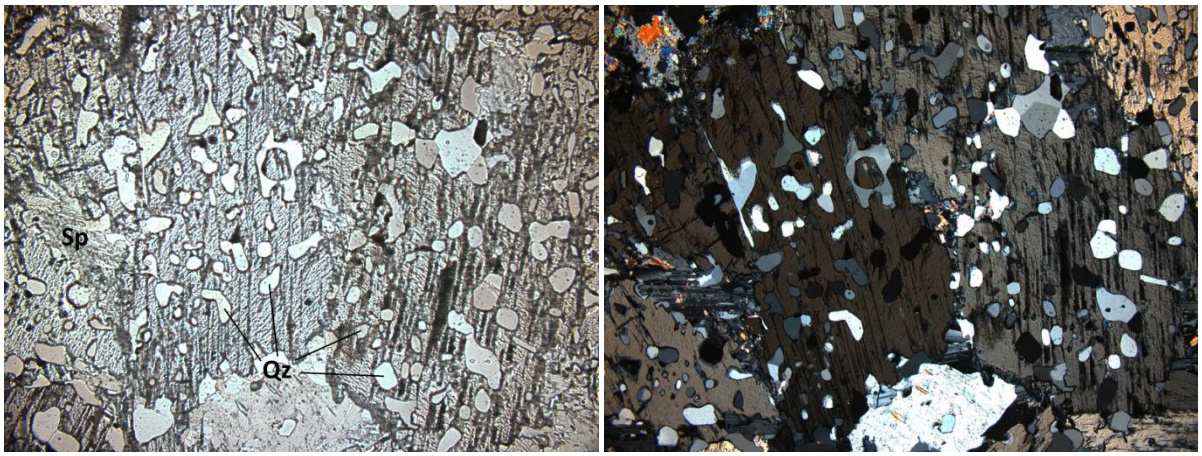

Figure 29. A) A transmitted light photomicrograph, plane polarized light, of spodumene-quartz intergrowths. Field of view is 4.5 mm. B) Same image, cross polarized light.

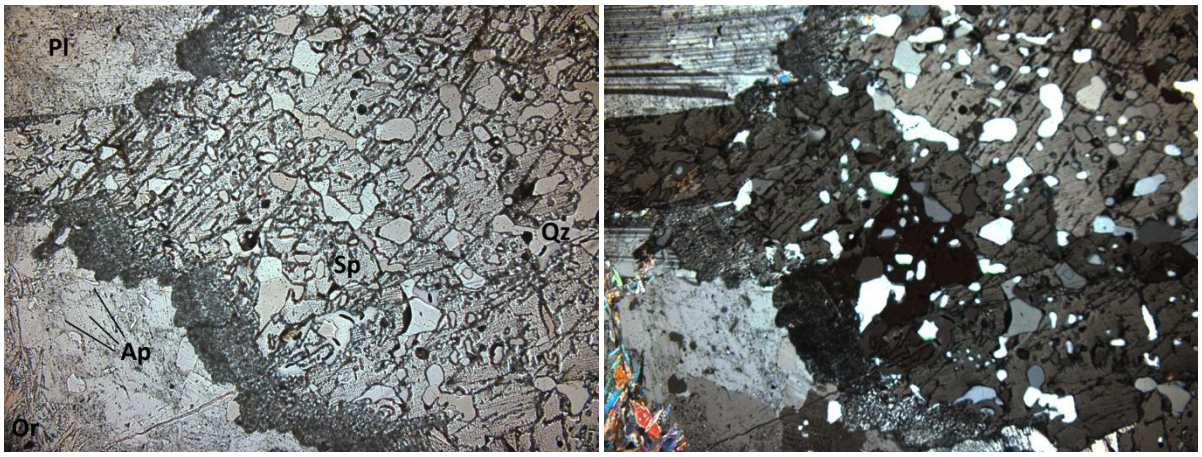

Figure 30: A) Transmitted light photomicrograph, plane polarized light, of spodumene-quartz intergrowths, bounded by plagioclase and orthoclase. Note the much finer grain size of the intergrowth at the margins. Field of view is 4.5 mm. B) Same image, cross polarized light.

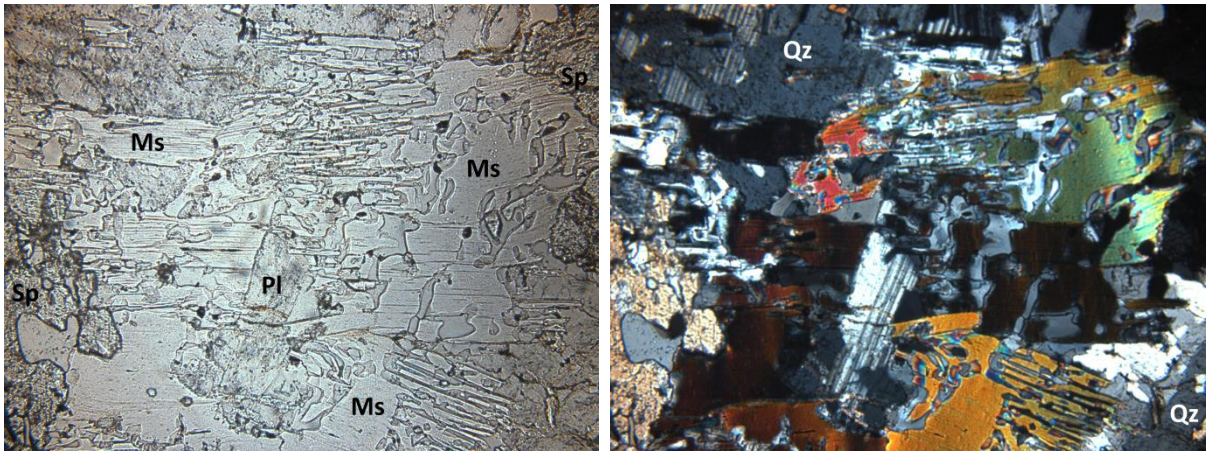

Figure 31: A) Transmitted light photomicrograph, plane polarized light, of symplectic texture in coarse grains of muscovite. Field of view is 4.5 mm. B) Same image, cross polarized light.

A mineralogical study of the Whabouchi pegmatites was conducted by SGS Canada Inc. for Nemaska Exploration Ltd. Those results are in general agreement, although the work identified petalite by XRD analysis in 3 of 6 samples. An effort was made to identify petalite both macro- and microscopically, however it was not observed in this study.

Table 5: Textural relationships observed in thin section

Sample	Textural Notes
CB2010A1	A thin section through a spodumene-quartz intergrowth.
CB2010A1B	A thin section through a spodumene-quartz intergrowth and one large spodumene crystal. There are two coarse grained crystals of garnet as well, measuring 3 x 2 mm and 1 mm^2.
CB2010A2	A thin section through a spodumene-quartz intergrowth. Mostly a large, euhedral spodumene crystal with inclusions of quartz grains.
CB2010A3	Two thirds of the thin section is comprised of fairly fine grained (1 mm length) plagioclase with quartz, muscovite, and small, high relief elongate sections of apatite, the remainder is a spodumene-quartz intergrowth. Approximately 15% of the spodumene is in discrete grains, while the rest is in the intergrowths.
CB2010A4	About half of the thin section is a spodumene-quartz intergrowth, and the other half contains coarse (up to 3 mm) crystals of plagioclase feldspar, fine grained mica and quartz grains ranging in size from <0.5 mm to 2 mm.
CB2010A4B	Coarse grained, euhedral quartz, plagioclase and spodumene-quartz intergrowth surround a pocket of fine grained (<0.5 mm) plagioclase, quartz, muscovite, apatite with coarser, radiating orthoclase with low 1^{st} order birefringence.
CB2010B1	Spodumene -quartz intergrowth bordered by one large spodumene crystal, coarse grained muscovite and euhedral plagioclase and quartz.
CB2010B1B	Radiating, low 1^{st} order birefrigence orthoclase occurs within an altered looking spodumene crystal. Quartz is coarse grained (>4.5 mm) and contains abundant inclusions of apatite. Muscovite varies in grain size from <0.5 mm in length to grains measuring 6 x 2 mm.
CB2010B2	A thin section through a single spodumene crystal.
CB2010C1	Graphic texture is abundant throughout with quartz, potassic and plagioclase feldspars, but not spodumene here. Rosettes of fine grained, radiating orthoclase fill fractures, especially within potassic feldspar, but also occur at interstices of quartz and feldspars. Less commonly, orthoclase occurs as elongate, fibrous crystals with 2^{nd} order birefringence. Muscovite is fine grained (<0.5 mm) and occurs as small inclusions within coarser grains.
CB2010C2	Quartz, spodumene, potassic feldspar and muscovite are coarse grained, with some finer plagioclase and orthoclase, and pockets of graphic quartz and feldspar
CB2010D1	There is one large (2 mm diameter) of garnet, and a few small crystals of fine grained (<0.5 mm) ferromanganese phosphate. Muscovite is coarse grained (up to 4.5 mm in length) and subhedral. In some instances, it forms graphic intergrowths with quartz, though spodumene does not in this sample.
CB2010D2	Quartz, potassic feldspar, plagioclase and spodumene are coarse grained while muscovite is rare and very fine grained.
CB2010E1	Quartz occurs as euhedral to subhedral crystals, ranging in size from submillimetric to millimetric, as well as myrmekitic crystals in spodumene, especially at the edges of the crystals. Spodumene is high relief and euhedral. Muscovite occurs as a few coarse grains, and there is one large crystal of garnet. Notable textures include rosettes of min "x" at interstices of quartz and plagioclase.
CB2010E2	There are tiny inclusions (<0.1 mm) throughout the sample. Muscovite is very coarse grained with crystals up to 4.5 mm in length. Quartz and plagioclase occur as coarse grains, as well as very fine grained pockets with orthoclase. Orthoclase is also found at the interstices between feldspars and quartz in radiating needles.
CB2010F1	Large variation in grain size; quartz occurs as myrmekitic growths mostly in spodumene, but also in plagioclase and distributed randomly throughout the sample, as well as euhedral crystals. Plagioclase also varies largely from very fine, anhedral to coarse euhedral grains. Spodumene is coarse grained and contains myrmekitic growths of quartz concentrated at the edges of grains. Orthoclase is low 1^{st} to 2^{nd} order birefringent, and occurs in fibrous, elongate grains up to 2 mm in length.
CB2010F2	Spodumene varies largely in grain size, from <0.5mm to 1 mm in length. Muscovite is very fine grained, and there are a few clusters of radiating, elongated crystals.
CB2010G1	Fine grained inclusions of elongate muscovite and of hexagonal basal sections and elongate sections of apatite, in euhedral plagioclase and quartz.
CB2010G2	Muscovite occurs as small, <0.5 mm crystals within quartz and plagioclase. Quartz occurs both as subhedral crystals and as a graphic intergrowth with both spodumene and plagioclase.

X-ray Diffraction

Compositions of samples CB2010A10, CB2010A11, CB2010A12, and CB2010A13 were determined by XRD analysis. CB2010A10 and CB2010A13 were determined to be spodumene and muscovite, respectively (Figures 32, 33). Sample CB2010A11, a composite sample of white minerals, was determined to be composed of albite and quartz (Figure 34). PANalytical Xpert Highscore software's quantification tool uses the relative intensity ratio (RIR) of a mineral to determine its abundance in a mixture. The RIR is the intensity of the main peak of a given mineral in a mixture, over the intensity of that same peak in a pure sample. This quantification tool can only provide a good estimate of proportions if all phases present have been identified. The proportions of albite and quartz were quantified using this tool and were determined to be 40 and 60 %, respectively. Sample CB2010A11 likely contained only feldspar and quartz, though the possibility remains that trace minerals were included in the core, therefore the proportions determined using this tool provide only a rough estimate. Sample CB2010A12, a sample of graphic intergrowth, was determined to be composed of spodumene and quartz (Figure 35). Their proportions were approximately quantified as 37 % spodumene and 63 % quartz using the quantification tool.

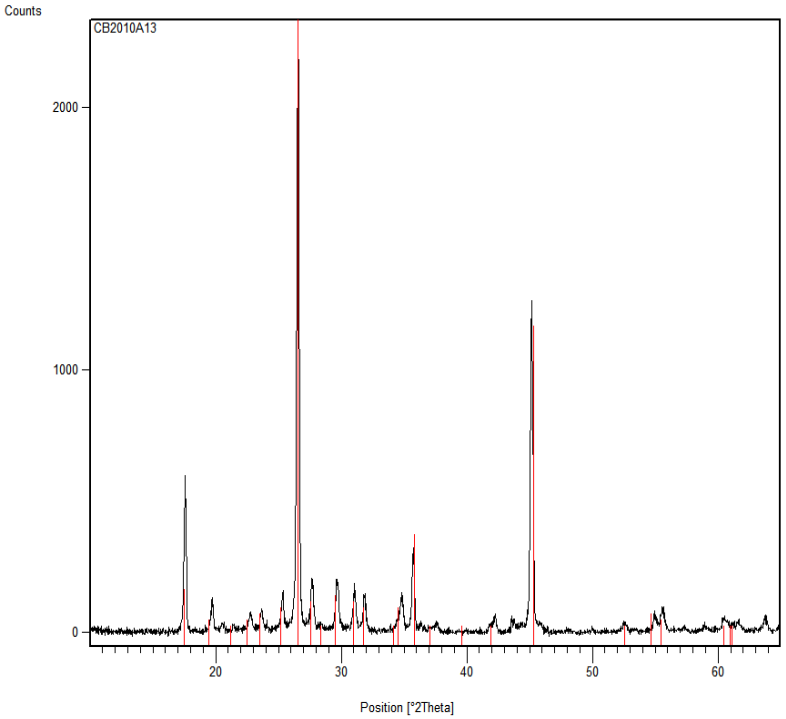

Figure 32: XRD spectra, portraying counts as a function of 2θ for CB2010A10 in black, with peak locations for spodumene in red.

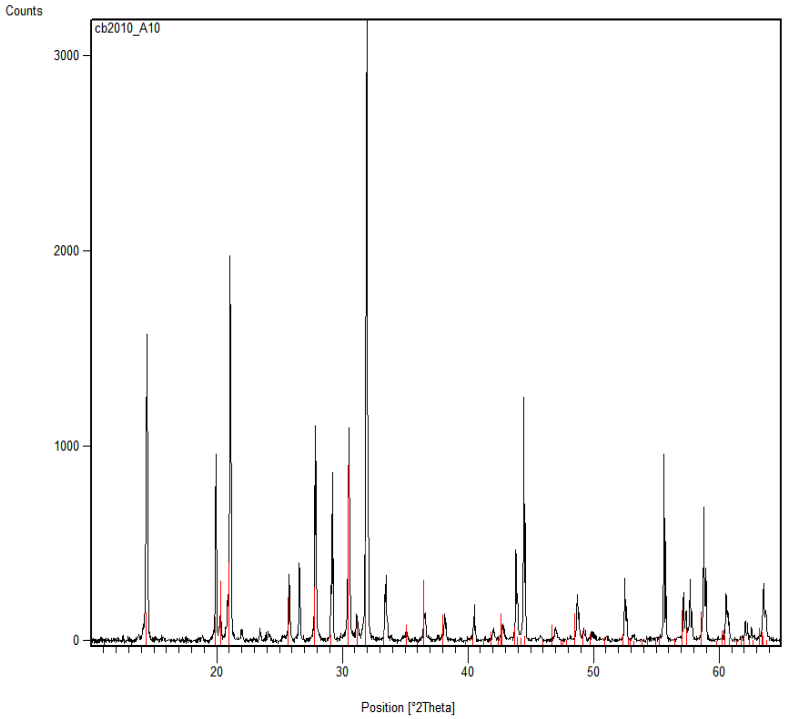

Figure 33: XRD spectra portraying counts as a function of 2θ for CB2010A13 in black, with peak locations of V-Ba-muscovite in red.

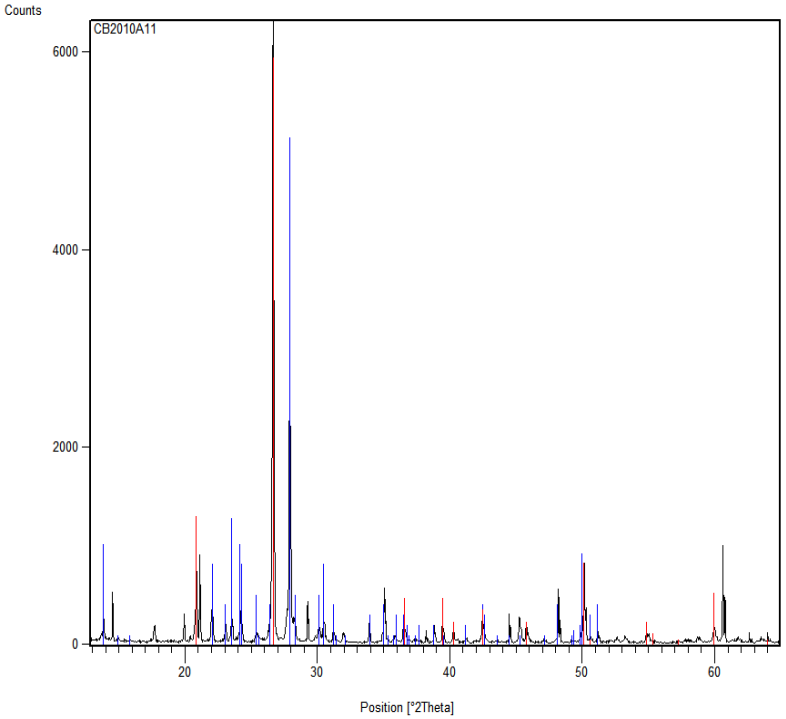

Figure 34: XRD spectra, with counts as a function of 2θ for sample CB2010A11 in black, with peak locations of quartz in blue, and albite in red.

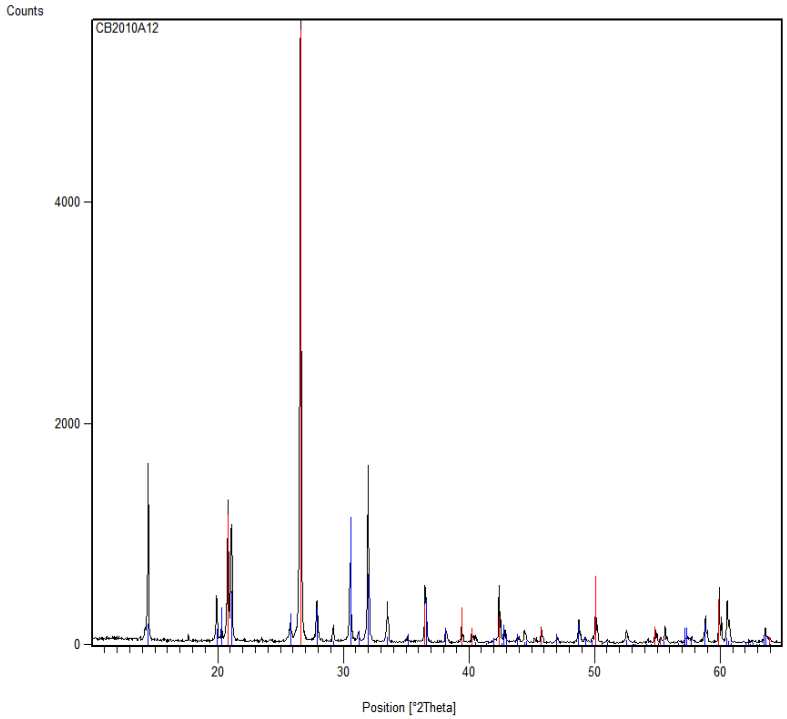

Figure 35: XRD spectra showing counts as a function of 2θ for sample CB2010A12 in black, with peak locations for quartz in red and spodumene in blue.

Modal Analysis

The mass fractions of spodumene and quartz in the intergrowths was determined through segmentation of 43 fields of view at 20x (25.2 mm^2) of spodumene-quartz intergrowths in 4 thin sections. On average, the intergrowths contain 44.93 ± 3.68 % spodumene and 55.07 ± 4.52 % quartz. Errors are 1 sigma. Figure 36 (a, b) are representative images of the segmentation results.

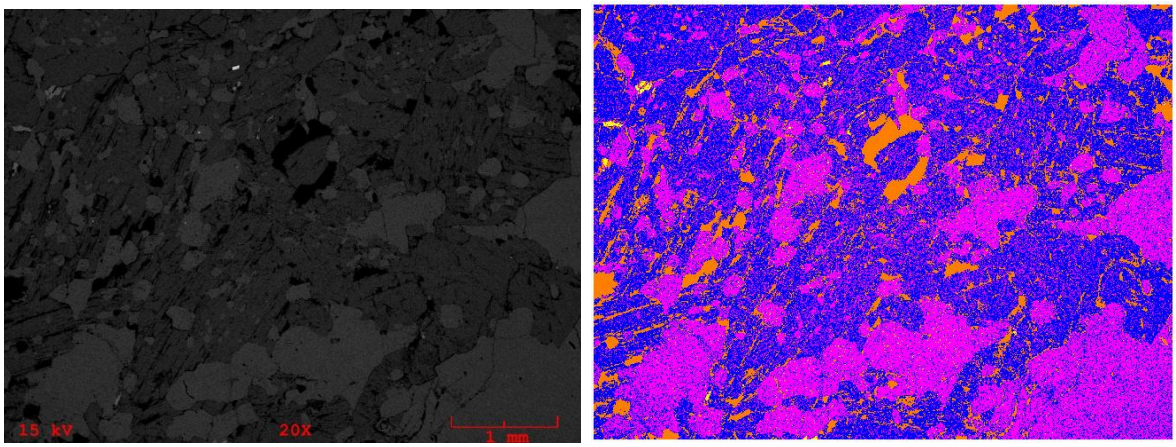

Figure 36: A) Representative BSE image of a spodumene-quartz intergrowth. Quartz and spodumene are dark and light grey, respectively. B) Same image, segmented. Quartz is in blue, spodumene in pink. Yellow areas are high average atomic weight grains while orange areas are low average atomic weight grains.

ZIRCON: TEXTURES, TRACE ELEMENT COMPOSITION AND U-Pb AGE

Images and Textures

Zircons from the Whabouchi pegmatite dyke are metamict and radially fractured, but to varying degrees. Metamictization and fracturing promote infiltration of fluids and subsequent alteration of the zircon grains. Many of the grains exhibit oscillatory zoning, considered a primary texture in igneous zircon (Nasdala et al, 2009)(Figures 37 a,b). However, primary

zoning is often partially or completely destroyed by alteration, and a porous texture is developed (Figures 38 a, b). Alteration is distinguished from pristine portions of zircon by its darker colour in back scattered electron images. Fluids change the chemical composition of the zircon, and result in zircon grains with Ca ± Fe ± Al ± Mn and the loss of Zr, therefore a lower average atomic weight and a darker colour in BSE images (Nasdala et al, 2010). Alteration has been observed both as lobate fronts and following fractures and/or internal zoning (Figures 39 a-d). In other cases, the alteration cuts across all zoning and textures with no discrimination (Figure 40).

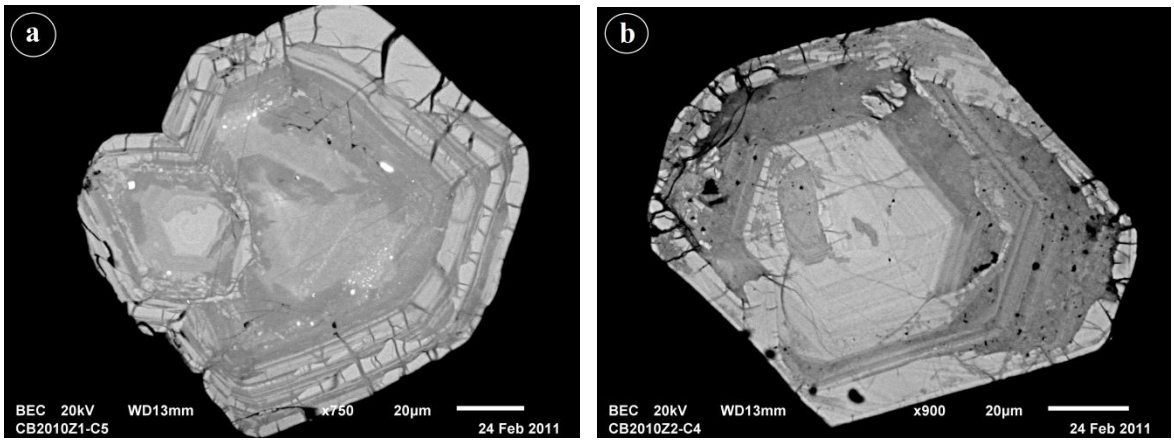

Figure 37: A and B) BSE images of oscillatory zoning in zircon.

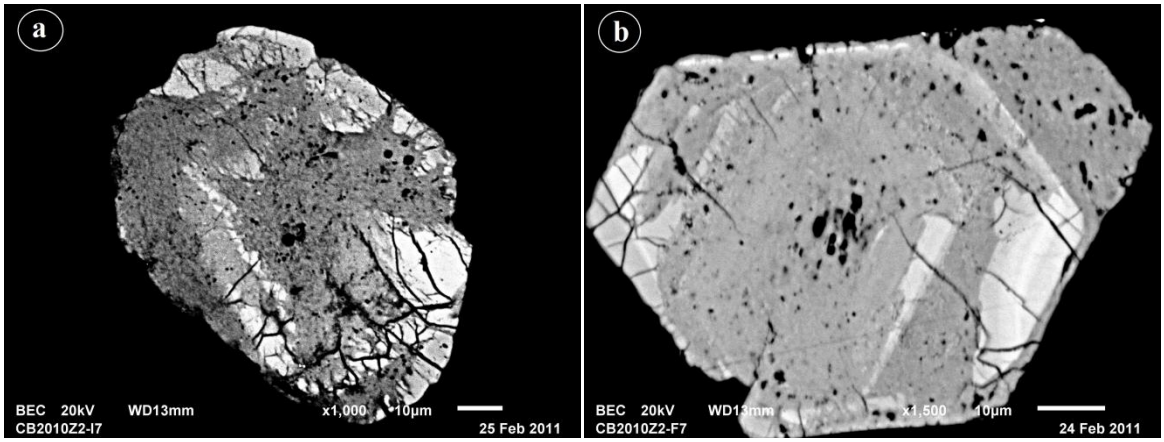

Figure 38: A and B) BSE images of extremely altered zircon grains with secondary porous texture. Remnants of primary zoning can be seen, though most has been destroyed.

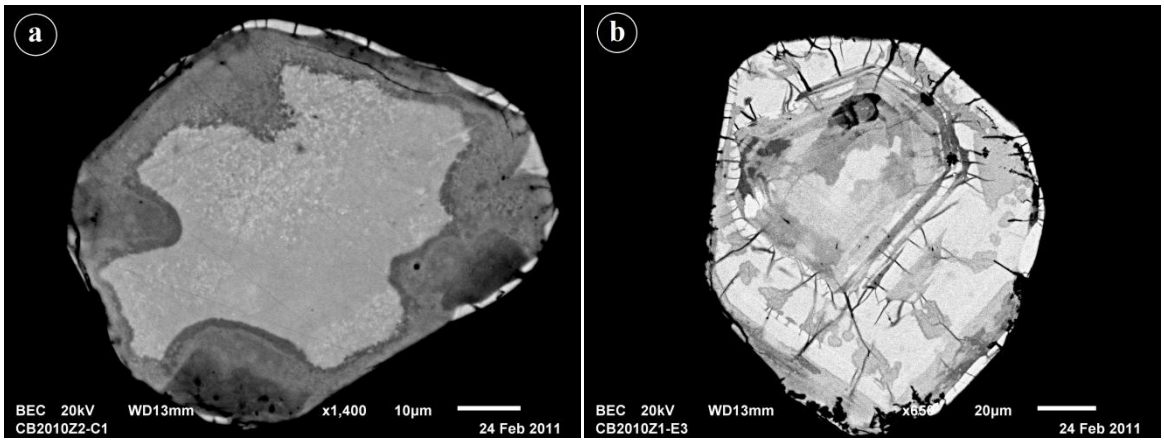

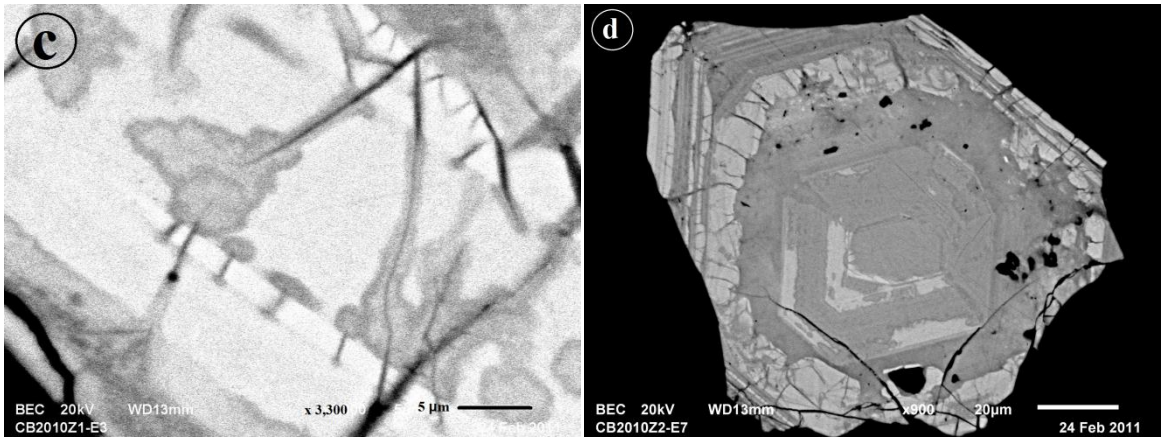

Figure 39: BSE images of alteration patterns in zircon. A) Lobate alteration front (darker colour) advancing into a crystal. B) Fractured zircon crystal exhibiting alteration originating from fractures and spreading out into the crystal. C) Magnified image of alteration following fractures. D) Alteration following the zoning of the zircon.

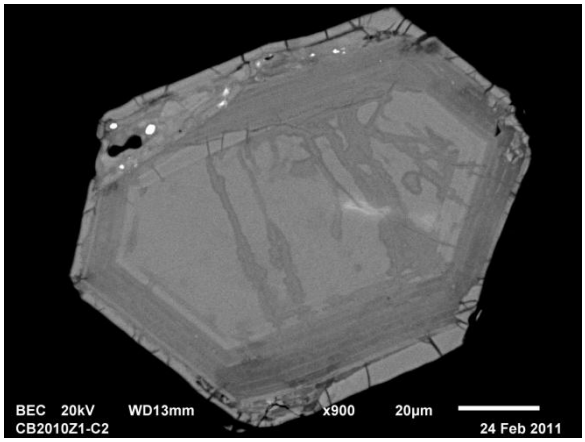

Figure 40: BSE image of a zircon grain showing alteration front entering via fractures and cutting across zonation.

Trace Element Abundances

Abundances of all measured elements, in ppm (minimum detection limits filtered), is given in Table 6. Ti was not included because of a high potential for interference from silicon oxide and phosphate. This interference was observed as disagreement of abundances between isotopes. Where more than one isotope of an element was measured, the value for the more abundant isotope was used for normalization and plotting. Also for plotting and normalization purposes, values below detection limits were considered 0. Figure 41 is a plot of silicate earth normalized (McDonough and Sun, 1995) abundances for all trace elements measured. The accompanying data is given in Table 7.

Table 6: Results of trace element analysis in 16 spots on 15 zircon from sample CB2010Z2. Abundances are in ppm, minimum detection limits filtered.

Element	Z2-F1	Z2-J1	Z2-H2	Z2-F2	Z2-F2(2)	Z2-I3	Z2-F4	Z2-G5	Z2-I6	Z2-H6	Z2-D6	Z2-D7	Z2-G7	Z2-J7	Z2-I8	Z2-G8
Li7	261.33	300.81	1756.17	1778.03	721.99	282.3	366.58	329.31	271.81	335.69	230.03	333.74	418.57	345.52	596.72	154.97
P31	387	<288.46	492.22	639.63	511.8	<286.73	495.15	386.15	<262.46	1573.82	470.45	678.7	352.07	376.42	<257.67	<247.19
Ca43	<4852.12	<4055.43	<4783.15	<4246.14	<4522.79	<4540.03	<4337.36	<4329.08	<4240.83	27426.9	<5115.81	<6517.89	<5252.99	<3904.05	<4668.56	<4206.11
Ca44	<1884.88	<1693.67	<1820.68	<1695.50	<1784.73	<1717.83	<1747.89	<1642.09	<1608.03	29192.3	<1866.50	3671.89	<2163.71	<1555.82	<1719.82	<1634.54
Ti46	1189.03	1249.14	1252.08	1163.35	1395.68	1335.95	1149.41	1215.74	1310.87	1432.64	1133.35	1486.55	1330.02	1364.5	1219.75	1221.72
Ti47	1779.79	1655.48	1566.19	1583.77	1612.1	1652.82	1446.02	1626.28	1567.35	1751.6	1456.61	1790.04	1681.28	1561.06	1587.82	1646.29
Ti49	<28.13	<29.13	<36.34	<28.28	<31.14	31.7	<35.37	<29.17	<24.90	70.56	<41.81	48.57	<39.45	<28.91	<30.74	<29.83
Ti50	<109.31	<98.35	<104.73	<100.06	<107.92	<99.23	<101.36	<101.21	<97.40	<76.80	<110.05	<144.91	<132.08	<91.65	<105.92	<97.03
Fe56	<168.98	<151.55	716.13	881.59	<153.85	421.94	<149.14	463.78	191.91	2364.15	<154.69	1759.88	<175.39	1179.66	726.49	<129.45
Sr88	12.77	<3.53	17.14	7.51	<3.50	55.21	<3.36	20.68	<3.40	686.43	39.28	132.03	22.55	41.65	8.22	<3.35
Y89	439.16	48.31	884.03	120.88	54.47	926.59	704.03	452.85	54.55	7814.13	750.92	2950.33	852.74	932.81	364.99	15.51
Nb93	13.01	2.91	24.19	15.97	2.21	77.92	5.86	19.7	1.09	492.97	47.01	612.06	3.38	14.24	37.62	<0.90
La139	5.92	<1.82	<1.95	<1.61	<1.72	23.82	1.72	22.17	<1.77	22.8	32.43	164.2	4.14	25.89	2.38	<1.99
Ce140	22.8	1.08	<1.01	<0.84	<0.71	95.2	<1.05	70.64	<0.88	163.24	101.84	628.88	9.61	65.48	31.11	<0.78
Pr141	1.93	<0.83	<0.92	<0.87	<0.92	13.59	<1.09	7.91	<0.92	17.81	14.07	71.97	<1.40	8.98	2.4	<1.07
Nd145	14.35	<10.39	<13.54	<10.65	<12.51	60.4	<9.75	38.36	<11.68	113.51	62.02	290.55	<16.45	23.21	13.66	<8.25
Nd146	7.69	<2.26	<2.89	<3.33	3.52	54.09	<4.52	29.17	<3.28	92.26	56.11	282.73	5.75	28.83	12.48	2.64
Sm147	<6.81	<5.40	<4.36	<4.98	<6.08	101.41	<6.39	29.34	4.88	317.19	53.73	285.43	<7.48	36.82	30.92	<6.02
Sm149	<7.38	<5.85	<7.29	<6.71	<7.68	82.71	<6.68	28.13	<4.59	318.52	64.37	339.24	<8.48	30.28	30.8	<6.54
Eu151	<2.37	<2.12	<1.92	<2.69	<2.56	<2.41	<2.46	<1.97	<2.13	17.91	<2.93	3.95	<2.92	<2.63	<2.16	<2.35
Eu153	<1.82	<2.25	<2.23	<1.93	<2.09	<2.31	<1.88	<2.23	<2.11	14.98	<2.11	6.16	<2.58	<1.86	<2.19	<1.70
Gd155	<16.37	<14.38	<16.50	<13.76	<16.59	132.87	<17.34	47.74	<15.51	581.31	87.11	419.15	<21.34	34.68	22.96	<15.44
Gd157	13.86	<8.01	12	13.33	<9.43	155.3	13.75	42.94	<8.35	569.26	76.12	423.44	<11.93	48.37	39.14	<10.34
Tb159	3.98	<0.68	5.06	1.77	<0.60	34.04	7.84	10.61	<0.53	193.62	24.54	104.61	10.45	13.58	10.48	<0.67
Dy161	28.2	5.8	51.76	9.99	<3.49	113.77	62.32	50.3	<2.82	872.55	98.93	399.12	81.05	80.89	45.03	<4.25
Dy163	24.43	<2.35	46.51	9.6	3.15	121.78	67.08	49.03	3.78	871.36	88.32	409.85	73.34	82.34	41.38	<3.26
Ho165	5.61	<0.74	11.05	1.13	0.84	10.44	8.16	5.11	<0.70	97.64	10.18	38.14	11.35	12.08	3.71	<0.73
Er166	23.62	2.41	42.78	4.88	2.4	21.99	23.39	10	<2.13	241.99	19.2	80.62	30.03	32.43	12.06	<1.29
Er167	17.85	<2.81	41.52	3.08	<2.68	19.31	19.17	11.26	3.35	243.51	21.3	81.62	29.81	36.19	9.67	<2.68
Tm169	7.65	0.72	13.27	1.55	0.89	3.2	5.86	2.13	<0.73	52.2	4.13	13.39	6.99	7.96	2.03	0.57
Yb171	91.5	6.36	155.59	15.14	<6.02	32.14	51.89	26.66	12.92	454.05	36.47	148.8	78.24	88.31	21.98	<7.52
Yb172	94.38	6.85	144.67	13	6.36	29.05	45.24	27.78	10.8	474.87	40.27	142.56	83.37	99.23	16.79	3.52
Yb173	86.01	6.1	153.52	10.93	8.18	29.13	47.17	26.5	6.37	493.27	40.81	156.09	77.87	100.2	15.61	<4.78
Lu175	17.59	2.05	29.96	1.56	1.5	3.63	9.33	5.3	1.45	61.63	7.29	19.47	10.63	17.68	2.63	<0.96
Hf177	51448.8	60970.8	50125.3	68377.6	58928	51556.8	42395.8	47454.9	55991.9	45850.9	44898.1	52077.3	50774.9	61886.2	73635.4	91532.6
Hf178	51686.2	62453.7	50644	68801.6	61106.5	53464.5	44229.6	49453.2	58483.8	45982.6	46840.6	52677.9	53036.6	63439.7	77326.3	94524.6
Hf179	53471.4	62225.3	50759.8	69768.5	61911.4	52990.3	44760.6	49370.4	58586.2	47284.1	46915.5	51173.7	52868.2	63719.1	76355.2	94644.3
Ta181	33.69	11.19	154.44	284.4	42.99	101.4	29.45	15.68	22.17	841.59	54.4	639.96	33.81	68.12	47.74	10.74
Th232	16.91	3.86	313.97	2011.67	77.95	163.54	6.21	11.42	60.16	676.42	14.53	28.89	9.43	96.44	31.59	1.05
U238	1428.75	581.15	9412.42	25695	3025.72	4142.51	1217.02	1399.94	2289.39	15190.7	1221.76	2816.19	1430.75	2743.65	1784.37	249.96

Table 7: Silicate earth-normalized trace element abundances in Z2 Zircon, using values from McDonough and Sun, 1995.

Element	Z2-F1	Z2-J1	Z2-H2	Z2-F2	Z2-F2(2)	Z2-I3	Z2-F4	Z2-G5	Z2-I6	Z2-H6	Z2-D6	Z2-D7	Z2-G7	Z2-J7	Z2-I8	Z2-G8
Li	163.33	188.01	1097.6	1111.3	451.24	176.44	229.11	205.82	169.88	209.81	143.77	208.59	261.61	215.95	372.95	96.856
P	4.3	0	5.4691	7.107	5.6867	0	5.5017	4.2906	0	17.487	5.2272	7.5411	3.9119	4.1824	0	0
Ca	0	0	0	0	0	0	0	0	0	1.1538	0	0.1451	0	0	0	0
Fe	0	0	0.0114	0.0141	0	0.0067	0	0.0074	0.0031	0.0378	0	0.0281	0	0.0188	0.0116	0
Sr	0.6417	0	0.8613	0.3774	0	2.7744	0	1.0392	0	34.494	1.9739	6.6347	1.1332	2.093	0.4131	0
Nb	0.0198	0.0044	0.0368	0.0243	0.0034	0.1184	0.0089	0.0299	0.0017	0.7492	0.0714	0.9302	0.0051	0.0216	0.0572	0
Y	102.13	11.235	205.59	28.112	12.667	215.49	163.73	105.31	12.686	1817.2	174.63	686.12	198.31	216.93	84.881	3.607
La	0.0091	0	0	0	0	0.0368	0.0027	0.0342	0	0.0352	0.05	0.2534	0.0064	0.04	0.0037	0
Ce	0.0136	0.0006	0	0	0	0.0568	0	0.0422	0	0.0975	0.0608	0.3755	0.0057	0.0391	0.0186	0
Pr	0.0076	0	0	0	0	0.0535	0	0.0311	0	0.0701	0.0554	0.2833	0	0.0354	0.0094	0
Nd	0.0062	0	0	0	0.0028	0.0433	0	0.0233	0	0.0738	0.0449	0.2262	0.0046	0.0231	0.01	0.0021
Sm	0	0	0	0	0	0.2498	0	0.0723	0.012	0.7813	0.1323	0.703	0	0.0907	0.0762	0
Eu	0	0	0	0	0	0	0	0	0	0.0222	0	0.0091	0	0	0	0
Gd	0.0255	0	0.0221	0.0245	0	0.2855	0.0253	0.0789	0	1.0464	0.1399	0.7784	0	0.0889	0.0719	0
Tb	0.0402	0	0.0511	0.0179	0	0.3438	0.0792	0.1072	0	1.9558	0.2479	1.0567	0.1056	0.1372	0.1059	0
Dy	0.0362	0	0.069	0.0142	0.0047	0.1807	0.0995	0.0727	0.0056	1.2928	0.131	0.6081	0.1088	0.1222	0.0614	0
Ho	0.0377	0	0.0742	0.0076	0.0056	0.0701	0.0548	0.0343	0	0.6553	0.0683	0.256	0.0762	0.0811	0.0249	0
Er	0.0539	0.0055	0.0977	0.0111	0.0055	0.0502	0.0534	0.0228	0	0.5525	0.0438	0.1841	0.0686	0.074	0.0275	0
Tm	0.1125	0.0106	0.1951	0.0228	0.0131	0.0471	0.0862	0.0313	0	0.7676	0.0607	0.1969	0.1028	0.1171	0.0299	0.0084
Yb	0.214	0.0155	0.328	0.0295	0.0144	0.0659	0.1026	0.063	0.0245	1.0768	0.0913	0.3233	0.189	0.225	0.0381	0.008
Lu	0.2606	0.0304	0.4439	0.0231	0.0222	0.0538	0.1382	0.0785	0.0215	0.913	0.108	0.2884	0.1575	0.2619	0.039	0
Hf	182.64	220.68	178.95	243.12	215.92	188.92	156.29	174.75	206.66	162.48	165.51	186.14	187.41	224.17	273.24	334.01
Ta	0.9105	0.3024	4.1741	7.6865	1.1619	2.7405	0.7959	0.4238	0.5992	22.746	1.4703	17.296	0.9138	1.8411	1.2903	0.2903
Th	0.2127	0.0486	3.9493	25.304	0.9805	2.0571	0.0781	0.1436	0.7567	8.5084	0.1828	0.3634	0.1186	1.2131	0.3974	0.0132
U	70.382	28.628	463.67	1265.8	149.05	204.06	59.952	68.963	112.78	748.31	60.185	138.73	70.48	135.16	87.9	12.313

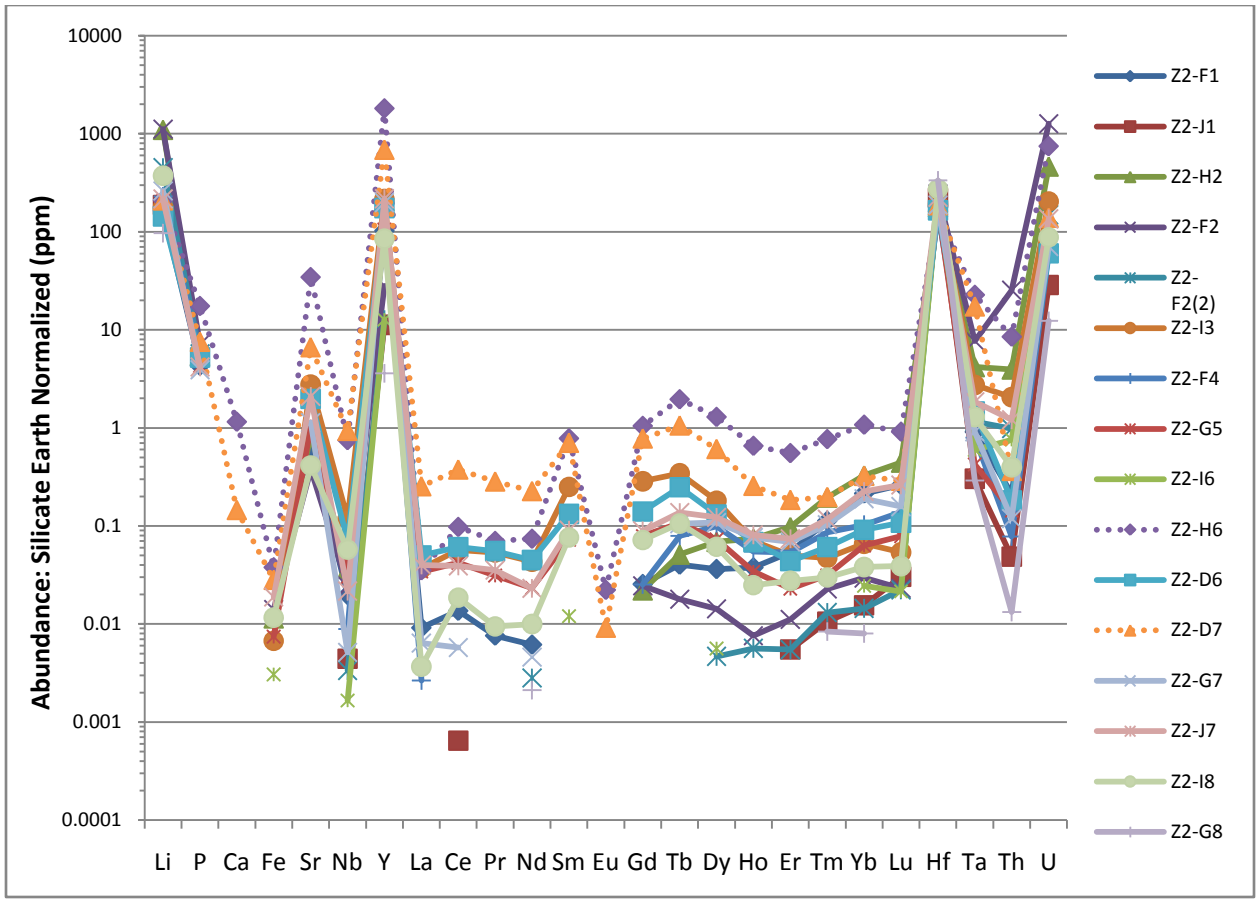

Figure 41: Silicate earth-normalized trace element abundances for Whabouchi zircon for a variety of trace elements. Patterns for samples where analysis of alteration is suspected are dashed lines (see text).

Overall, the zircon exhibit an strong enrichment in Li (10^2-10^3x silicate earth), P (10^1 - 10^2x silicate earth) and Hf (10^2x silicate earth). Y and U are also enriched but more variable, and range from a few to thousands of ppm, and tens to thousands of ppm, respectively. Likewise, enrichment of Ta varies from less than 10^0 to 10^1x silicate earth. Th abundances are variable, and the zircons range from slightly enriched to slightly depleted (10^1 to 10^{-1}x silicate earth). Similarly, Sr abundances range from less than 1 to tens of ppm. Relative to silicate earth abundances, zircon in this study is depleted in Ca (only two samples contain any), Fe and Nb.

Notably, compared to unaltered samples, altered samples are enriched in P, Ca, Fe, Sr, Nb and Y, as well as the REEs, by one to three orders of magnitude.

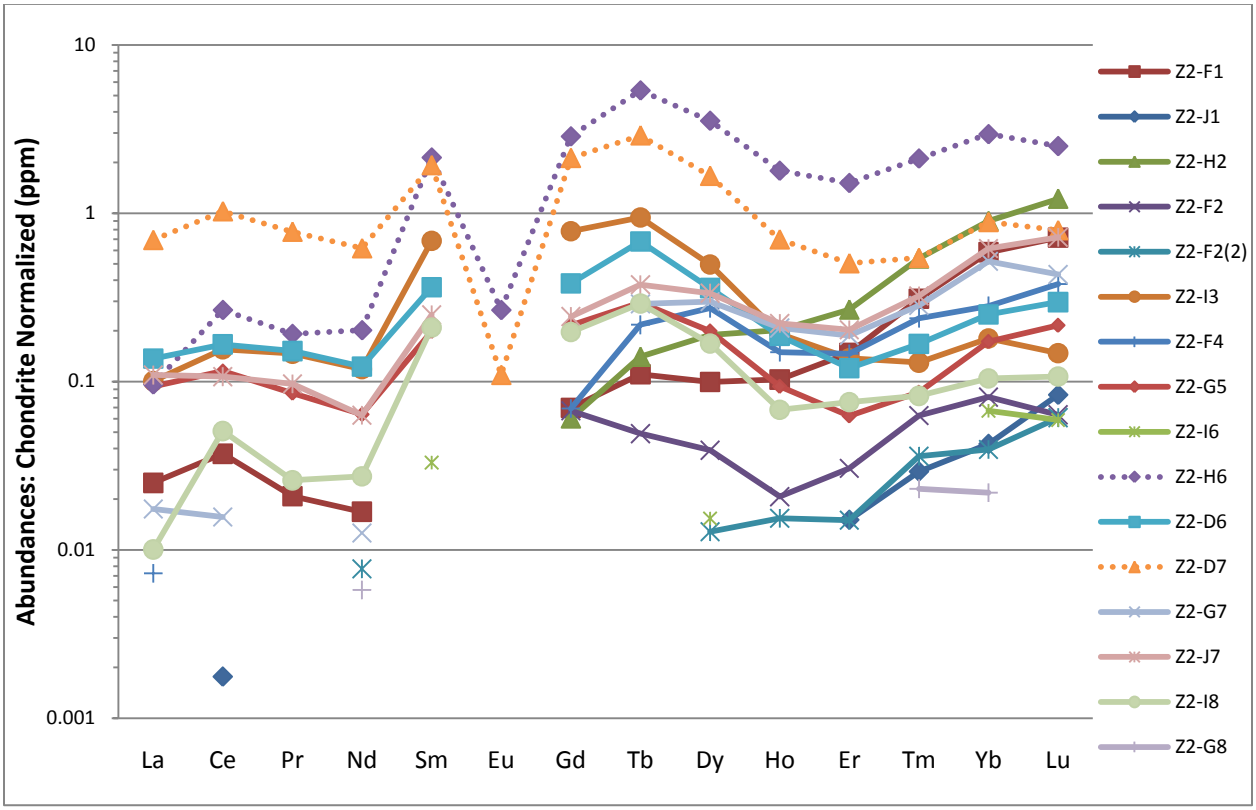

Figure 42: REE chondrite-normalized abundances in Z2 Zircon

Relative to chondritic values (McDonough and Sun, 1995), the zircon is depleted in rare earth elements (REEs) and generally exhibits fairly flat patterns (Figure 42). The accompanying data is given in Table 8. Samples Z2-I6 and Z2-G8 are mostly devoid of any REE, such that their REE patterns cannot be determined. Patterns are highly variable between samples. The zircon are especially depleted in light rare earth elements (LREEs, La-Pr); two samples contain low abundances of only one LREE and 5 samples contain none at all. Samples that do contain LREE are relatively depleted, with abundances ranging from 10^{-1} to ~ 10^{-3}x chondritic.

Table 8: Chondrite-normalized REE abundances in Z2 zircon, using values from McDonough and Sun, 1995.

Element	Z2-F1	Z2-J1	Z2-H2	Z2-F2	Z2-F2(2)	Z2-I3	Z2-F4	Z2-G5	Z2-I6	Z2-H6	Z2-D6	Z2-D7	Z2-G7	Z2-J7	Z2-I8	Z2-G8
La	0.02498	0	0	0	0	0.10051	0.00726	0.09354	0	0.0962	0.13684	0.69283	0.01747	0.10924	0.01004	0
Ce	0.03719	0.00176	0	0	0	0.1553	0	0.11524	0	0.2663	0.16613	1.02591	0.01568	0.10682	0.05075	0
Pr	0.0208	0	0	0	0	0.14644	0	0.08524	0	0.19192	0.15162	0.77554	0	0.09677	0.02586	0
Nd	0.01683	0	0	0	0.0077	0.11836	0	0.06383	0	0.20188	0.12278	0.61867	0.01258	0.06309	0.02731	0.00578
Sm	0	0	0	0	0	0.6852	0	0.19824	0.03297	2.14318	0.36304	1.92858	0	0.24878	0.20892	0
Eu	0	0	0	0	0	0	0	0	0	0.26607	0	0.10941	0	0	0	0
Gd	0.06965	0	0.0603	0.06698	0	0.7804	0.0691	0.21578	0	2.8606	0.38251	2.12784	0	0.24307	0.19668	0
Tb	0.11025	0	0.14017	0.04903	0	0.94294	0.21717	0.29391	0	5.36343	0.67978	2.89778	0.28947	0.37618	0.2903	0
Dy	0.09931	0	0.18907	0.03902	0.0128	0.49504	0.27268	0.19931	0.01537	3.54211	0.35902	1.66606	0.29813	0.33472	0.16821	0
Ho	0.10275	0	0.20238	0.0207	0.01538	0.19121	0.14945	0.09359	0	1.78828	0.18645	0.69853	0.20788	0.22125	0.06795	0
Er	0.14763	0.01506	0.26738	0.0305	0.015	0.13744	0.14619	0.0625	0	1.51244	0.12	0.50388	0.18769	0.20269	0.07538	0
Tm	0.30972	0.02915	0.53725	0.06275	0.03603	0.12955	0.23725	0.08623	0	2.11336	0.16721	0.54211	0.283	0.32227	0.08219	0.02308
Yb	0.58621	0.04255	0.89857	0.08075	0.0395	0.18043	0.28099	0.17255	0.06708	2.9495	0.25012	0.88547	0.51783	0.61634	0.10429	0.02186
Lu	0.71504	0.08333	1.21789	0.06341	0.06098	0.14756	0.37927	0.21545	0.05894	2.50528	0.29634	0.79146	0.43211	0.7187	0.10691	0

Note that patterns are roughly parallel, however heavy rare earth element (HREE, Tb-Lu) patterns are especially highly variable between samples, from a steep slope, to a humped, concave up pattern, sometimes negatively sloping. Four samples show increasing enrichment with decreasing ionic radius (though still $<10^0$x chondritic); a steep HREE pattern. Another 4 samples exhibit a concave up pattern with decreasing enrichment with decreasing ionic radius from Tb to Ho or more commonly Er, and then increasing enrichment with decreasing ionic radius. Five other samples exhibit a similar trend, except that after the inflection of the pattern at Ho or Er, enrichment does not increase sufficiently for HREE with smaller ionic radii to be more abundant than those with larger ionic radii (eg. Tb).

Ce and Eu anomalies are defined as $Ce/(La \times Pr)^{0.5}$, and $Eu/(Sm \times Gd)^{0.5}$, all in chondrite-normalized abundances (Hoskin and Schaltegger, 2003). In Whabouchi zircon, Ce anomalies are weak where they could be identified, ranging from 1.03 to 3.15. Eu was detected only in the altered samples; consequently these are the only samples displaying a negative Eu anomaly on the plots. However, samples with no detectable Eu, but detectable adjacent REEs must have a negative Eu anomaly since this element was below detection limits while those around it were not. For those samples where REEs adjacent to Eu were undetectable (Z2-J1, -F2(2),-G7 and G8), the presence of a Ce anomaly is indeterminable and unlikely.

***In Situ* U-Pb Age Dating of Single Zircon Grains**

Thirty one 10 µm spots on 25 grains were analyzed for U and Pb levels to calculate a U-Pb age. Results from all analyses are given in Figure 43 and data is provided in Table 9.

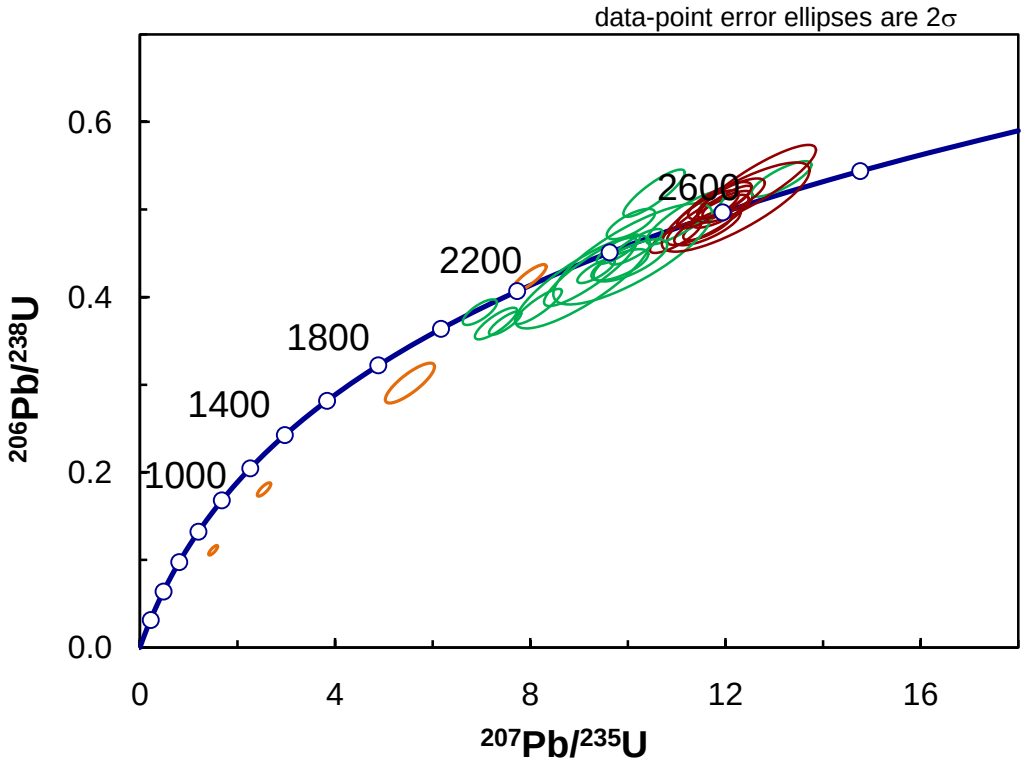

Figure 43: A plot of $^{206}Pb/^{238}U$ vs $^{207}Pb/^{235}U$ for all Whabouchi zircon, with the concordia curve in blue. Concordia ages are labelled in Ma. Green ellipses represent data points that were omitted, orange ellipses represent intentional analysis of alteration, and red ellipses represent data points used to calculate the most likely age of the Whabouchi pegmatite dyke swarm.

The concordia curve is constructed using decay constants to determine the theoretical isotopic composition (in this case, $^{206}Pb/^{238}U$, $^{207}Pb/^{235}U$) of a sample over a given amount of time assuming closed system behaviour (Dickin, 1995). Equations used to construct the concordia curve are given below:

$$\frac{206\text{Pb}}{204Pb} = \left(\frac{206\text{Pb}}{204Pb}\right)_i + \frac{238\text{U}}{204Pb}(e^{\lambda_1 238t}\text{-}1) \quad (1)$$

$$\frac{207\text{Pb}}{204Pb} = \left(\frac{207\text{Pb}}{204Pb}\right)_\text{i} + \frac{235\text{U}}{204Pb}(e^{\lambda_2 235t}\text{-}1) \quad (2)$$

where unbracketed lead ratios are the isotopic composition of lead during analysis, bracketed ratios are the initial isotopic composition of lead, U:Pb ratios are the isotopic composition during analysis, $\lambda_{1,2}$ are the decay constants of ^{238}U and ^{235}U, respectively, and t is the elapsed time since the mineral system closed (Dickin, 1995). Non-radiogenic, or common lead, ^{204}Pb is used to divide through the equations for convenience of calculating ratios rather than absolute abundances (Faure, 1977). Equations 1 and 2 can be solved for *t* to yield two independent concordant ages (Faure, 1977):

$$t_{206} = \frac{1}{\lambda_1} ln\left(\frac{\frac{206Pb}{204Pb} - \left(\frac{206Pb}{204Pb}\right)_i}{\frac{238U}{204Pb}} + 1\right) \quad (3)$$

$$t_{207} = \frac{1}{\lambda_2} ln\left(\frac{\frac{207Pb}{204Pb} - \left(\frac{207Pb}{204Pb}\right)_i}{\frac{235U}{204Pb}} + 1\right) \quad (4)$$

Data points above Concordia represent zircon that has lost U, which is indicative of leaching due to chemical weathering (Faure, 1977). U-Pb ages determined from zircons that have lost U are not accurate and would result in an age determination that is older than the true age of the rock. Four points lying relatively far above Concordia were therefore omitted on this basis.

Data points lying below Concordia represent zircon that has either lost Pb or gained U (Faure, 1977). Lead loss causes the data point to be pulled downwards below Concordia

towards the origin. Due to the extremely metamict nature of this zircon population, there is a great number of points that lie relatively far below Concordia, and 5 such points have also been omitted on this basis. Notably, the 4 analyses of alteration (in orange, Figure 43) have the most discordant ages, which emphasizes the loss of radiogenic Pb caused by alteration.

Table 9: U, ^{206}Pb abundances and calculated ages for all analyses of Whabouchi zircon. Samples highlighted in yellow were deemed too discordant and were not included in the calculation for the final reported age.

Measurements	U	Pb206	Th/U	Ages Ma			
Analysis	ppm	ppm		207Pb/206Pb	207Pb/235U	206Pb/238U	%Disc
Z2-C9.1	1984.85437	853.31415	0.00573743	2431.602295	2372.97437	2305.32397	6.17342186
Z2-D7.1	1116.676636	522.98083	0.006897088	2556.453369	2520.57617	2476.26343	3.776206017
Z2-E1.1	925.0283813	444.99487	0.014070545	2610.401123	2575.7229	2531.88428	3.635641098
Z2-F1.1	1152.325684	573.7959	0.001626449	2588.82373	2595.89331	2604.9624	-0.757875562
Z2-F2.1	3216.703125	1637.4541	0.02916874	2571.681885	2606.93652	2652.56104	-3.83793664
Z2-F4.1	1770.828735	655.5506	0.006849369	2306.691162	2170.9585	2030.31421	13.95154095
Z2-G5.1	1037.336792	403.92963	0.019410744	2369.996094	2249.76953	2120.00342	12.36448765
Z2-G7.1	925.510498	453.9794	0.004093205	2583.906494	2579.0686	2572.91602	0.515831232
Z2-G8.1	459.7608337	225.51308	0.027300969	2511.040771	2538.42944	2572.84253	-2.98587966
Z2-I6.1	2573.133545	1170.2024	0.025832102	2416.854004	2416.67212	2416.45605	0.019744858
Z2-13.1	1148.670288	551.57837	0.012002905	2612.554932	2575.2356	2528.08716	3.906784773
Z2-J1.1	371.8804016	185.98795	0.008602733	2546.076172	2576.06152	2614.34766	-3.262988091
Z2-D6.1	670.5160522	301.2562	0.006712706	2487.658936	2444.09668	2392.09546	4.596115589
Z2-F2.2	923.4460449	494.01102	0.012338066	2636.801025	2690.40649	2762.33594	-5.857603073
Z2-H2.1	8361.299805	3524.468	0.031577956	2192.648438	2228.34009	2267.38306	-4.044275284
Z2-H6.1	734.4000244	376.53156	0.004678433	2571.223633	2613.39575	2668.17285	-4.606923103
Z2-H6.2	779.3565063	404.34512	0.015695168	2314.874512	2483.21777	2694.17041	-20.08794594
Z2-I8.1	856.1887207	391.70776	0.01027667	2467.874512	2449.99731	2428.51758	1.91361618
Z2-J7.1alt	2116.039795	907.22998	0.012134766	2414.466553	2361.20947	2300.0332	5.632205486
Z2-J9.1alt	1714.949707	517.6181	0.019819805	2137.037109	1905.58716	1700.36194	23.21235847
Z1-B7-1	816.0574341	410.31061	0.006539789	2617.117676	2620.90112	2625.802	-0.403998673
Z1-C2.1	3217.094727	1342.6487	0.026830716	2431.655518	2345.83472	2248.42969	8.917964935
Z1-D3.1	850.0325928	449.92618	0.014006362	2589.488037	2653.60278	2738.52148	-7.069851398
Z1-D7-1	2187.408203	966.84747	0.017683206	2507.185547	2439.71094	2359.61426	7.02383852
Z1-D8-1	4863.827148	2351.7129	0.031424817	2356.552002	2440.52026	2542.53955	-9.559858322
Z1-D8.2	20131.75586	7704.7368	0.140315324	2124.952637	2107.14648	2088.95654	1.982939243
Z1-D9-1	4750.211914	1756.8583	0.020564245	2265.201904	2148.55933	2028.68701	12.15850449
Z1-E8-1	670.8787231	342.26038	0.017208531	2547.25708	2595.31958	2657.34375	-5.276641846
Z1-E1-1alt	8079.050781	1456.2069	0.050883025	1667.184326	1284.61548	1068.31189	38.92990112
Z1-B1-1alt	8723.717773	967.40906	0.045473289	1590.39209	931.044922	677.938477	60.36768723
Z1-E2-1	1384.745728	604.86139	0.023010865	2490.310059	2419.53857	2336.31372	7.366632462

From Figure 43, it is clear that there is a tight cluster of data near 2600 Ma. These 11 data points all agree with each other within error. To determine the most likely age, a line was fit through the origin and the cluster of data. The most likely age of the Whabouchi pegmatite dyke swarm is given by the upper intercept of this line with Concordia, and was determined to be 2577 ± 13 Ma, with a mean square of weighted deviates (MSWD) of 1.07 (Figure 44). As previously mentioned, this line is the equivalent to the weighted average of $^{207}Pb/^{206}Pb$ ages. The grains analysed contain between 372 and 3217 ppm U, with a mean Th/U of 0.011.

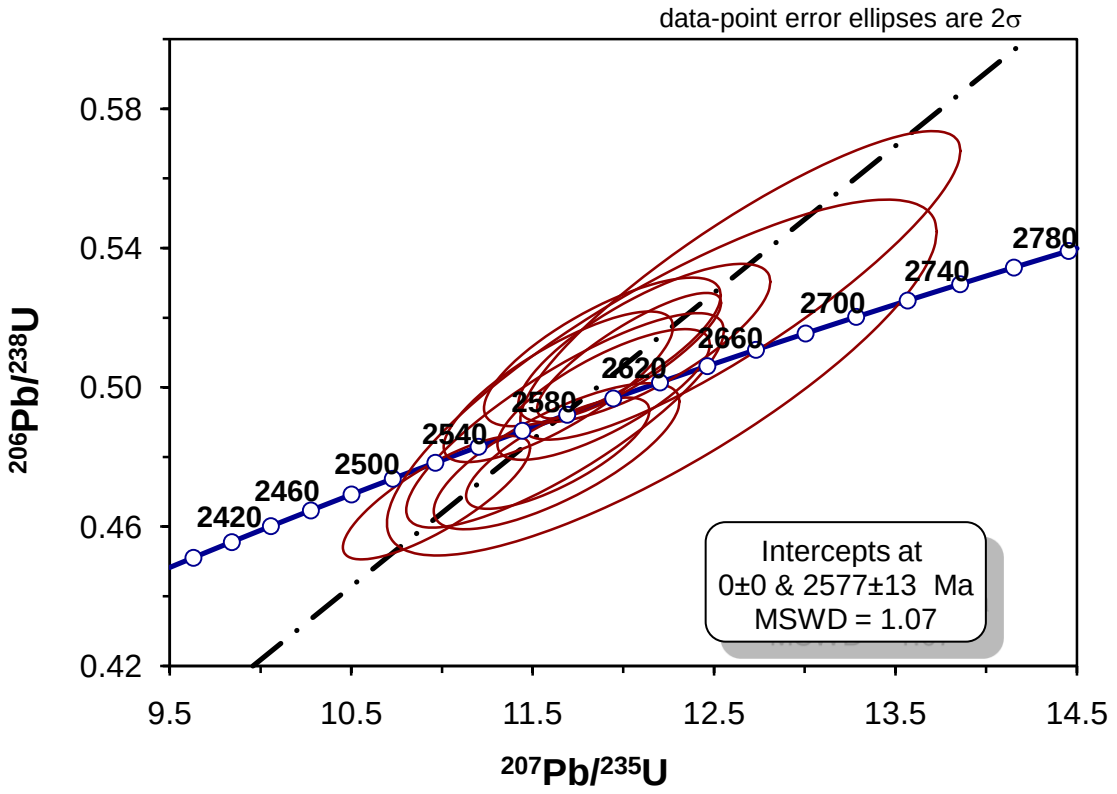

Figure 44: A plot of $^{206}Pb/^{238}U$ vs $^{207}Pb/^{235}U$ for concordant Whabouchi zircon, with the concordia curve in blue. Concordia ages are labelled in Ma. The black dashed line crosses the origin, and its intercept with concordia represents the reported age of emplacement of the Whabouchi pegmatite dykes.

DISCUSSION

PETROGRAPHY

Bulk Composition

The bulk composition of the Whabouchi Li-bearing pegmatites is peraluminous, as evidenced by the abundance of aluminosilicate minerals such as garnet, muscovite, feldspars and spodumene. As expected for peraluminous granitic compositions (Roda-Robles et al, 2010), these pegmatites contain abundant P as well. Less evolved igneous systems contain only apatite as a primary phosphate mineral, as Ca is usually in excess of P whereas the occurrence of a variety of phosphate minerals indicates an evolved system rich in P (Roda-Robles et al, 2010). Apatite and a ferromanganese phosphate variety were identified in the Whabouchi pegmatites. In a zoned field of LCT family pegmatites in Spain, Roda-Robles et al (2010) report Fe-Mn-phosphates in both the simple, intermediately-enriched pegmatites and those bearing Li-minerals.

Spodumene-Quartz Intergrowths

The most widespread and notable texture of the Whabouchi pegmatites is the spodumene-quartz intergrowth (SQI), a common textural feature of Li-rich pegmatites (Thomas et al, 1994, Cerny and Ferguson, 1972). SQI crysts are generally interpreted as the products of the isochemical breakdown of petalite (London, 1984, Stewart, 1978, Selway et al, 2005, Chakoumakos and Lumpkin, 1990), by the reaction:

$$\text{Petalite} \rightarrow \text{Spodumene} + 2\text{Quartz}$$

$$LiAlSi_4O_{10} \rightarrow LiAlSi_2O_6 + 2\ SiO_2$$

called the isochemical inversion model (Thomas et al, 1994). The inversion occurs by Li saturation within the stability field of petalite, followed by isobaric cooling which results in a transition to the spodumene stability field and consequently petalite inversion (London, 1984). Thomas et al (1994) measured modes of spodumene and quartz in SQI crysts from the Highbury pegmatite, South Africa, and found a consistent proportion of 60% to 40%, respectively. The authors report this as evidence for the petalite inversion (Thomas et al, 1994). SQI crysts are often pseudomorphic after petalite, showing fibrous or needle-like grains of spodumene oriented perpendicular to the edges of petalite crystals (Cerny and Ferguson, 1972) .The reaction is accompanied by an increase in volume, such that SQI crysts are commonly surrounded by radial fractures (Thomas et al, 1994).

An alternate interpretation for the origin of SQI involves Li saturation within the spodumene stability field and therefore spodumene crystallizing as the primary lithium aluminosilicate, followed by an abrupt decrease in pressure resulting in exsolution of a fluid phase, with petalite crystallizing directly from the hydrothermal fluid (Charoy et al, 2001). With further cooling, petalite breaks down to spodumene + quartz (Charoy et al, 2001).

The SQI in the Whabouchi pegmatite are visibile both macro- and microscopically; on neither scale are radial fractures emanating from the crysts visible. Their composition, determined by SEM modal analysis, is quartz-rich compared to theoretical expectations and those documented by Thomas et al (1994). Cerny and Ferguson (1972) noted compositional discrepancies within SQI from Tanco, but these were quartz-deficient, attributed to the migration of silica. As previously mentioned, though petalite was not recorded in the present

study, it has been noted by other workers (Laferriere, 2009) and it is likely that these SQI originated from the breakdown of petalite. This mechanism is obscured however by the deviation in composition and lack of radial fractures and petalite pseudomorphs. Excess quartz in the SQI might be explained by inversion of a quartz-rich petalite composition, since Stewart's (1978) T-X diagram for lithium aluminosilicates indicates a range of quartz-petalite solid solutions (Figure 45).

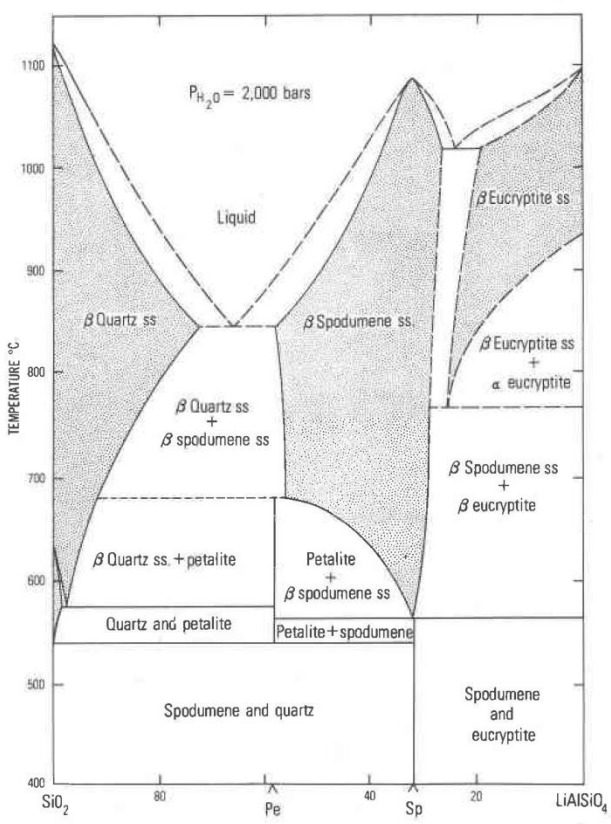

Figure 45: T-X diagram for the system quartz-eucryptite-water at 2kbar, with phase relations below 840 °C experimentally determined by Stewart, 1978 (Figure 3 from Stewart, 1978)

Whether the SQI formed from the breakdown of primary magmatic or hydrothermal petalite is unclear, and further studies to constrain the P-T path of the Whabouchi pegmatites are warranted. Also, the occurrence of symplectic textures in feldspars and muscovite, sometimes directly in contact with SQI may suggest an alternate origin for the SQI, since the breakdown of petalite cannot account for such textures. Graphic intergrowths of feldspar and quartz are very common, especially in granitic pegmatites and are formed by subsolvus crystallization of quartz and feldspar in the presence of abundant fluids (Therriault et al, 2002). Though only rarely observed, since graphic feldspar and quartz occur in direct contact with SQI crysts (Figure 23) this may suggest that the SQI in the Whabouchi pegmatite are also simply the products of an undercooled melt.

Pegmatite Classification

The Whabouchi pegmatite dyke swarm belong to the albite-spodumene type of the Rare Element-Li subclass in the LCT family of pegmatites. This is evidenced by the dominance of albite over potassic feldspar and the macroscopic textural homogeneity (lack of zonation) of the dykes. Albite-spodumene type pegmatites are known for their great enrichment in Li_2O, which approaches the experimentally determined maximum Li oxide concentration of 2.0 wt % (Cerny and Ercit, 2005). The average concentration of Li_2O in unzoned Li-rich pegmatites is 1.5 wt % (Stewart, 1978) while the average concentration in the Whabouchi pegmatites, determined thus far, is approximately 1.6 wt % (Laferriere, 2009). The Whabouchi pegmatites are therefore slightly more enriched in Li and closer to the maximum possible amount of Li_2O in pegmatites.

ZIRCON

Zircon Textures

The oscillatory zoning seen in zircon in this study is generally considered evidence for growth in a melt (Nasdala et al, 2009), indicating that the zircon is likely of igneous origin. Radial fractures are considered to originate from radiation damage, caused by radioactive decay of ^{238}U (Figure 46) within the crystal which develops a capillary network, allowing water or fluids to seep in (Faure, 1977).

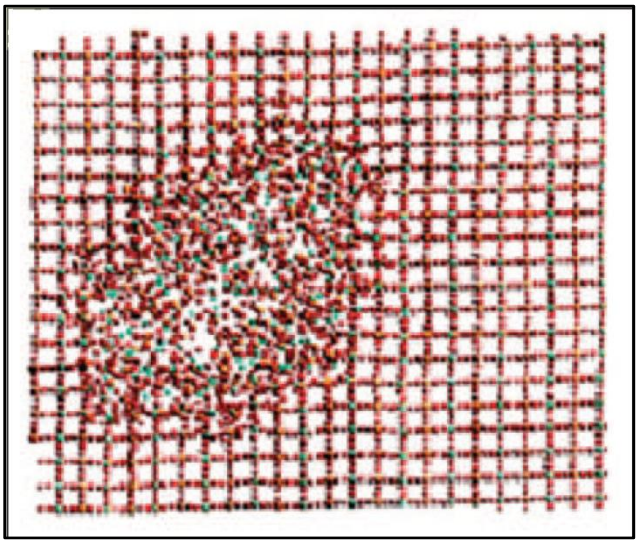

Figure 46 : A model of the damage done to the zircon lattice by emission of a single alpha particle and its recoil (Figure 2, Geisler et al, 2007)

Following radiation damage, the zircon crystal dilates and fractures (Faure, 1977). Some zones in the crystal may be more fractured than others and this is attributed to differential radiation damage due to zoning of U in the grain (Nasdala et al, 2009). The alteration fronts are sharp boundaries and commonly follow fractures, indicating alteration via fluid permeation (Rayner et al, 2005, Nasdala et al, 2009). In other cases, the alteration fronts follow internal zoning

patterns of the grain, or cut across with no discrimination between high and low U zones. Rayner et al (2005) suggest this texture represents a chemically active fluid. This is consistent with the observed changes in composition between altered and unaltered zones, where the altered zones contain Ca ± Fe ± Al ± Mn. Such compositional changes are commonly observed in metamict and fluid altered zircon (Hoskin and Schaltegger, 2003, Rayner et al, 2005, Nasdala et al, 2009, Hoshino et al, 2010). Therefore, the zircon in this study is texturally igneous in origin and has suffered severe radiation damage, promoting the development of pathways for fluid alteration, resulting in increased Ca, Fe, Al and Mn abundances. Metamictization also causes the loss of radiogenic Pb from zircon, causing U-Pb ages to be biased towards younger ages and discordancy. Accordingly, the most discordant analyses in the present study are those from intentional targeting of alteration.

Trace Element Abundances

Calcium and iron are not typically incorporated into the zircon structure in great abundances during primary crystallization, and the presence of high concentrations of these elements signifies secondary alteration, as mentioned above (Nasdala et al, 2009, Rayner et al, 2005, Hoskin and Schaltegger, 2003). The two samples in the present study with the greatest Fe concentration, Z2-H6 and Z2-D7, are also the only two that contained abundances of Ca above detection levels, and are therefore considered to be the most altered.

Strontium, Nb and Ta usually do not occur in great concentrations in igneous zircon, with Sr up to 6 ppm, Ta less than 3 ppm; Nb however is highly variable (Hoskin and Schaltegger, 2003). The Whabouchi zircon is mostly typical in this regard, with low Sr and Nb. It is however

enriched in Ta, ranging from 0.79 to 20.91 ppm. Van Lichtervelde et al (2009) investigated Ta abundances in zircon from different zones of Ta oxide mineralization in the Tanco pegmatite in Manitoba, Canada. These authors found that zircon crystallized in units devoid of Ta oxide mineralization were extremely enriched in Ta, up to 20,800 ppm, while zircon crystallized in units heavily mineralized in Ta oxide mineralization were relatively Ta poor (5520 ppm) (Van Lichtervelde et al, 2009). There is trace Ta oxide mineralization in the Whabouchi Li-pegmatites which may explain the low concentration of Ta in zircon, though it is much lower than that documented at Tanco. However, these differences in Ta abundances in zircon may simply reflect the difference in abundance of Ta mineralization between the pegmatites; Ta mineralization is highly abundant at Tanco (London, 2008), while it is present in only trace amounts at Whabouchi.

Zircon in this study is extremely enriched in Li, with absolute Li abundances ranging from 155 to 1778 ppm (mean = 558 ppm). Unaltered magmatic zircon typically contains little Li, ranging from 8 ppb (Ushikubo et al, 2008) to less than 3 ppm (Hoskin and Schaltegger, 2003), though abundances may reach 10 to 70 ppm in zircon crystallized from evolved crustal melts (Ushikubo et al, 2008). Although data are sparse, exceptionally Li enriched zircon has been reported from anatectic melts of amphibolite-granulite facies metasediments and Li-mineral bearing pegmatites, with the highest abundance ever reported being 250 ppm, from the Harding pegmatite (Ushikubo et al, 2008), mined for beryl, spodumene and microlite (London, 2008). Zircon in the present study is therefore enriched in Li at unprecedented levels.

In a study of trace element abundances of the Jack Hills zircon, Ushikubo et al (2008) found concentrations of Li ranging from approximately 5 to 70 ppm. These workers conducted Li ion mapping and did not find elevated Li abundances in alteration fronts near fractures. The Jack Hills zircon feature Li depleted detrital cores of igneous origin with Li enriched metamorphic zircon overgrowth rims (Ushikubo et al, 2008). These zircon are hosted in a granulite facies metaconglomerate with anatectic melting (Ushikubo et al, 2008). If Li were exceedingly mobile in zircon, it would have been redistributed by diffusion during high-grade metamorphism, and differences in Li abundances from core to rim would not be maintained (Ushikubo et al, 2008). Based on these evidences, the authors conclude that the Li concentration they measured in cores of the Jack Hills zircon represents the initial Li signature (Ushikubo et al, 2008). In the first study of Li diffusion in zircon, Cherniak and Watson (2010) determined that with fast cooling from mid-crustal metamorphic temperatures, zircon will retain its original Li signature.

Since the Whabouchi pegmatite dykes are unmetamorphosed and were emplaced after regional granulite facies metamorphism, it is likely that the Li abundances measured in zircon are primary Li and therefore represent the highest Li concentration in zircon reported to date. Furthermore, analyses of altered Whabouchi zircon contain Li abundances below average for the population. This can be taken as further evidence that the anomalously high Li abundances in these zircon are primary, and not due to alteration.

Phosphorus is commonly incorporated with REEs into zircon via the xenotime substitution:

$$(Y, REE^{3+}) + P^{5+} = Zr^{4+} + Si^{4+}$$

where P is required for charge balance to incorporate REEs (Hoskin and Schaltegger, 2003). If the xenotime substitution is the only mechanism acting to incorporate Y and REEs into zircon's structure, then (Y, REE) and P abundances should reach parity, yet this is seldom the case, and P is generally less abundant (Hoskin and Schaltegger, 2003). In the present study, (Y+ REE)/P ranges from 0 (P below detection limits) to 8.28, with a mean value of 2.07, indicative of another mechanism aiding in the incorporation of Y and REEs. It has been postulated that Li^{1+} can be substituted into the zircon crystal lattice via an interstitial mechanism (Hanchar et al, 2001):

$$Li^{1+}_{interstitial} + (Y, REE)^{3+} = Zr^{4+} + \square$$

The ratio of (Y+REE) / (P + Li) in Whabouchi zircons ranges from 0.02 to 5.76, with a mean value of 1.72, which is closer to parity and suggests that Li had a control in Y, REE subsititution into the crystal lattice. Phosphorus abundances in Whabouchi zircon are attributed to the xenotime and/or interstitial substitutions. However, the extremely high P abundances in samples Z2-H6 and Z2-D7 are attributed, at least in part, to accidental analysis of alteration since these samples also contain extremely elevated Ca and Fe abundances.

Typical U abundance for zircon is 4000 ppm, (0.4 wt %), while Th concentrations are generally 2000 ppm (0.2 wt %) (Speer, 1982). Uranium abundances in zircon from the present study are average, and range from 249.96 ppm to 25 695.03 ppm, with a mean value of 4044.45

ppm. Thorium is depleted and ranges from 1.05 to 2011.67 ppm, with a mean of 201.34 ppm. Consequently, Th/U ratios for this zircon population are very low, ranging from 0.004 to 0.078, with a mean of 0.022.

Zircon can become highly enriched in Hf, such that zircon and hafnon ($HfSiO_4$) form a complete solid solution series (Deer et al, 1992), though typically Hf accounts for 1.51 – 10.40 wt % of zircon from granites, and 0.85 – 18.66 wt % of those from granitic pegmatites (Hoskin and Schaltegger, 2003). Hafnium contents in zircon from the present study fall in the expected range for granitic pegmatites, with a mean value of 5.84 wt %.

REE + Y Enrichment Patterns

Typical Patterns + Granitic Pegmatite Patterns

Magmatic zircon from crustal rocks usually contain less than 1 wt % total REEs and Y, where REEs range from 250 – 5000 ppm, Y abundances range from tens of ppm to 5000 ppm, and greater enrichment is attributed to analysis of alteration or inclusions (Hoskin and Schaltegger, 2003).

REE enrichment patterns for zircon displayed on a chondrite normalized diagram characteristically exhibit a depletion in LREEs, enrichment in HREEs, and positive Ce and negative Eu anomalies. LREEs are typically present in abundances less than 10x chondrite, while HREEs are usually relatively enriched, ranging from 10^3 to 10^4 x chondrite (Hoskin and Schaltegger, 2003). These trends are expected because of easier accommodation of ions of similar size to Zr^{4+} into the zircon structure (Hoskin and Schaltegger, 2003). Zr^{4+} has an ionic

radius of 0.84Å, therefore the lattice can more easily incorporate the HREE than LREE due to their smaller ionic radii (Hoskin and Schaltegger, 2003). The ratio of Sm to La, chondrite normalized ($(Sm/La)_N$) is used to quantify the slope of the LREE portion of the curve, and for magmatic zircon it ranges from 57 to 547 (Hoskin and Schaltegger, 2003). Similarly, $(Lu/Gd)_N$ is used to describe the slope of the HREE portion of the curve, ranging from 16-74 in igneous zircon (Hoskin and Schaltegger, 2003).

Zircon from granitic pegmatites commonly exhibit a markedly steep positive slope from LREE to HREE, though the HREE may be further enriched by orders of magnitude(Figure 47; Hoshino et al, 2010) due to the high degree of fractionation of pegmatitic melts. Such zircons are commonly enriched in Hf, Y, Th, U and sometimes P (Liu et al, 2010). Liu et al (2010) documented REE and trace element abundances of zircon from compositionally simple, granitic pegmatite dykes and found LREEs to be depleted, ranging from 10^{-4} to 10^{-1} x chondrite, and HREEs to be enriched, ranging from 10^{-1} to 10^{2} x chondrite. These workers also noted strong positive Ce and negative Eu anomalies, and Th/U values of 0.06 – 0.08 (Liu et al, 2010). These data provide further evidence of the limitation of Th/U as a discriminant between host rock environments of zircon because these zircon grains are igneous in origin yet some exhibit values of the ratio considered to be metamorphic.

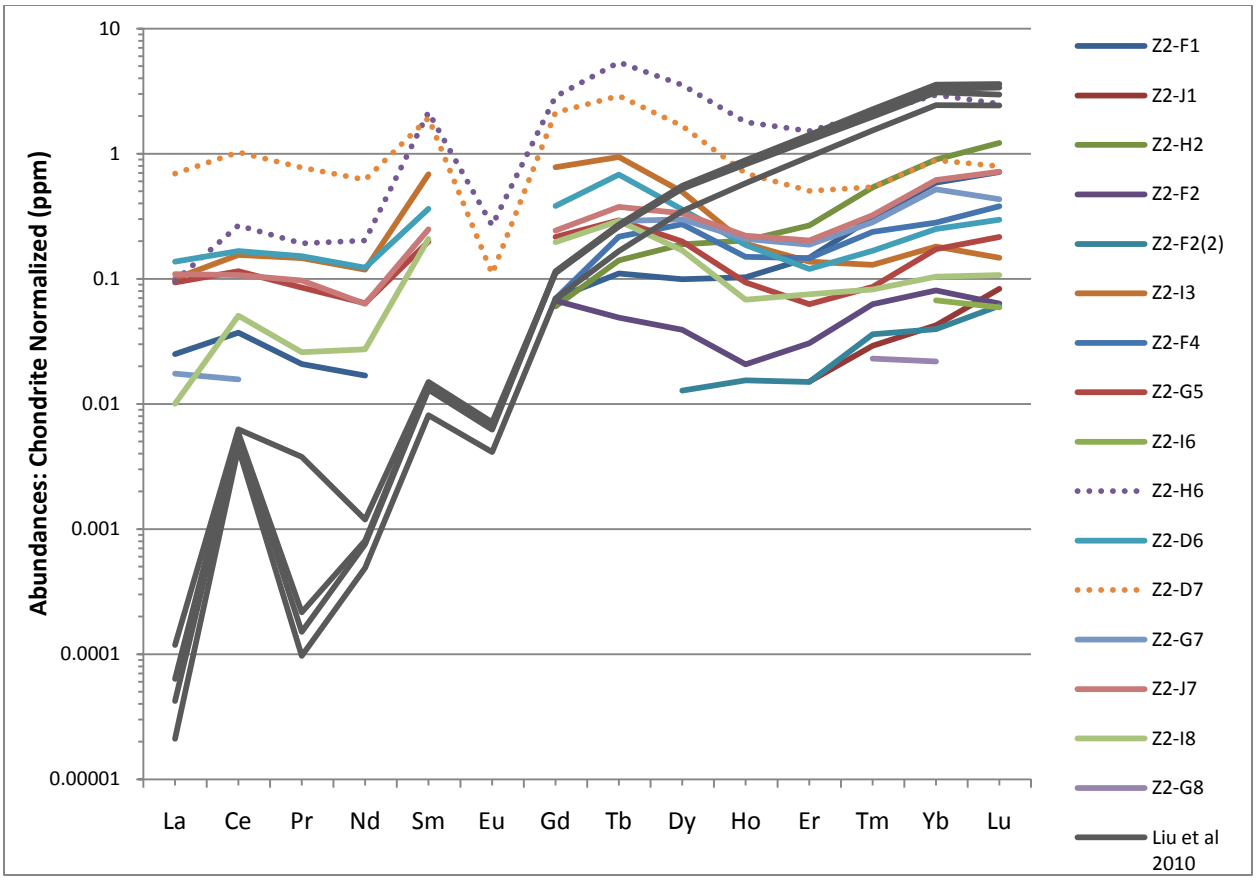

Figure 47: A plot of chondrite normalized REE abundances in zircon from a granitic pegmatite (data from Liu et al, 2010, Figure 10a) in gray, with Whabouchi zircon REE multicoloured. The dashed lines represent altered samples.

Hoshino et al (2010) investigated the geochemical trends of subduction zone related granites and granitic pegmatites and determined that they could be distinguished based on differences in their Hf and Y contents, with granites being notably depleted in both elements relative to pegmatites (Figure 48).

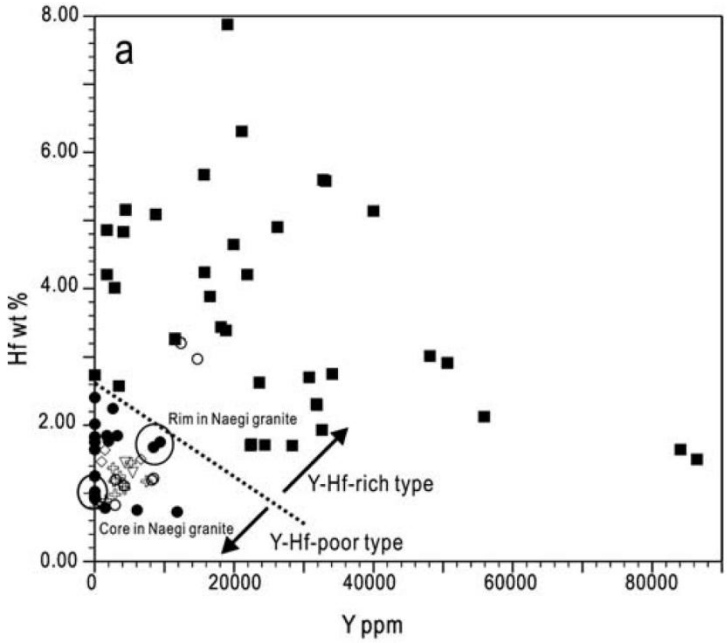

Figure 48: Plot of Hf (wt %) vs Y (ppm) for granites and related granitic pegmatites, Japan. (Hoshino et al, 2010, Figure 7a). Closed squares are pegmatites, closed circles are granite.

Similarly, high concentrations of Hf, 18.8 and 13.1 wt %, have been reported in zircon from S- and I-type granitic pegmatites, often correlated with Be-Nb-Ta mineralization (Uher, 2005). Uher (2005) also noted a subtler enrichment in Hf (mean 3.05 wt %) in highly evolved granites with Li mineralization. Pegmatites related to an I-type peraluminous granitic pluton that are extremely enriched in both Hf and Y have been reported from Spain, with mean Hf and Y abundances of 13.79 wt % and 14 050 ppm, respectively (Perez-Soba et al, 2007). Alternatively, the Hf and Y abundances of pegmatites studied in Liu et al (2010) are not consistent with the boundary in Y (ppm) – Hf (wt %) space defined by Hoshino et al (2010), as they are relatively depleted in these elements with mean values of 1297 ppm Y and 1.56 wt % Hf.

Interpretation of Whabouchi Zircon Chemistry

The Whabouchi zircons are depleted in both Y and REEs, with ΣREE+Y ranging from 0.002 – 0.159 wt %, and a mean of 0.07 wt %. Altered Whabouchi zircon are relatively enriched in ΣREE+Y, ranging from 0.5 – 1.1 wt %. Total REE abundances in unaltered zircon range by orders of magnitude, from as low as 6.73 ppm to 667.54 ppm, with an average of 233.15 ppm. Yttrium concentrations are indeed more variable and in this study range from 15.51 to 932.81 ppm, with a mean of 471.56 ppm.

The Whabouchi zircon's REE patterns are highly atypical in a number of ways. First, they are very depleted relative to chondrite in all REEs, and generally lack the characteristic steep positive slope with decreasing ionic radius. Moreover, the REE patterns are exceedingly flat, with a mean $(Sm/La)_N$ for Whabouchi zircon of 2.5, and mean $(Lu/Gd)_N$ equal to 3.0, and Ce and Eu anomalies are weak or absent. Such patterns have only been documented in zircon with mantle affinity (Hoskin and Schaltegger, 2003) whose paragenesis is not at all similar to granitic pegmatites.

A generally depleted REE pattern suggests depletion of the primary melt in REEs. REEs, Y, Th and U are increasingly depleted with increasing aluminosity of a felsic melt, such that peraluminous granitic melts are expected to be strongly depleted in these elements (Bea, 1996). In contrast, P becomes more abundant with increasing aluminum saturation as apatite solubility is heightened (Bea, 1996). Furthermore, S-type peraluminous melts are progressively depleted in REE, Y, Th and U with increasing fractionation, explained by the early crystallization of REE-Y-Th-U-sequestering phosphate minerals such as monazite and xenotime (Bea, 1996).

REE abundances in peraluminous granites are lower than the average upper crust, and rare element granites are especially depleted, with total REE abundances of a few ppm or less (Tin, 2007). Considering that the Whabouchi pegmatite dykes are highly fractionated, peraluminous, granitic residual melts, it follows that their total REE budget should be low. Xenotime nor monazite have been documented in these pegmatites however, and further petrographic studies should be conducted to better constrain this explanation for the overall depletion in REE.

Since the partition coefficients ($D^{Ci\ zircon/Ci\ melt}$) for LREE are much smaller than those for HREE, the flatness of the REE patterns for Whabouchi zircon may indicate that the primary melt was depleted in the latter group. This is expected in highly fractionated granitic rocks due to the preferential partitioning of LREE into a melt, while HREE often remain in restite (Tin, 2007). Prior or concurrent growth of garnet or xenotime with zircon has been observed to decrease abundances of HREE in zircon because these minerals sequester HREEs and therefore influence the budget of these elements that zircon will ultimately have available to it for crystallization (Whitehouse and Platt, 2003). Partition coefficients for REE between garnet and melt were determined by Rubatto (2002). The author calculated $^{TE}D_{zircon/garnet}$ and found zircon preferentially hosts Y, Nb, Hf, REE, Ce, Sm, Nd and Eu, though garnet still partitions a significant concentration of these elements (Rubatto, 2002). Garnet has been documented in the Whabouchi pegmatites, therefore it is likely that its presence further accentuated the flatness of the REE pattern in addition to an originally HREE depleted melt.

Positive Ce anomalies in zircon occur due to the preferential incorporation of Ce^{4+} over Ce^{3+} in an oxidized melt (Hoskin and Schaltegger, 2003). Absence of a Ce anomaly in zircon indicates crystallization under reducing conditions (Hoskin and Schaltegger, 2003). Zircon from mantle rocks, for example, generally have weak to no Ce anomalies (Hoskin and Schaltegger, 2003). The lack of a Ce anomaly in the Whabouchi zircon could therefore indicate that the primary melt was depleted in Ce, or reduced. S-type peraluminous granitic melts are commonly more reduced than I-type due to the abundance of organic C in their sedimentary protoliths (London, 2008). The primary melt for the Whabouchi pegmatites is likely S-type, and this could explain the weak to absent Ce anomalies in zircon. Another possibility is the early crystallization of monazite-(Ce) (a variety of monazite where Ce is the dominant LREE incorporated) which would largely decrease the availability of Ce to zircon once it began to form.

A reduced primary melt may also account for the observed negative Eu anomaly, which in part occurs due to Eu^{2+} being dominant over Eu^{3+} under reducing conditions and the excessive size of Eu^{2+}. Plagioclase also sequesters Eu^{2+} therefore its prior or concurrent growth with zircon causes a negative Eu anomaly in zircon REE patterns (Hoskin and Schaltegger, 2003). Only the altered samples exhibit a clear, negative Eu anomaly, however Eu was below detection limits for all other analyses. It is possible that if Eu were detectable at lower limits, a negative anomaly may have been documented in unaltered samples as well.

Th/U ratios have been used as a discriminant for the origin of zircon. Igneous zircon usually has $Th/U \geq 0.5$ (Hoskin and Schaltegger, 2003), while zircon with $Th/U \leq 0.07$ is

considered metamorphic (Rubatto, 2002). However, Hoskin and Ireland (2000) investigated geochemical trends for zircons from a variety of host rocks in an attempt to determine whether such information could be used as a provenance indicator. They found that in a single zircon population, Th/U varied by orders of magnitude, and that there was considerable overlap between trends for zircon formed in very different environments (Hoskin and Ireland, 2000). From their findings, Hoskin and Ireland (2000) conclude that Th/U is not a reliable discriminant of zircon origin. Zircon in this study are most likely of magmatic origin, as they exhibit characteristic igneous textures, and their host was emplaced post-granulite facies metamorphism.

Low Th/U ratios have been reported from zircons crystallized in anatectic melts, though they are accompanied by the characteristic igneous REE pattern, which the zircons in this study do not display. Lastly, the anomalously low Th/U ratio in Whabouchi zircon might be explained by concurrent growth with monazite which sequesters Th (Hoskin and Schaltegger, 2003) and Th concentrations in the primary melt are expected to be low due to its peraluminous nature as discussed above. Furthermore, magmatic zircon with low Th/U occurs in hydrous melts or hydrothermal environments (Rubin et al, 1989). While Zr solubility is enhanced with increasing water content (Harrison and Watson, 1983), U is consistently more soluble than Th for a given concentration of H_2O and the solubility of Th decreases with increasing H_2O (Kessel et al, 2005, Keppler and Wyllie, 1991). Th is therefore not transported as easily in the very hydrous pegmatite forming melt, and it follows that zircon crystallized from a hydrous, peraluminous melt exhibit low Th/U ratios.

Bulk Melt Composition Calculation

Trace element abundances in zircon may be used to calculate their abundance in the equilibrium bulk melt by the following equation:

$$C_i^{melt} = \frac{C_i^{zircon}}{D_i^{\overline{zircon}}}$$

where C^{melt} and C^{zircon} are the abundance of trace element *i* in the melt and zircon in wt %, respectively, and D is the partition coefficient for trace element *i* between zircon and melt (Hanchar and van Westrenen, 2007) assuming zircon crystallization from the early melt and equilibrium trace element partitioning (Hoskin and Schaltegger, 2003).

Using partition coefficients from Sano et al (2002) with REE abundances in zircon obtained in the present study, the total REE budget of the Whabouchi pegmatite bulk melt has been calculated, presented in Table 9. The results are plotted against measured REE patterns for granitic leucosome generated in a granulite terrane in Japan (Liu et al, 2010), for comparison (Figure 49).

Table 9: Bulk melt REE composition calculated using zircon/melt partition coefficients.

	$D^{zircon/melt}$	C zircon (wt %)	C melt (wt %)
La	4.60E-04	3.57E-06	7.76E-03
Ce	3.60E-01	4.63E-06	1.29E-05
Pr	1.72E-02	3.76E-06	2.19E-04
Nd	7.70E-02	3.13E-06	4.07E-05
Sm	8.00E-01	1.24E-05	1.55E-05
Eu	1.22E+00	0.00E+00	0.00E+00
Gd	8.00E+00	1.49E-05	1.86E-06
Tb	2.07E+01	2.42E-05	1.17E-06
Dy	4.59E+01	1.77E-05	3.86E-07
Ho	8.00E+01	1.04E-05	1.30E-07
Er	1.36E+02	1.01E-05	7.39E-08
Tm	1.97E+02	1.65E-05	8.36E-08
Yb	2.77E+02	2.76E-05	9.95E-08
Lu	3.25E+02	3.21E-05	9.88E-08

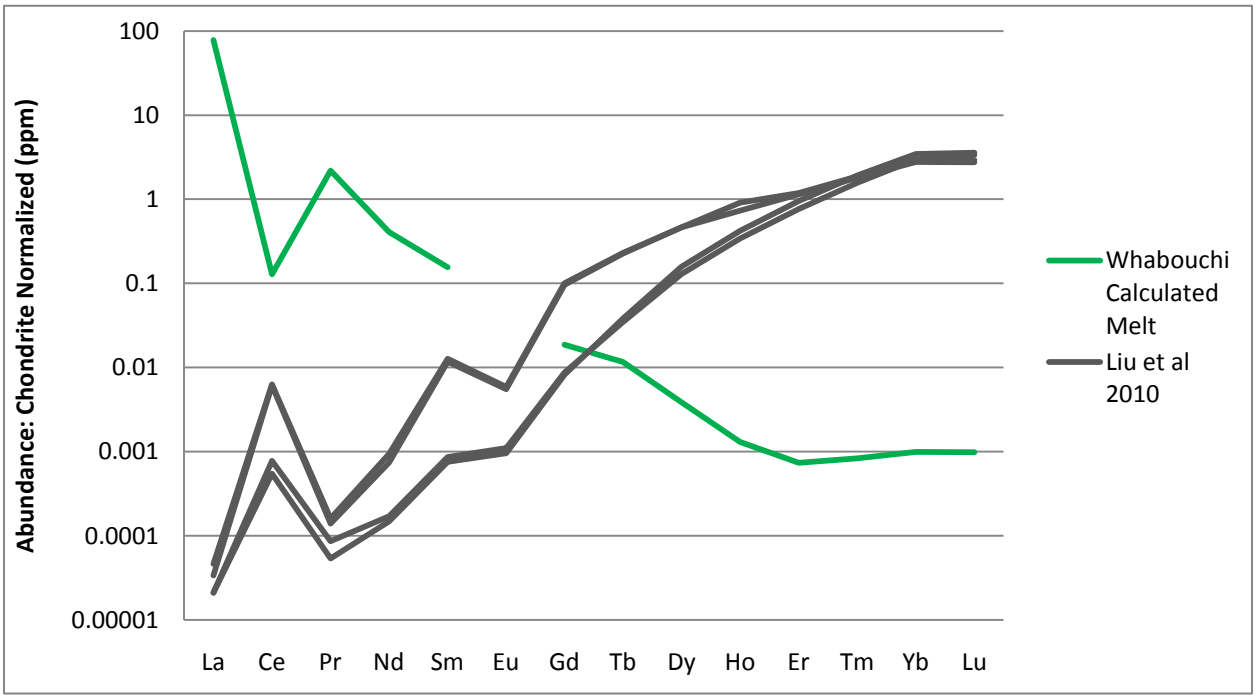

Figure 49 : A plot of chondrite normalized abundances for the calculated Whabouchi primary melt with data from Liu et al (2010).

The results of the melt composition calculation given in Table 9 and Figure 49 indicate that the primary bulk melt was overall highly depleted in REEs, and enriched in LREEs relative to HREEs, as expected for a hydrous, peraluminous, rare element pegmatite. The calculated melt composition does not well match the melt REE composition measured by Liu et al (2010), which could likely be explained by different source lithologies for the melt. It is possible that during generation of the Whabouchi pegmatite forming melt, garnet remained in the restite which would result in an HREE depleted melt. In contrast, garnet could have been melted during the generation of the granitic melts documented in Liu et al (2010) which would explain the high HREE abundances.

However, there are a number of *caveats* that must be emphasized. Partition coefficients are a function of melt composition; early crystallization of zircon operates under different partition coefficients than those for later zircon for which the melt composition is unconstrained (Hoskin and Schaltegger, 2003). Moreover, it has been determined that melt composition has a large influence on REE partitioning between melt and apatite or titanite, therefore it is very possible that it also influences zircon REE partitioning (Hoskin and Schaltegger, 2003).

Furthermore, the growth of other REE-sequestering minerals would affect the validity of this melt composition calculation (Hanchar and van Westrenen, 2007). Garnet, for example, has been identified in the pegmatites, and if it crystallized before or concurrently with zircon, the HREE budget available to zircon would have been less than that of the actual primary bulk melt. If monazite and/or xenotime were also present, as suspected due to geochemical trends

of zircon, then they would have also limited the concentrations of REEs actually available to zircon.

As previously mentioned, oscillatory zoning is essentially ubiquitous in magmatic zircon and it is impossible to say which zone best represents the bulk composition of the melt (Hanchar and van Westrenen, 2007). The possibility also exists that accidental analyses of inclusions are included in the calculation (Hanchar and van Westrenen, 2007). If an REE-rich mineral inclusion is analysed, the apparent abundances in zircon will be increased, resulting in a too-rich estimate of the bulk melt composition, and vice versa.

It cannot be confirmed whether the assumptions of early crystallization under equilibrium partitioning are met in this study. In fact, it is likely that the Whabouchi zircon did not crystallize from the early melt, based on their geochemical signatures which indicate cogenetic crystallization with REE-sequestering minerals. Additionally, it has been suggested that disequilibrium partitioning largely controls the REE concentrations in zircon (Hoskin and Schaltegger, 2003). The calculated melt composition therefore represents at best a crude estimate of the average local melt that zircon crystallized from, rather than the primary bulk melt.

U-Pb Age Dating

The age of 2577 ± 13 Ma determined for the emplacement of the Whabouchi pegmatite dyke swarm indicates that they were emplaced 65 to 61 Ma after the granitic intrusions and compositionally simple pegmatite dykes, and 58 ± 13 Ma after the regional metamorphism had stabilized at amphibolite facies (end of D2 in Figure 50). Also, the Whabouchi pegmatites were

emplaced syn to late tectonically relative to the D3 folding event, though they are unfolded and undeformed.

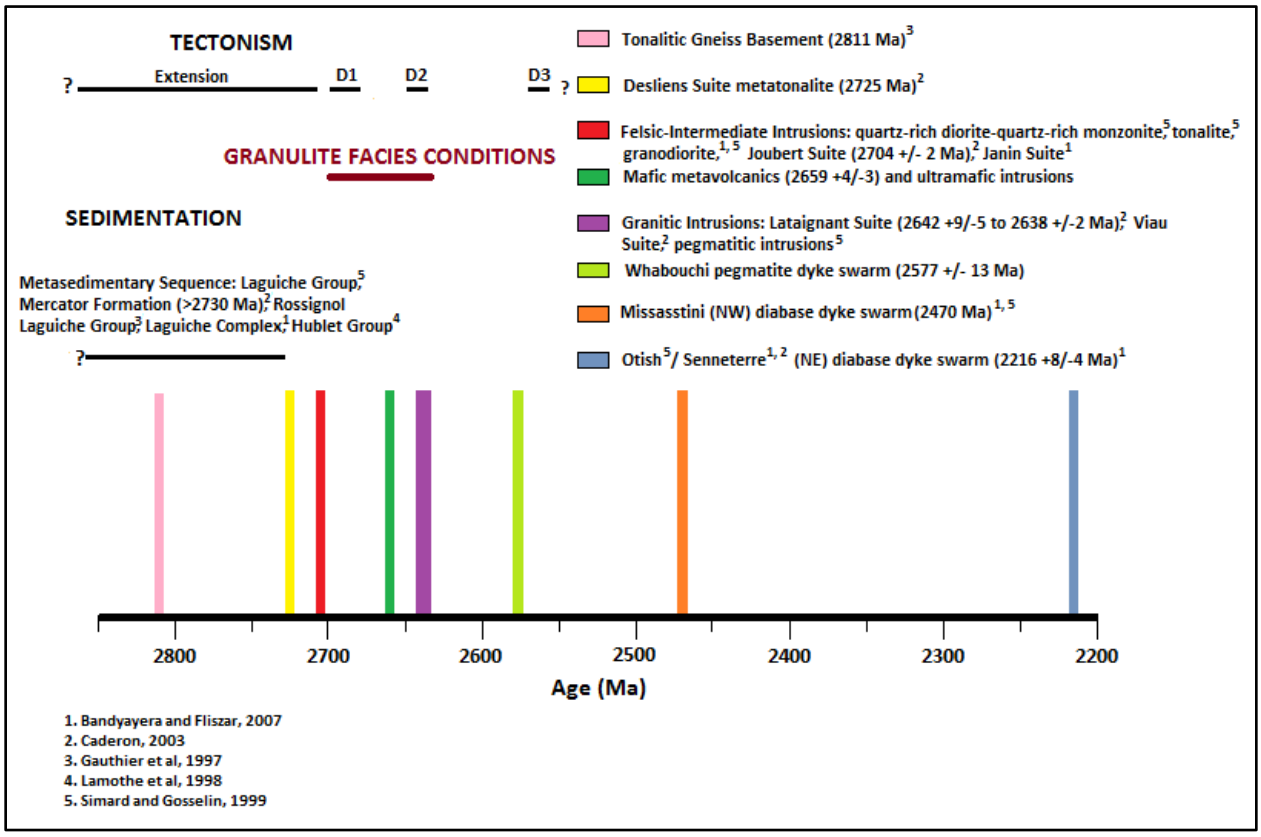

Figure 50 : Lithological timeline for the Opinaca Subprovince, with the reported age of the Whabouchi pegmatite dyke swarm. Y axis is arbitrary.

By projecting the experimentally determined solidus for Li-rich pegmatites (London, 1984) on a thermal model for homogeneous crustal thickening (England and Thompson, 1984) and extending it to greater pressures (depths), it can be estimated whether the Whabouchi melt could have been generated by anatexis from D1 and D2 related crustal thickening (Figure 51).

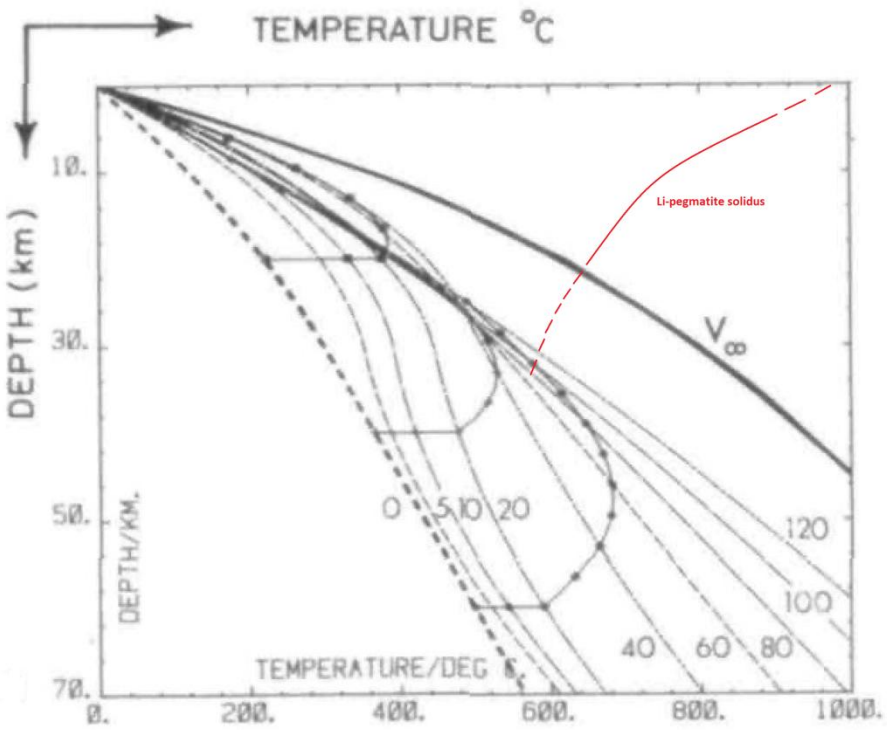

Figure 51 : Experimentally determined solidus for Li-pegmatites (London, 1984) projected onto England and Thompson's (1984) thermal model for homogeneous crustal thickening in compressional regimes.

The Whabouchi pegmatites were emplaced 58 ± 13 Ma after regional metamorphic conditions in the Opinaca subprovince stabilized at amphibolite facies. From Figure 51, it is possible that the Whabouchi pegmatite-forming melt could have been generated by anatexis due to regional metamorphism, up to 100 Ma after crustal thickening (maximum depth of burial).

Diabase dykes were emplaced along NE and NW trending fault systems in the Opinaca subprovince, whose timing of formation are unclear, though they must pre-date the mafic dyke swarms. It is possible that the Whabouchi pegmatites were emplaced along one of these NE trending deep fault systems, as pegmatites are often intruded along planes of structural

weakness (Laferriere, 2009), though constraint of the timing of deformation that caused these fault systems is required to confirm this possibility.

CONCLUSION

The Whabouchi Li-pegmatite dykes are peraluminous in composition and are classified as LCT family, albite-spodumene type pegmatites of the Rare Element Class. The origin of SQI crysts is unclear due to the lack of textures indicating the isochemical breakdown of petalite, and the presence of similar symplectic intergrowths with quartz in feldspar and muscovite, at times directly in contact with SQI. This evidence (and lack of) could suggest the same origin of subsolvus crystallization for all symplectic intergrowths present in the Whabouchi pegmatites. Zircon trace element abundances are atypical compared to other granitic pegmatites. Though the database is small, Whabouchi zircon contain the highest abundance of Li ever reported. Chondrite normalized REE diagrams for Whabouchi zircon are also atypical, and indicate a primary melt depleted in HREEs due to either prior or concurrent crystallization of garnet or retention of garnet in restite during melt generation. The age of emplacement of the Whabouchi Li-pegmatites of 2577 ± 13 Ma determined in this study indicates that they were intruded syn to late tectonically however they do not exhibit any deformation. The pegmatite forming melt may have been generated by anatexis due to crustal thickening in a compressional regime.

REFERENCES

1. Bandyayera, D. and A. Fliszar. 2007. Géologie de la région de la baie Kasipasikatch (33C09) et du lac Janin (33C16). Ministere des Ressources Naturelles et de la Faune. RP-2007-05

2. Bea, F. 1996. Residence of REE, Y, Th and U in Granites and Crustal Protoliths: Implications for the Chemistry of Crustal Melts. Journal of Petrology. 57, 521-552.

3. Bussieres, Y. and D. Theberge. 2010. NI 43-101 Technical Report – The Lac des Montagnes Property, James Bay area.

4. Caderon, S. 2003. Interpretation tectonometamorphique du nord de la Province Superieur, Quebec, Canada. PhD thesis. Universite de Quebec a Montreal.

5. Card and Ciesielski 1986. Subdivisions of the Superior Province of the Canadian Shield. Geoscience Canada. 13, 5-13.

6. Cerny, P., Ercit, T.S. 2005. The classification of granitic pegmatites revisited. The Canadian Mineralogist. 43:2005-2026.

7. Cerny, P. , Ferguson, R.B. 1972. The Tanco pegmatite at Bernic Lake, Manitoba. IV. Petalite and spodumene relations. The Canadian Mineralogist. 11, 660-678.

8. Chakoumakos, B.C., Lumpkin, G.R. 1990. Pressure-Temperature constraints on the crystallization of the Harding pegmatite. Taos County, New Mexico. The Canadian Mineralogist. 28, 287-298.

9. Charoy, B., Noronha, F., Lima, A. 2001. Spodumene-petalite-eucryptite: mutual relationships and pattern of alteration in Li-rich aplite-pegmatite dykes from Northern Portugal. The Canadian Mineralogist. 39: 729-746

10. Cherniak, D. J., Watson, E.B. 2010. Li diffusion in zircon. Contributions to Mineralogy and Petrology. 160, 383-390.

11. Davis, D. W., Pezzutto, F., Ojakangas, R. W. 1990. The age and provenance of metasedimentary rocks in the Quetico Subprovince, Ontario, from single zircon analyses: implications for Archean sedimentation and tectonics in the Superior Province. Earth and Planetary Science Letters. 99,195-205.

12. Deer, W.A., Howie, R.A., Zussman, J. *An Introduction to the Rock-Forming Minerals.* United Kingdom: Pearson Prentice Hall, 1992. Print.

13. Dickin, Alan P. *Radiogenic Isotope Geology*. United Kingdom: Cambridge University Press, 1995. Print.

14. Doyon, J. 2004. Comparaison de la composition des roches metasedimentaires archeennes dans six basins de la Province du Superieur: une etude geochimique et statistique. Master's thesis. Universite de Quebec a Chicoutimi.

15. England, P.C., Thompson, A.B. 1984. Pressure-Temperature-time paths of regional metamorphism 1: Heat transfer during the evolution of regions of thickened continental crust. Journal of Petrology. 25: 894-928.

16. Faure, Gunter. *Principles of Isotope Geology*. Canada: John Wiley and Sons, 1977. Print.

17. Franconi, A. 1983. Region de la Gorge Prosper. Ministere de l'Energie et des Ressources, Quebec; MM 82-02

18. Gauthier, M., Chartrand, F., and Larocque, M. 1997. Cadre geologique, style et repartition des mineralisations metalliques de la Grande Riviere, Territoire de la Baie James. Ministere des Ressources Naturelles du Quebec. MB 97-30, 69 p.

19. Geisler, T., Schaltegger, U., Tomaschek, F. 2007. Re-equilibration of Zircon in Aqueous Fluids and Melts. Elements. 3: 43-50

20. Hanchar, J.M., Nagy, K.L., Fenter, P., Finch, R.J., Beno, D.J., and Sturchio, N.C. 2000. Quantification of minor phases in growth kinetics experiments with power X-ray diffraction. American Mineralogist. 85: 1217-1222.

21. Hanchar, J.M. and van Westrenen, W. 2007. Rare earth element behaviour in zircon-melt systems. Elements. 3: 37-42

22. Hanchar, J.M., Finch, R.J., Hoskin, P.W.O., Watson, E.B., Cherniak, D., Mariano, A.N. 2001. Rare earth elements in synthetic zircon: Part 1. Synthesis and rare earth element and phosphorus doping. American Mineralogist. 86: 667-680.

23. Harrison, T.M., Watson, E.B. 1983. Kinetics of zircon dissolution and Zirconium diffusion in granitic melts of variable water content. Contributions to Mineralogy and Petrology. 84: 66-72

24. Hoshino, M., Kimata, M., Nishida, N., Shimizu, M., Akasaka, T. 2010. Crystal chemistry of zircon from granitic rocks, Japan: genetic implications of HREE, U and Th enrichment. Neues Jarbuch fur Mineralogie. 187, 167-188.

25. Hoskin, P. W. O., Ireland, T. R. 2000. Rare earth element chemistry of zircon and its use as a provenance indicator. Geology. 28, 627-630.

26. Hoskin, P.W.O. and Schaltegger, U. 2003. The composition of zircon and igneous and metamorphic petrogenesis – In: Hanchar, J.M. and Hoskin, P.W.O. (eds): Zircon. Mineralogical Society of America, Reviews in Mineralogy. 53: 27-62.

27. Kelly, N. M., Harley, S. L. 2005. An integrated microtextural and chemical approach to zircon geochronology: refining the Archaean history of the Napier Complex, east Antarctica. Contributions to Mineralogy and Petrology. 149, 57-84.

28. Keppler, H., Wyllie, P. J. 1991. Partitioning of Cu, Sn, Mo, W, U, and Th between melt and aqueous fluid in the systems haplogranite-H_2O-HCl and haplogranite-H_20-HF. Contributions to Mineralogy and Petrology. 109, 139-150.

29. Kessel, R., Schmidt, M.W., Ulmer, P., Pettke, T. 2005. Trace element signature of subduction zone fluids, melts and supercritical fluids at 120 – 180 km depth. Nature. 437: 724-727.

30. Laferriere, A. 2009. NI 43-101 Technical Report – Mineral Resources Estimate-Whabouchi Lithium Deposit.

31. Lamothe, D., Leclair, A.D. and Choiniere, J. 1998. Geologie de la region du Lac Vallard (SNRC 23C). Ministere des Ressources Naturelles, Quebec. RG 98-13, 31 p.

32. Liu, F., Robinson, P. T., Gerdes, A., Xue, H., Liu, P., Liou, J. G. 2010. Zircon U–Pb ages, REE concentrations and Hf isotope compositions of granitic leucosome and pegmatite from the north Sulu UHP terrane in China: Constraints on the timing and nature of partial melting. Lithos. 117, 247-268.

33. London, D. 1984. Experimental phase equilibria in the system $LiAlSiO_4$-SiO_2-H_2O: a petrogenetic grid for lithium-rich pegmatites. American Geologist. 69, 995-1004.

34. London, D, Morgan VI, G. B., Herzig R. L. 1989. Vapor-undersaturated experiments in the system macusanite-H_2O at 200 MPa and the internal differentiation of granitic pegmatites. Contributions to Mineralogy and Petrology. 102: 1-17.

35. London, D. 2008. *Pegmatites*. The Canadian Mineralogist, Special Publication 10.

36. London, D. 2005b. Granitic Pegmatites: an assessment of current concepts and directions for the future. Lithos. 80: 281-303.

37. London, D. 2009. The origins of primary textures in granitic pegmatites. The Canadian Mineralogist. 47: 697-724.

38. McClelland, W. C., Gilotti, J. A., Mazdab, F. K., Wooden, J. L. 2009. Trace-element record in zircons during exhumation from UHP conditions, North-East Greenland Caledonides. European Journal of Mineralogy. 21, 1135-1148.

39. McDonough, W. F., Sun, S.-s. 1995. The composition of the Earth. Chemical Geology. 120, 223-253.

40. Nabelek, P.I., Whittington, A. G., Sirbescu, M. C. 2010. The role of H_2O in rapid emplacement and crystallization of granite pegmatites: resolving the paradox of large crystals in highly undercooled melts. Contributions to Mineralogy and Petrology. 160:313-325.

41. Nasdala, L., Hanchar, J. M., Rhede, D., Kennedy, A. K., Váczi, T. 2010. Retention of uranium in complexly altered zircon: An example from Bancroft, Ontario. Chemical Geology. 269, 290-300.

42. Percival, J. A. 1990. Archean Tectonic Setting of Granulite Terranes of the Superior Province, Canada. A View from the Bottom. In. Granulites and Crustal Evolution, D. Vielzeuf and Ph. Vidal (Eds), pp. 171-193.

43. Percival J. A, Mortensen, J. K, Stern, R. A., Card, K. D. and Begin, N. J. 1992. Giant granulite terranes of the Northeastern Superior Province. The Ashuanipi Complex and Minto block. Canadian Journal of Earth Sciences. 29,2287-2308.

44. Percival, J. A. 2007. Geology and metallogeny of the Superior Province, Canada, *in* Goodfellow, W.D., ed., Mineral Deposits of Canada: A Synthesis of Major Deposit Types, District Metallogeny, the Evolution of Geological Provinces and Exploration Methods: Geological Association of Canada, Mineral Deposits Division, Special Publication 5, 903-928.

45. Pérez-Soba, C., Villaseca, C., Gonzalez del Tanago, J. 2007. The composition of zircon in the peraluminous Hercynian granites of the Spanish Central System batholith. The Canadian Mineralogist. 45, 509-527.

46. Rayner, N., Stern, R.A., Carr, S.D. Grain-scale variations in trace element composition of fluid-altered zircon, Acasta Gneiss Complex, northwestern Canada. Contributions to Mineralogy and Petrology. 148, 721-734.

47. Roda-Robles, E., Vieira, R., Pesquera, A., Lima, A. 2010. Chemical variations and significance of phosphates from the Fregeneda-Almendra pegmatite field, Central Iberian Zone (Spain and Portugal). Mineralogy and Petrology. 100: 23-34

48. Rubatto, D., Williams, I. S., Buick, I. S. 2001. Zircon and monazite response to prograde metamorphism in the Reynolds Range, central Australia. Contributions to Mineralogy and Petrology. 140, 458-468.

49. Rubatto, D. 2002. Zircon trace element geochemistry: partitioning with garnet and the link between U-Pb ages and metamorphism. Chemical Geology. 184, 123-138.

50. Rubin, J.N., Henry, C.D., Price, J.G. 1989. Hydrothermal zircon and zircon overgrowths, Sierra Blanca Peaks, Texas. American Mineralogist. 74: 865-869

51. Sano, Y., Terada, K., Fukuoka, T. 2002. High mass resolution ion microprobe analysis of rare earth elements in silicate glass, apatite and zircon: lack of matrix dependency. Chemical Geology. 184, 217-230.

52. Selway, J. B., Breaks, F.W. 2005. A review of rare-element (Li-Cs-Ta) pegmatite exploration techniques for the Superior Province, Canada, and large worldwide tantalum deposits. Exploration and Mining Geology, 14, 1-30.

53. Simard, M., et Gosselin, C. 1998. Géologie de la région du lac Lichteneger (33B). Ministère des Ressources Naturelles du Québec. RG 98-15,24 p.

54. Sirbescu, M.C., Hartwick, E.E., Student J.J. 2008. Rapid crystallization of the Animikie Red Ace Pegmatite, Florence county, northeastern Wisconsin: inclusion microthermometry and conductive cooling modeling. Contributions to Mineralogy and Petrology. 156: 289-305.

55. Sirbescu, M.C., Leatherman, M.A., Student, J.J. 2009. Apatite textures and compositions as records of crystallization processes in the Animikie Red Ace pegmatite dike, Wisconsin, USA. The Canadian Mineralogist. 47: 725-743.

56. Speer, J.A. 1982. Zircon – In: Ribbe, P.H. (ed): Orthosilicates. Mineralogical Society of America, Reviews in Mineralogy. 5: 67-112.

57. Stewart, D. B. 1978. Petrogenesis of lithium-rich pegmatites. American Mineralogist. 6, 970-980.

58. *Talison Lithium.* Talison Lithium. Electronic Publication. November 13 2010.<talisonlithium.com/what-is-lithium.aspx>

59. Therriault, A.M., Fowler, A.D., Grieve, R.A.F. 2002. The Sudbury Igneous Complex: A Differentiated Impact Melt Sheet. Economic Geology. 97: 1521-1540.

60. Thomas, R. J., Bühmann, D., Bullen, W.D., Scogings, A. J., De Bruin, D. 1994. Unusual spodumene pegmatites from the Late Kibaran of southern Natal, South Africa. Ore Geology Reviews. 9, 161-182.

61. Thomas, R., Davidson, P., Badanina, E. 2009. A melt and fluid inclusion assemblage in beryl from pegmatite in the Orlovka amazonite granite, East Transbaikalia, Russia; implications for pegmatite forming melt systems. Mineralogy and Petrology. 96: 129-140.

62. Thomas, R., Davidson, P., Rhede, D., Leh, M. 2009b. The miarolitic pegmatites from the Königshain: a contribution to understanding the genesis of pegmatites. Contributions to Mineralogy and Petrology. 157: 505-523.

63. Thomas, R., Webster, J.D., Rhede, D., Seifert,W., Rickers, K., Forster, H-J., Heinrich, W., Davidson, P. 2006. The transition from peraluminous to peralkaline granitic melts: Evidence from melt inclusions and accessory minerals. Lithos. 91: 137-149.

64. Thomas, R., Webster, J.D., Heinrich, W. 2000. Melt inclusions in pegmatite quartz: complete miscibility between silicate melts and hydrous fluids at low pressure. Contributions to Mineralogy and Petrology. 139: 394-401.

65. Tin, Q.D. 2007. Experimental studies on the behaviour of rare earth elements and tin in granitic systems. PhD thesis. Institute for Geosciences, University of Tuebingen.

66. Uher, P. 2005. Accessory zircon in orogenic to post-orogenic granites and pegmatites: compositional variations as indicator of magmatic evolution. An example from Western Carpathians, Slovakia. Geophysical Research Abstracts. 7.

67. Ushikubo, T., Kita, N.T., Cavosie, A. J., Wilde, S. A., Rudnick, R. L., Valley, J. W. 2008. Lithium in Jack Hills zircons: Evidence for extensive weathering of Earth's earliest crust. Earth and Planetary Science Letters. 272, 666-676.

68. Valiquette, G., 1975: Région de la rivière Nemiscau. Ministère des Richesses Naturelles du Québec RG 158.

69. Van Lichtervelde, M., Melcher, F., Wirth, R. 2009. Magmatic vs. hydrothermal origins for zircon associated with tantalum mineralization in the Tanco pegmatite, Manitoba, Canada. American Mineralogist. 94: 439-450

70. Whitehouse, M.J., Platt, J. P. 2003. Dating high-grade metamorphism-constraints from rare-earth elements in zircon and garnet. Contributions to Mineralogy and Petrology. 145, 61-74.